SELECTIVE MODULATION OF THE MICROBIOME: EFFORTS TOWARD A NEW PARADIGM IN HUMAN THERAPEUTICS

Adam Berkley Roberts

A dissertation submitted to the faculty of the University of North Carolina at Chapel Hill in partial fulfillment of the requirements for the degree of Doctor of Philosophy in the Department of Biochemistry and Biophysics.

Chapel Hill
2014

Approved by:

Matthew Redinbo

Gary Pielak

Brian Kuhlman

Kevin Slep

Dorothy Erie

ABSTRACT

Adam Berkley Roberts: Selective Modulation of the Microbiome: Efforts Toward a New Paradigm in Human Therapeutics
(Under the direction of Matthew Redinbo)

Drug-induced toxicity, side effects of certain therapeutics, is often more toxic than the original disease and limits the potential for dose intensification. The dose-limiting side effect of the mainstay anti-cancer therapeutic CPT-11, which is a prodrug for its active metabolite SN-38, is delayed onset diarrhea. Detoxified in the liver through conjugation with glucuronic acid, SN-38-glucuronide acts as a substrate for an enzyme, β-glucuronidase, expressed by the symbiotic microbiota naturally populating the mammalian gastrointestinal tract. Thus, bacterial β-glucuronidase inhibitors should alleviate the delayed onset diarrhea as a side effect of CPT-11. Initial high-throughput screen hits were established as potent inhibitors in biochemical assays against a range of β-glucuronidase enzymes from GI-associated bacterial species and as non-toxic to mammalian or bacterial cells. Importantly, they proved to be selective for the bacterial enzyme relative to the mammalian orthologue and proved effective in preclinical models of toxicity. X-ray crystallographic analysis of several inhibitors in complex with the bacterial enzymes highlighted structural features critical for inhibition. Exploiting these features, we were able to synthesize analogues from original screening hits that have since displayed improved *in vitro* and *in vivo* properties. These inhibitors are effective in models of drug-induced toxicity beyond CPT-11, including NSAID-induced enteropathy in the small intestine. This work is designed to ultimately create a clinical co-therapy for drugs that are limited by their toxic GI side effects caused by bacterial β-glucuronidase. This appears to be a new paradigm of drug therapy – inhibition of a bacterial enzyme for therapeutic gain without harming the microbial symbiotes essential for human health.

Dedication

To all the friends and family who helped me accomplish so much, especially Laura, who has been with me when it has mattered most, and Byron and Cathy, my parents, who have been through so much to get me here.

ACKNOWLEDGEMENTS

I would like to thank Bret Wallace from the Redinbo Lab who got this project moving and was profoundly helpful as a teacher. I would also like to thank Bill Janzen and the entire community at the UNC CICBDD for their help in training and throughout the process of performing the high-throughput screen. I would also like to thank all of our collaborators. The initial mouse studies, including all of the toxicity studies were performed by the lab of Dr. Sridhar Mani from Einstein College. The pharmacokinetic results of CPT-11 were performed by the lab of Dr. William Zamboni from UNC-Chapel Hill. NSAID toxicity and pharmacokinetic studies were performed in the lab of Dr. Urs Boelsterli from UConn. Inhibitor pharmacokinetic and bioavailability work was done by SAI Pharma. Crystallographic experiments were mainly conducted and collected at the GM/CA-CAT beamline at the APS in Chicago, IL. Fewer experiments were also assisted at the SER-CAT beamline.

I would like to thank Sara Robinson, an undergraduate from UNC-Chapel Hill, who performed various *in vitro* inhibition assays and assisted in setting up countless crystal trays. I also couldn't have done this without the help from Dr. Jon Edwards from the Redinbo Lab who provided not only technical support but also moral support during my time here. I would also like to thank the HHMI and the Translational Medicine Program at UNC for providing training and financial support. And finally, I would most like to thank Dr. Matthew Redinbo for providing invaluable training and support not only in learning techniques but also in how to truly become a scientist.

TABLE OF CONTENTS

LIST OF TABLES

LIST OF FIGURES

LIST OF ABBREVIATIONS AND SYMBOLS

Å – angstrom

α – alpha

ABT – 1-aminobenzotriazole

Ala, A – alanine

Amp – ampicillin

ASD – autism spectrum disorders

Asn, N – asparagine

Asp, D – aspartic acid

β – beta

BSA – bovine serum albumin

C – Celsius

CE – carboxylesterase

Cl – chloride

*Cp*βG – *Clostridium perfringens* β-glucuronidase

C-terminus, C-term, C-terminal – carboxy terminus

Δ – deletion

CPT-11 – irinotecan, 7-ethyl-10-[4-(1-piperidino)-1-piperidino]

DNA – deoxyribonucleic acid

DTT – D,L-dithiothreitol

EC_{50} – half maximal effective concentration

*Ec*βG – *E. coli* β-glucuronidase

F – bioavailability

F – fluorine

FL – full length

GDL – glucaro-δ-lactam

GI – gastrointestinal

Glu, E – glutamic acid

H – hydrogen

h – hour

hCE1 – human carboxylesterase 1

HEPES - 4-(2-hydroxyethyl)-1-piperazineethanesulfonic acid

His, H – histidine

HTS – high-throughput screen

Ile, I - isoleucine

IC_{50} - half maximal inhibitory concentration

IPTG – isopropyl β-D-1-thiogalactopyranoside

iv – intravenous administration

K – potassium

K_M – Michaelis constant

kDa – kilodalton

L – liter

Leu, L – leucine

LB – lurea broth

LIC – ligation independent cloning

Lys, K – lysine

µ – micro

µg – microgram

µL – microliter

µM - micromolar

MBP- maltose binding protein

mg – milligram

min – minute

mL – milliliter

mM – millimolar

mm – millimeter

mol – mole

Met, M - methionine

MW – molecular weight

Na – sodium

Ni – nickel

nM – nanomolar

nm – nanometer

NSAID – nonsteroidal anti-inflammatory drug

N-terminus, N-term N-terminal – amino terminus

OD – optical density

p – p-value

PDB – Protein Data Bank

PEG – polyethylene glycol

pH – negative log (base 10) of the molar concentration of hydronium ions

Phe, F – phenylalanine

PK – pharmacokinetic

PNP – p-nitrophenol

PNPG – p-nitrophenyl β-D-glucuronide

p.o. – *per os* (oral administration)

rCE – rabbit carboxylesterase

rpm – revolutions per minute

s – seconds

*Sa*βG – *Streptococcus agalactiae* β-glucuronidase

SEM – standard error of the mean

SN-38 – 7-Ethyl-10-hydroxy-camptothecin

SN-38G – 7-Ethyl-10-hydroxy-camptothecin-glucuronide

TCEP - *tris*(2-carboxyethyl)phosphine

TRIS – 2-Amino-2-hydroxymethyl-propane-1,3-diol

Tyr, Y – tyrosine

UGT – UDP-glucuronosyltransferase

UNC-CH – University of North Carolina at Chapel Hill

WT – wild type

w/v – weight by volume

% – percent

° – degree

Chapter 1

Introduction

1.1 Microbiome

Recent technological advances have allowed researchers to uncover a deeper understanding of the symbiotic microbial populations in humans. Indeed, because microbial cells in the human body outnumber all other kinds of cells 9 to 1, one could argue that humans simply act as a large fermenter to the host microbes. Increasingly, this humorous turn-of-phrase is becoming more authentic. Our understanding of the genetic makeup of this microbial population, known as the microbiome, and the role it plays in maintaining a functioning metabolism in humans has sprouted into common knowledge with the work of several key laboratories and the introduction of the Human Microbiome Project, which sampled and sequenced the genetic material of the microbial populations of a representative sample of healthy adults. Much like the Human Genome Project before it, the Human Microbiome Project has laid the foundation to understand, and subsequently to predict, manage, manipulate and potentially prevent, if necessary, the host-microbe interactions that lead to poor health outcomes and disease.

The completion of the Human Microbiome Project highlighted the complexity and diversity of the bacterial populations that reside in and on their human hosts. Not only do sample populations typically differ markedly between subjects, but also samples are typically rich and varied when taken over time from the same location in the same subject (1). The subjects in this comprehensive investigation were required to be “healthy” because researchers have begun to appreciate the role of the microbiota in maintaining a thriving metabolism and in the development of disease (2–4). Studies in germ-free mice indicate the critical role that the microbiota play in the development of the host lymphatic system, metabolic profiles, and neurochemical levels compared to wild-type controls (5–7). Gastrointestinal (GI)

complications are common in patients diagnosed with autism spectrum disorders (ASD), and a recent study using mouse models demonstrates that modulations of the GI microbiome contribute to the symptoms of ASD and that probiotic therapies can alleviate some of these symptoms (8). Alterations in the GI microbiota have also been implicated in the development of metabolic disorders (9, 10) and have been similarly implicated in disease pathogenesis, such as in irritable bowel syndrome, type 1 and type 2 diabetes, and cardiovascular disease (4, 11–13). Healthy GI microbiota also play an important role in directly preventing bacterial infection (2, 3) and indirectly regulating the host immune function (5, 6, 14). These emerging data emphasize the importance of maintaining a diverse and healthy population of GI commensal bacteria and suggest significantly limiting the use of broad-spectrum antibiotics, which can significantly alter the diversity of the GI microbiota. They also facilitate new explorations into the on-going chemical interplay between mammalian tissues and microbial symbiotes. At any given time, there are an innumerable amount of molecules in circulation that must be metabolized in order to promote a healthy physiology, and the mammalian microbiome plays a critical role.

1.2 The Role of the Microbiota in Mammalian Metabolism

Before compounds reach the intestine where they are impacted by the microbiota, they are typically metabolized in the liver. Accounting for ~75% of reactions, Phase I reactions are most notably and most often carried out by cytochrome P450 enzymes, which often oxidize compounds, leading to reduced toxicity (15). Phase II reactions involve conjugation of the lipophilic organic compound to charged or polar species, enhancing elimination. A major pathway involves the conjugation of a glucuronide from UDP-glucuronic acid to nucleophilic functional centers, such as oxygen in hydroxyl or carboxylic acid groups, catalyzed by UDP-glucuronosyltransferases (UGT). While this reaction often detoxifies xenobiotic compounds, metabolites such as morphine-6-O-glucuronide are active (16). This reaction is also critical for proper homeostasis of endobiotics, such as bilirubin and bile acids. Polymorphisms in UGT genes have been linked to hyperbilirubinemia associated with Crigler-Najjar and

Gilbert's syndromes (17), and, in addition to other enzymes in the liver, such as methyl- and sulfotransferases that play a critical role in Phase II reactions, to cancer (18).

These conjugation reactions are intimately linked to activity of the microbiota through enterohepatic circulation. The microbiota will often reverse the conjugation reaction and liberate the parent compound to be reabsorbed and trafficked back to the liver. Although this process potentially affects xenobiotic metabolism, it is most notably important to the metabolism of endobiotics (19). A sufficient concentration of endobiotics in circulation must be maintained for homeostasis. For instance, bile acids are required for the proper processing of cholesterols and fats. Alterations in the GI microbiota leading to the dysregulation of bile acids in circulation can have wide-ranging effects from GI disorders and atherosclerosis to diabetes and obesity (20). Hydrolase enzymes expressed endogenously and by the GI microbiota have been implicated in reversing Phase II conjugation reaction.

1.3 Glycoside Hydrolases

Carbohydrates play a critical role in a variety of cellular processes critical to a functioning and healthy metabolism, including detoxification of xenobiotics through conjugation. The unique repeating structure of carbohydrates, built up from simple sugars, allows for an almost endless array of combinations through the diversity of their bonds. Held together in a tight and efficient manner, it is critical to liberate the simple sugars from their complex chains for use as energy. It is, thus, not surprising that mammals express a wide range of enzymes that hydrolyze the assortment of glycosidic bonds that hold carbohydrates together. The family of enzymes mainly responsible for these hydrolytic reactions is known as the glycoside hydrolases. Genetic mutations in these enzymes have been implicated in a range of inherited diseases, and specific inhibitors are used as therapeutics (21).

Resident microbial populations must scavenge for energy sources in order to survive. Thus, symbiotic bacteria also express an array of glycoside hydrolase enzymes, which process short-chain carbohydrates relative to their orthologous mammalian counterparts, in order to liberate the simple sugars as a source of energy (22). This process is orthogonally critical to the metabolism of compounds which

are often detoxified through conjugation with simple sugars. Contrary to the liver, which primarily metabolizes compounds through oxidation and conjugation, the human microbiota processes chemicals through counter reductive and hydrolytic reactions and plays a key role in the enterohepatic circulation of metabolized compounds including xenobiotic drugs and endobiotic molecules such as bile acids.

1.4 β-Glucuronidase

One key family member of the glycoside hydrolases is β-glucuronidase. Found in plants, animals, and microorganisms, these enzymes hydrolyze carbohydrates that contain a glucuronide moiety, releasing glucuronic acid and the parent aglycone molecule. In humans, β-glucuronidase is isolated in lysosomes, acting as an acid hydrolase in glycosaminoglycan degradation (19). Researchers have also noted an increase in extracellular β-glucuronidase activity around tumors, stimulating new investigations into glucuronide prodrugs that could be liberated at the site of the tumor (23). In microbes, an orthologous form of β-glucuronidase is expressed in order to use passing glucuronidated compounds as an energy source. The general ubiquity of β-glucuronidase has allowed it to be used as a reporter gene in biological experiments and as a marker for microbial contamination (24, 25).

Original research into microbial β-glucuronidase activity led to the conclusion that the activity was isolated to *E. coli* and other closely related species (26). Later research showed that it was expressed in a range of GI-associated species such as *Bacteroides* and *Clostridium* (27, 28). Although in some species, such as *Bacteroides*, the activity is much weaker, the species are also much more abundant, so it is believed that they still make a significant contribution to overall β-glucuronidase activity in the GI tract (27, 29). Indeed, the β-glucuronidase activity from *Bacteroides* has been attributed to a second, distinct gene (28).

Compounds are often detoxified in the liver through conjugation with glucuronic acid, so human and microbial β-glucuronidases play a key role in drug metabolism and disposition through the release of the parent compound. Indeed, interindividual changes in β-glucuronidase expression may alter the efficacy of glucuronidated compounds (30). This process may lead to an increased risk of carcinogenesis

in the GI tract due to a buildup of carcinogenic compounds (31), but more often, it is associated with acute GI toxicity.

1.5 Drug-Induced Toxicity

Toxicities associated with most often chronic or, in some cases, acute drug use are a common problem affecting the entire length of the GI tract and has only recently been appreciated owing to advances in diagnostic technology (32). The effects can be wide-ranging, either in the location of the injuries to the GI tract or in the symptoms that they engender, from benign histologic changes to fatal perforations and bleeding. In addition to drugs currently on the market, there are surely more that never made it through clinical trials due to toxic side effects.

Although the mechanisms of toxicities are not completely understood, the GI microbiota has largely been implicated. These bacteria play a critical role in a functioning metabolism owing to their considerable ability, perhaps as great as the liver, to process drugs that pass through the GI tract (33). Owing to the increasingly biopharmaceutical complexity of new drugs, potential therapeutics often suffer from poor solubility. This leads to an increase in the amount of drug that passes through the lower GI tract and then interacts with the resident microbiota. Thus, the interaction between potential therapeutics and the host microbiota should be thoroughly explored in any proper drug development process.

Sorivudine is the foremost example in the dangers in unforeseen drug-induced toxicities. Use of sorivudine indirectly caused the death of at least eighteen patients soon after it was approved for use in Japan. Unbeknownst to researchers, sorivudine was metabolized by GI microbiota and its metabolite inhibited the biotransformation of the potent chemotherapeutic 5-flourouracil, leading to a severely toxic buildup (34). This tragic episode highlights the importance of understanding how new therapies are metabolized by GI microbiota and has led to the development of new models and screens in preclinical trials. In response to drugs currently on the market, researchers are searching for paths to limit toxicity, and they are beginning to target the GI microbiota.

1.6 CPT-11

Extracted from the Asian tree *Camptotheca acuminata*, camptothecin was first identified in 1966 as a drug with potential anti-tumor efficacy. Preclinical trials revealed activity in gastric and colonic tumors, so camptothecin was developed as a therapy for GI malignancies (35). Although preclinical data was promising, the development of camptothecin was hampered by poor solubility and toxic side effects (36). These toxicities along with poor efficacy in phase II trials led to the abandonment of camptothecin as a therapy. In 1985, following the recognition of the role of topoisomerase I in DNA replication, camptothecin was found to target topoisomerase I and cause reversible single-strand breaks. After the replication fork collides with the stalled enzyme, these reversible breaks become irreversible double-strand breaks, ultimately leading to apoptotic cell death (35). Although camptothecin still suffered as a potential therapeutic, investigators began to explore and exploit the main scaffold in order to improve solubility, mitigate toxic effects, and maintain anti-tumor efficacy.

This led to the development of numerous analogues of camptothecin, including CPT-11 (irinotecan, 7-ethyl-10-[4-(1-piperidino)-1-piperidino]). CPT-11 was the first water-soluble derivative of camptothecin to be developed. It maintained potent anti-tumor activity for GI malignancies and gained approval for use in the US by 1996 (35). Today, CPT-11 is utilized worldwide for the treatment of a variety of solid malignancies, but its efficacy is often limited by severe GI toxicity (37–44). CPT-11 is most frequently employed in first- and second-line treatment of metastatic colon cancers, both alone and in combination with other agents (45, 46). Treatment for colorectal cancer is based on the stage and progression of the disease. If diagnosed early, surgery alone can be effective, but upon metastasis, radiation and chemotherapy become essential. Single-agent treatment with CPT-11 after first progression significantly increases survival time compared to other options, such as fluorouracil, combination fluorouracil/leucovorin, or supportive-care (47). In addition to colorectal cancer, CPT-11 has now been employed in preclinical and clinical trials against a range of other malignancies, including brain tumors and lung, breast, gastric, pancreatic, and gynecological cancers (48–54).

CPT-11, like its predecessor camptothecin, is not without side effects. Patients receiving this chemotherapy suffer from numerous toxicities, the most common and significant of which are myelosuppression and diarrhea. Diarrhea can occur early or late (beyond 24 hours post infusion), affects up to 40% of patients, and limits the dose that the patient can receive (37, 38, 40, 42, 44, 55). While most early onset diarrhea associated with CPT-11 treatment can be treated with anti-motility agents, the delayed GI toxicity is refractory to standard treatments (56).

CPT-11 is unique from other derivatives of camptothecin in that it contains a bulky dipiperidino side-chain in addition to the characteristic five-ring scaffold of camptothecin **(Figure 1.1)**. Thus, CPT-11 is considered a prodrug that is processed by carboxylesterase (CE) enzymes that remove the dipiperidino side chain following intravenous (IV) administration to produce, SN-38, which is thought to produce the majority of the antitumor activity in the same manner as camptothecin, by targeting the human topoisomerase I catalytic cycle (57–59). The metabolic fate of SN-38 is further regulated by UGTs in the liver and other tissues. UGT isoforms, in particular UGT1A1, catalyze the conjugation of a glucuronide group onto SN-38, producing the inactive compound SN-38 glucuronide (SN-38G), which is marked for elimination through the GI tract (60). However, as SN-38G passes through the GI tract, it acts as a substrate for bacterial β-glucuronidases, which remove the glucuronide moiety, regenerating the active metabolite SN-38 in the GI lumen. SN-38 can then impact intestinal epithelial cells, mediating cell death and producing the severe, delayed diarrhea that limits the efficacy and dose-intensification of CPT-11 (61–63). Indeed, the severity of CPT-11-induced diarrhea is correlated with levels of SN-38 in the intestinal lumen, and the intestinal microbiota have been found to play a significant role in the development of this toxicity (58, 63, 64). It has now been convincingly demonstrated that the intestinal toxicity of CPT-11 limits dose intensification and optimized delivery of CPT-11 (65–67).

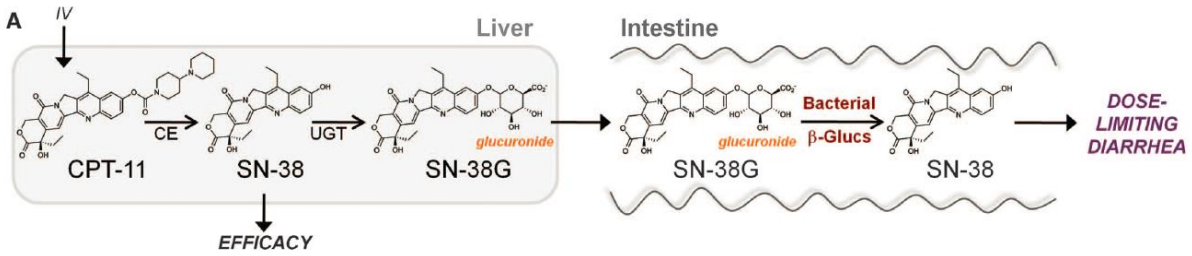

Figure 1.1. Metabolism of CPT-11. Figure is adapted from (74).

1.7 Potential Therapies

This research is not the first attempt to improve the outcome of CPT-11 treatment. Other strategies have included pharmacologic modification (68), antibiotics targeted at host microbiota (40), intestinal alkalinization (69, 70), or pharmacogenetic screening (55, 60). None of these strategies were effective, however. A specific, nontoxic solution has yet to be realized. Attempts to produce SN-38 analogues have been in production for nearly a decade and are not devoid of GI toxicity (68). Antibiotics, while successful at lessening the side effects, also harm the patient due to the role that the microbiota plays in nutrient and bile metabolism and protection against pathogenic infection. This role is even more critical in CRC patients already immune-compromised. Intestinal alkalinization, although effective at alleviating late-onset diarrhea, affects the pharmacokinetic profile of CPT-11 such that the patient receives less CPT-11 and SN-38 in systemic circulation (71). Screening of the *UGT1A1* promoter, which is responsible for polymorphisms in UGT enzymes and ultimately varying levels of glucuronidation, allows for dose reduction in patients that are more susceptible to side effects (72). Still, this method is not a prophylaxis and not effective as a treatment for the general population.

1.8 Alleviation of CPT-11-Induced Toxicity

The lab of Dr. Matthew Redinbo (UNC Chapel Hill) tackled the problem of CPT-11-induced toxicity by developing a system of targeted inhibition of bacterial β-glucuronidase. Known β-glucuronidase inhibitors were not potent enough for use as potential therapies (26, 73). In Wallace *et al.*,

utilizing a high-throughput screen of a compound library, they identified potent inhibitors of *E. coli* β-glucuronidase (*Ec*βG) (74). They showed that the inhibitors displayed sub-micromolar inhibition *in vitro*, as well as in cultured *E. coli* and anaerobic bacteria. Wallace *et al.* demonstrated that the inhibitors had no effect on mammalian β-glucuronidase and did not affect the viability of cultured bacterial or mammalian cells. This relationship was supported through crystallographic analysis of lead inhibitors bound to *Ec*βG. Crystal structures of Inhibitors 2 and 3 in complex provided evidence that these structurally similar hits bind adjacent to the enzyme's dynamic active site, which consists of residues Glu-413 and Glu-504 as well as the "bacterial loop," a region of 17 amino acids at the solvent-exposed mouth of the active site that is not present in orthologous mammalian β-glucuronidase enzymes **(Figure 1.2)**. By using a mutant form of *Ec*βG where the "bacterial loop" is deleted, they showed that Inhibitors 1 and 4 bind at the active site along with Inhibitors 2 and 3. Oral administration of one lead, when given to mice, was protective against CPT-11-induced diarrhea **(Figure 1.3)**. Healthy 6- to 8-week old Balb/cJ mice that received 10 µg Inhibitor 1 orally in conjunction with CPT-11 exhibited significantly less diarrhea compared to mice that were given only CPT-11. They also displayed fewer histologic indicators of colonic toxicity, indicating that bacterial β-glucuronidase inhibition is able to protect the endothelial cells in the mouse GI tract against CPT-11-induced toxicity (74).

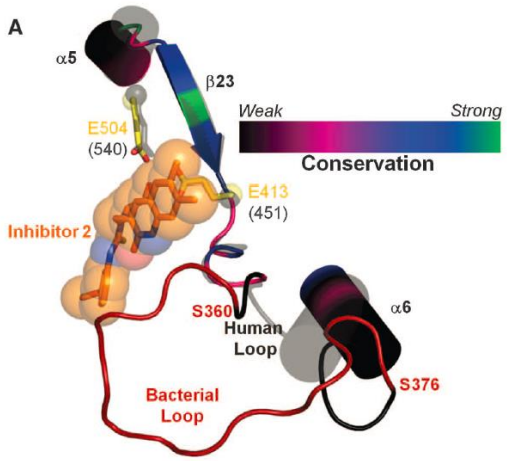

Figure 1.2. Overlay of the x-ray crystallographic structures of human β-glucuronidase and *Ec*βG bound to Inhibitor 2. Figure is adapted from (74).

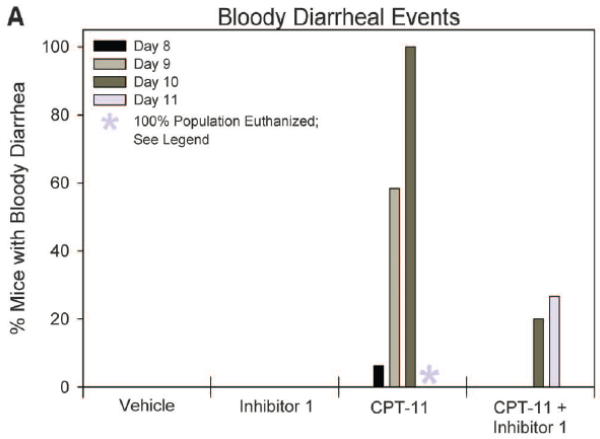

Figure 1.3. CPT-11-induced toxicity in mice is alleviated by pretreatment with Inhibitor 1. Figure is adapted from (74).Figure is adapted from (74).

1.9 NSAIDs

Many classes of drugs that contain carboxylic acid or phenolic moieties (e.g., non-steroidal anti-inflammatory drugs (NSAIDs), statins, anticonvulsants, and diuretics) are similarly inactivated and eliminated through the formation of acyl glucuronide metabolites. NSAIDs are notably associated with GI toxicity, often through unknown mechanisms (75–77). Owing to their success at relieving inflammation and pain, NSAIDs are among the most widely prescribed medications in the world with an estimated 5-10% of the US population taking NSAIDs on a regular basis (32). Side effects from NSAID use can range from ulcers, stomach erosions, and submucosal hemorrhages, to life-threatening events such as bleeding and perforation (75, 78). GI complications from chronic NSAID use in the US have been estimated to cause as high as 100,000 hospitalizations and 16,500 deaths per year (79). The average risk of developing complications is up to five-fold greater in NSAID users as opposed to non-users (75, 80).

Although the NSAID associated toxicities in the large intestine are well appreciated and understood, Graham *et al.* showed that 15 of 21 patients that were chronic NSAID users had evidence of small intestinal injuries (enteropathy), five of which had major erosions or multiple ulcers, compared to only 2 of 20 control patients (81). The mechanism underlying the enteropathy is less well understood. More recent advances in technology, namely video capsule endoscopy, have shown the extent of NSAID

related damage is wider than previously thought. Indeed two-thirds of patients have shown some form, either mild or severe, of drug-induced lesions in the small-intestine, holding true both for chronic use (> 3 months) and for short-term use (< 1 week) (82).

1.10 Alleviation of NSAID-induced toxicity

The mechanism underlying the development of NSAID-induced enteropathy has not been well-established. Specifically, many NSAIDs contain a carboxylic acid moiety that is conjugated in the liver to glucuronic acid during a typical Phase II detoxification reaction (76, 83). These glucuronidated conjugates (acyl glucuronides) are then trafficked through the bile for excretion through the waste. Initial experiments indicated that NSAID acyl glucuronide metabolites are reactive with proteins affected during enteropathy, forming irreversible protein adducts (76, 83, 84), but direct evidence for the mechanism of the underlying cause remained elusive.

With the discovery of selective bacterial β-glucuronidase inhibitors from Wallace *et al.*, the lab of Dr. Urs Boelsterli (University of Connecticut) embarked on an investigation to use this system of inhibition to flush out the relative roles played by the NSAID acyl glucuronide metabolites and their aglycone parent molecules in the development of enteropathy. Indeed, using a study of diclofenac-induced small intestinal ulcers, Loguidice *et al.* showed that selective inhibition of bacterial β-glucuronidase alleviates the drug-induced toxicity, implicating the local accumulation of the parent aglycone molecule over the acyl glucuronide metabolite in the development of enteropathy **(Figure 1.4)** (85). This finding was reinforced in Saitta *et al*. where the researchers used analogous models of indomethacin- and ketoprofen-induced toxicity that was similarly relieved via β-glucuronidase inhibitors **(Figure 1.5)** and extended their findings by demonstrating that pretreatment with β-glucuronidase inhibitors does not affect the plasma pharmacokinetic profile of any of the above NSAIDs (86).

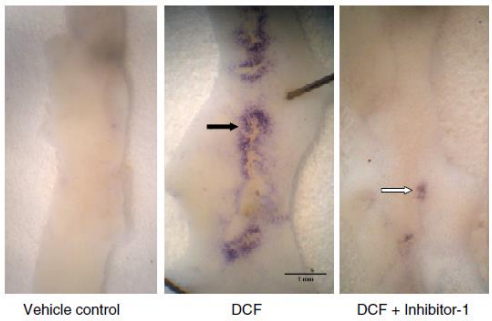

Figure 1.4. Macroscopic view of mouse jejunum in a model of diclofenac-induced ulceration. Large ulcers (DCF, black arrow) are extensive in mice treated with diclofenac. Ulcers appear blue following staining with nitroblue tetrazolium. After pretreatment with Inhibitor 1 (DCF + Inhibitor-1), only a single small ulcer is present (white arrow). Figure is adapted from (85).

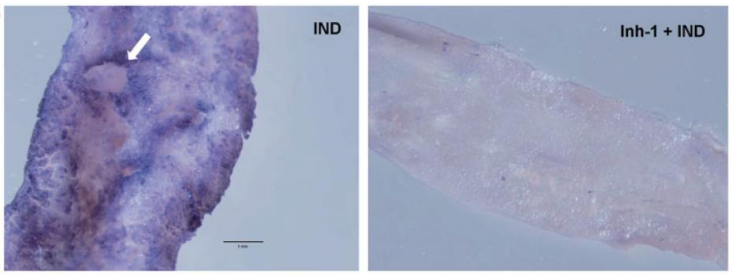

Figure 1.5. Indomethacin-induced ulcers (IND, white arrow) stained blue by nitroblue tetrazolium in the mouse jejunum. Treatment with Inhibitor 1 (Inh-1 + IND) protects mice from ulcerations. Figure is adapted from (86).

These results, along with advancing understanding of the interplay between mammalian host and symbiotic microbiota, allow for new and innovative drugs that target the microbiome in order to produce a therapeutic effect for the host (87). This system of enzyme-specific inhibition could be utilized to not only lessen acyl glucuronide-mediated toxicity, but also probe the pharmacodynamics of compounds that are similarly glucuronidated and recirculated *in vivo*. It may prove a critical step in drug development, especially those that are limited by toxic side effects.

Chapter 2

Extension of the Understanding of β-Glucuronidase from GI Bacteria and the Characterization of Novel Inhibitors[1]

2.1 Summary

Bacterial β-glucuronidase plays an important role in drug-induced toxicity in the gastrointestinal tract. Selective disruption of bacterial β-glucuronidases by small molecule inhibitors alleviates side effects of drug metabolites, which can be dose-limiting. Here, we characterize putative β-glucuronidase inhibitors that impact β-glucuronidase activity in *E. coli* cells with EC_{50} values as low as 300 nM, but encouragingly prove ineffective in assays with purified mammalian β-glucuronidase. The 2.8 Å resolution crystal structure of one inhibitor bound to *E. coli* β-glucuronidase demonstrates that it contacts and orders a portion of the "bacterial loop" present in microbial, but not mammalian, β-glucuronidases. We additionally express and purify β-glucuronidase enzymes from GI-associated species *Streptococcus agalactiae* and *Clostridium perfringens* and demonstrate that not all of the compounds are effective against each species. Crystal structures of each new species highlight structural similarities and differences to the previously determined structure of *E.* coli β-glucuronidase. The most potent compound examined in this group was found to protect mice against CPT-11-induced diarrhea. These data advance the understanding of the chemical and structural basis of selective microbial β-glucuronidase inhibition, which may improve human drug efficacy and toxicity.

[1]Adapted from: Roberts AB, et al. Molecular Insights into Microbial β-Glucuronidase Inhibition to Abrogate CPT-11 Toxicity. *Mol. Pharmacol.* 2013

2.2 Introduction

CPT-11, approved for use in a variety of malignancies and in preclinical trials for many more, is often limited by toxic gastrointestinal (GI) side effects (37–44). Similar GI complications from chronic use of non-steroidal anti-inflammatory drugs (NSAID), one of the most commonly prescribed medications worldwide, are of growing concern (77, 81, 82). Prescribed for diverse reasons, these drugs share a common metabolic pathway. CPT-11 and certain NSAIDs undergo conjugation with glucuronic acid (58, 76, 88, 89). In each case, these detoxified metabolites are reactivated in the intestinal lumen by a symbiotic bacterial enzyme, β-glucuronidase, leading to toxic damage to the intestinal epithelium (90).

The role played by microbial enzymes in therapeutic metabolism has been appreciated since the early days of drug discovery (33). We recently hypothesized that selective inhibitors would alleviate drug-induced toxicity mediated by bacterial β-glucuronidases. *In vitro* and cell-based assays demonstrated that a set of chemically similar compounds identified by high-throughput screening displayed potent, selective inhibition of *E. coli* β-glucuronidase (*Ec*βG) and did not impact the viability of cultured bacterial or mammalian cells (74). Accordingly, oral administration of one of the inhibitors in mice alleviated CPT-11-induced diarrhea and intestinal damage (74). Furthermore, in a subsequent study, the administration of the same inhibitor protected mice from small intestinal ulceration caused by the NSAIDs diclofenac, indomethacin, and ketoprofen, which are also subject to glucuronidation and reactivation in the intestinal lumen (85, 86).

Here we describe the inhibitory profile of four novel compounds that are chemically distinct from the originally reported set (74, 91), shown to be *in vitro* inhibitors of *Ec*βG and non-lethal to cultured *E. coli* and mammalian cells. However, *E. coli,* from the Proteobacteria phylum, is only one of a myriad of species of bacteria that are known to populate the human GI tract. As such, we additionally expressed and purified β-glucuronidases from *Streptococcus agalactiae* and *Clostridium perfringens*, two Firmicute bacteria from the mammalian microbiota population. These enzymes were characterized kinetically, and four novel compounds were tested for their ability to impact enzyme activity. Interestingly, although each inhibitor was effective against *Ec*βG, not all of the compounds were effective against *S. agalactiae* and *C.*

perfringens β-glucuronidase (*Sa*βG and *Cp*βG, respectively). The x-ray crystal structure of *Ec*βG in complex with one of the inhibitors reveals that it binds to the entrance of the enzyme's active site and makes contact with, but does not completely order, the flexible "bacterial loop" unique to the microbial β-glucuronidases. This structure highlights the binding mode for one compound that was ineffective against *Sa*βG and *Cp*βG. By comparing that structure to the un-liganded structures of *Sa*βG and *Cp*βG, we can begin to draw conclusions as to why that particular compound is ineffective. We also show that the most potent of these new compounds protects mice from CPT-11-induced diarrhea. Taken together, these data enhance the understanding of the selective modulation of microbial β-glucuronidases, which may lead to the targeted alleviation of drug-induced toxicity in the human GI tract.

2.3 Materials and Methods

Expression and Purification

E coli β-glucuronidase (*Ec*βG) (EC 3.2.1.31) was expressed and purified as described previously (74). *S. agalactiae* and *C. perfringens* β-glucuronidase (*Sa*βG and *Cp*βG, respectively) were purified in an analogous manner with the addition of 0.5 mM TCEP to the buffers. Purified β-glucuronidase was stored in 20 mM HEPES, 50 mM NaCl, pH 7.4 at ~10 mg/mL at ¯80 ^{o}C. The Δ360-376 form of *Ec*βG was created using PCR mutagenesis, confirmed by sequencing, and purified as described previously (74).

Inhibitor Compounds

Compounds identified from high-throughput screening (74, 91) were purchased from ASINEX, Inc, Moscow, Russia. Each compound was provided as a solid powder and dissolved initially in 100% DMSO at 25 mM.

Kinetic and Equilibrium Inhibition Assays

Inhibition assays were conducted by measuring the β-glucuronidase-catalyzed conversion of p-nitrophenyl β-D-glucuronide (PNPG) to p-nitrophenol (PNP). PNPG was acquired from Sigma-Aldrich, St. Louis, MO, and stored by dissolving in water at 250 mM. The conversion of increasing concentrations of PNPG to PNP, in the presence of 10 nM enzyme, was measured in the presence of increasing

concentrations of putative inhibitors; zero-substrate and zero-inhibitor controls were carried out at the same time. Reactions were conducted in 96-well, clear-bottom assay plates (Costar, Tewksbury, MA) at 37 ^{o}C in 50 µL of total volume. The reaction consisted of 10 µL of assay buffer (5% DMSO and 500 mM HEPES, pH 7.4), 5 µL of inhibitor (various concentrations), 5 µL of 100 nM enzyme, and 30 µL of substrate (various concentrations). Product formation was calculated by measuring the change in absorbance over time at 410 nm using a PHERAstar *Plus* microplate reader (BMG Labtech, Ortenberg, Germany). The acquired data were analyzed using Microsoft Excel and Sigmaplot 11.0. From these data, K_i values were calculated for each of the compounds.

A related assay was employed to calculate the IC_{50} values in the following manner. An analogous 50 µL reaction, consisting of enzyme (1 nM final), buffer, PNPG (1 mM final), and variable concentrations of the inhibitors, was incubated at 37 ^{o}C for 6 hours to allow the reaction to reach equilibrium and then quenched with 100 µL 0.2 M sodium carbonate. The percent inhibition for each concentration of inhibitor was calculated based on changes in absorbance and used to plot a dose-response curve. The IC_{50} value was calculated as the concentration of inhibitor that produced 50% *in vitro* inhibition. The same assay was performed with purified bovine liver β-glucuronidase with PNPG as the substrate.

We also tested the ability of these compounds to inhibit β-glucuronidase in *E. coli* cells. We grew HB101 *E. coli* cells, transformed with the pET-28a vector containing the β-glucuronidase gene, to an OD_{600} of 0.6 in LB medium and used a small aliquot in an assay similar to the *in vitro* IC_{50} assay described above. The cells (39 µL) were incubated with 1 µL of variable concentrations of inhibitor and 10 µL of 1 mM PNPG at 37 ^{o}C for 6 hours. The reaction was quenched with 100 µL 0.2 M sodium carbonate. The amount of substrate turnover and therefore the amount of inhibition is calculated from the change in absorbance compared to zero-inhibitor controls. EC_{50} values were calculated as the amount of inhibitor necessary to produce 50% inhibition. The *in vitro* and cell-based assays employed here were similar to those reported previously (74).

Additional Glycosidase Enzymes

Mammalian (bovine liver) β-glucuronidase (lyophilized powder, EC 3.2.1.31), *Prunis dulcis* β-glucosidase (lyophilized powder, EC 3.2.1.21), *Helix pomatia* β-mannosidase (ammonium sulfate suspension, EC 3.2.1.25), *E. coli* β-galactosidase (lyophilized powder, EC 3.2.1.23), and bovine liver β-galactosidase (lyophilized powder, EC 3.2.1.23) were purchased from Sigma-Aldrich, St. Louis, MO. The assays were conducted as previously published, using the appropriate p-nitrophenyl-glycosidase compound as the primary substrate for enzyme activity detection (92). Each of the four inhibitors was tested for an effect on each glycosidase enzyme activity by adding a concentration range of 0 to 100 μM to the reaction mixture. The reaction was allowed to proceed for 6 hours at 37 ^{o}C and then quenched with 100 μL 0.2 M sodium carbonate. Absorbance was measured at the appropriate wavelength, and the data were analyzed using Microsoft Excel and SigmaPlot 11.0.

Toxicity of Inhibitors Toward Cultured Cells

The toxicity of inhibitors to bacterial cells was examined by incubating HB101 *E. coli* cells, transformed with the pET-28a vector containing the β-glucuronidase gene, grown to an OD_{600} of 0.6 in LB medium with each compound, as well as DMSO and ampicillin as controls, for 6 hours. Cell survivability was measured by plating a 10^{-5} dilution of the cells on LB media enriched with kanamycin. After overnight incubation, colonies were counted to quantify cell viability. We used a similar assay to assess the inhibitor's toxicity toward cultured HCT116 human colon cancer cells, which were grown and cultured in DMEM media. Aliquots of HCT116 cells were incubated with 100 μM of each lead for 24 hours. The resulting viability of the cells was quantified by using the CellQuanti-Blue™ Cell Viability Assay Kit (BioAssay Systems, Hayward, CA). Cells are incubated with CellQuanti-Blue™ Reagent and fluorescence was measured.

Crystal Structure Determination

Crystals of *Ec*βG were obtained at 2 mg/mL protein with 30-fold molar excess Inhibitor 8 (**Figure 2.1**) in 17% PEG-3350 (w/v), 250 mM magnesium acetate, and 0.02% sodium azide (w/v) at 16 °C. Crystals first appeared after 5 days and were immediately cryo-protected with perfluoropolyether

vacuum pump oil (Sigma-Aldrich, St. Louis, MO) and flash-cooled in liquid nitrogen. Diffraction data were collected on the 22-BM beam line at SER-CAT (Advanced Photon Source, Argonne National Laboratory). Data in space group C2 were indexed and scaled using HKL2000 (93) to 2.83 Å resolution. The asymmetric unit contained two monomers. The structure was determined with Phaser (94) using molecular replacement with the recent apo *Ec*βG structure (PDB ID 3K46) as a search model. The structure was refined using simulated annealing and torsion angle refinement with the maximum likelihood function target in CNS, and monitored using both the crystallographic R and cross-validating R-free statistics (95). The software suite PHENIX (96) was also employed for grouped B-factor (with two groups – main chain, and side chain) and TLS refinement. The model was manually adjusted using Coot (97) and $2F_o$-F_c and F_o-F_c electron density maps. The ligand model and definition files were generated using PRODRG (98), and were placed into electron density in the active site of both monomers in the asymmetric unit.

Animal Studies

Animal experiments were performed according to the Institutional Animal Care and Use guidelines approved by the Institutional Animal Care and Use Committee (IACUC # 20070715 and 20100711) of the Albert Einstein College of Medicine, Bronx, New York. This work was conducted by our collaborator, Dr. Sridhar Mani (Albert Einstein College of Medicine). CPT-11 was purchased from LC Laboratories, Woburn, MA (catalog number: I-4122) as a hydrochloride salt (> 99% HPLC purified grade). CPT-11 (20 mg/mL) and Inhibitor 5 (100 μg/mL) were dissolved in 0.25% (w/v) carboxymethylcellulose sodium salt (Sigma, C5013) to make stock solutions. As a vehicle control, all animals received an equivalent volume (compared to experimental groups) of 0.25% (w/v) carboxymethylcellulose sodium salt solution. BALB/cJ female mice (8-10 week old) were obtained from Jackson Laboratories, Bar Harbor, ME. The mice were housed in conventional metabolic cages (N=1/cage) and kept in a room under controlled temperature (20-22 ^{o}C) and 12 hour day-night cycle. Animals had free access to water and conventional food without fortification. Mice were divided into four groups of 9 animals each: Group 1, vehicle controls received equivalent volume of 0.25% (w/v)

carboxymethylcellulose sodium salt solution intraperitoneally (i.p.) and by oral gavage (~100 µL twice per day); Group 2, Inhibitor 5 gavaged (10 µg/day) twice per day (every 10 hours) starting on day ⁻1 with oral gavage of 0.25% (w/v) carboxymethylcellulose sodium salt solution, and i.p. once per day; Group 3, CPT-11 injected (50 mg/kg) i.p. once daily in the morning with oral gavage of 0.25% (w/v) carboxymethylcellulose sodium salt solution; Group 4, CPT-11 injected (50mg/kg) i.p. once daily in the morning, and Inhibitor 5 gavaged (10 µg/day) twice per day (every 10 hours). Total injected volume was identical for each animal. Mice were weighed and examined daily for signs of diarrhea (fecal staining of skin, lose watery stool) and bloody diarrhea (black sticky stool). Body weight, stool consistency and blood in stool were monitored daily using methods previously published (74, 99). Previous studies indicate that dosing at ~60-80 mg/kg/day of CPT-11 for 4 days allows for observation of delayed diarrhea around 15 days (100). A dosing scheme of 50 mg/kg/day, once daily for 9 days, was chosen with the intention of accelerating the onset of diarrhea while preventing death. As outlined previously, 50 mg/kg CPT-11 in mice is roughly equivalent to the 5 mg/kg typical human CPT- 11 dose based on differences in body surface area (63, 100). GI symptoms in Group 3 started as early as day 2 and up to day 10, and included decreased appetite, bowel movements, mobility and body weight. All animals were euthanized on day 11.

2.4 Results

2.4.1 *In vitro* and Cell-Based *E. coli* β-Glucuronidase Inhibition

Eight compounds (Inhibitors 1-8) were chosen from high-throughput screening results (74, 91) for further functional and structural characterization (**Figure 2.1**). Inhibitors 5-8 are relatively distinct in structure from one another and are also distinct from the four chemically-similar compounds (Inhibitors 1-4) reported previously (74). In *in vitro* assays with purified *E. coli* β-glucuronidase (*Ec*βG) using the substrate p-nitrophenyl glucuronide (PNPG), we found that all four compounds functioned as inhibitors, with IC_{50} and K_i values ranging from 180 nM (Inhibitor 5) to 15 µM (Inhibitor 7) **(Table 2.1)**, similar to those observed previously with Inhibitors 1-4 (74). Inhibitors 5, 6 and 8 were effective against the β-

glucuronidase target in living *E. coli* cells. Only Inhibitor 7, the weakest *in vitro* compound, showed no impact in cells, while Inhibitors 5, 6, and 8 exhibited 310 nM, 750 nM, and 1.2 µM EC_{50} values, respectively (**Table 2.1**). The relatively potent in-cell EC_{50} values compared to the *in vitro* IC_{50} values are likely due to differences in compound entry, metabolism, export, or partitioning within living cells; such features will be examined in future studies.

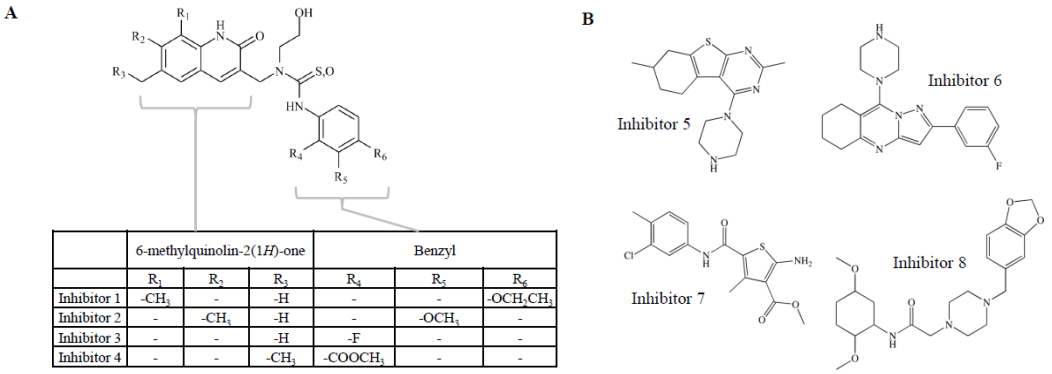

	6-methylquinolin-2(1*H*)-one			Benzyl		
	R_1	R_2	R_3	R_4	R_5	R_6
Inhibitor 1	$-CH_3$	-	-H	-	-	$-OCH_2CH_3$
Inhibitor 2	-	$-CH_3$	-H	-	$-OCH_3$	-
Inhibitor 3	-	-	-H	-F	-	-
Inhibitor 4	-	-	$-CH_3$	$-COOCH_3$	-	-

Figure 2.1. Chemical structures of **A)** Inhibitors 1-4, which share a common scaffold, and **B)** Inhibitors 5-8.

	*Ec*βG		*E. coli* cell-based
	K_i (nM)	IC_{50} (nM)	EC_{50} (nM)
Inhibitor 5	220± 40	540 ± 90	310 ± 8
Inhibitor 6	670 ± 30	8900 ± 3000	750 ± 200
Inhibitor 7	1900 ± 20	15000 ± 2000	NI
Inhibitor 8	960 ± 20	6400 ± 1000	1200 ± 300

Table 2.1. *In vitro* and cell-based assays for β-glucuronidase activity and inhibitor efficacy. Errors represent SEM, where $N = 3$. NI, no inhibition

2.4.2 *C. perfringens* and *S. agalactiae* β-Glucuronidase Activity and Inhibition

While *Ec*βG, the original target for screening for inhibitors, has been examined *in vitro* both structurally and with inhibitors, we now sought to examine β-glucuronidases obtained from other human GI-associated microbial species. Thus, the β-glucuronidases from *Clostridium perfringens* and *Streptococcus agalactiae* (*Cp*βG and *Sa*βG, respectively) were cloned, overexpressed and purified. While *E. coli* is part of the Proteobacteria phylum, these species belong to the Firmicute phylum, a major source of GI β-glucuronidase activity in humans.

They were initially assayed *in vitro* to determine their kinetic parameters, and those values were compared to *Ec*βG (**Table 2.2**). The k_{cat} values for *Ec*βG and *Sa*βG were found to be similar, at 40 and 24 sec^{-1}, respectively, while *Cp*βG exhibited a 10-fold slower turnover (k_{cat} = 2.6 sec^{-1}). Furthermore, *Sa*βG and *Cp*βG were both found to have reduced binding affinities for PNPG relative to *Ec*βG, exhibiting low-millimolar for *Cp*βG (K_M = 1.1 mM) to micromolar for *Sa*βG (K_M = 350 µM), while *Ec*βG demonstrated a low-micromolar (K_M = 160 µM) affinity. Thus, these three enzymes exhibit nearly a 100-fold difference in catalytic efficiency (k_{cat}/K_M), with *Ec*βG the best at 260 $sec^{-1}mM^{-1}$ (**Table 2.2**). Despite the reasonable sequence similarity between the enzymes (42-47% identity), their activities toward a glucuronidated substrate varies nearly two orders of magnitude.

	k_{cat}[a] (s^{-1})	K_M[b] (mM)	k_{cat}/K_M ($s^{-1}mM^{-1}$)
*Ec*βG	40 ± 1	0.16 ± 0.02	260
*Cp*βG	2.6 ± 0.6	1.1 ± 0.2	2.4
*Sa*βG	24 ± 1	0.35 ± 0.03	69

Table 2.2. Kinetic data were estimated by non-linear fitting using p-nitrophenyl glucuronide as the substrate. [a] *N* = 6 ± SEM**;** [b] *N* = 3 ± SEM

We next examined *Sa*βG and *Cp*βG in kinetic assays with Inhibitors 1-8 (**Table 2.3, Figure 2.1**). Inhibitors 5-8, which are not related to each other or to Inhibitors 1-4 in chemical structure (**Figure 2.1B**), exhibited more variability, including Inhibitor 7 and Inhibitor 8 that proved ineffective against these new species. Inhibitor 5 is the most potent exhibiting K_i values for *Sa*βG and *Cp*βG in the mid-nanomolar range (540 and 810 nM, respectively). Inhibitor 1 produced similar potency against *Sa*βG and *Cp*βG (K_i = 970 nM and K_i = 1400 nM, respectively). Interestingly, Inhibitor 7, which was effective at disrupting *Ec*βG (K_i = 1.9 µM), did not inhibit *Sa*βG and *Cp*βG. Similarly, Inhibitor 8 (K_i = 960 nM against *Ec*βG) did not inhibit *Cp*βG and only produced 30% inhibition at 100 µM with *Sa*βG (estimated K_i = 20 µM) (**Table 2.3**). Thus, while Inhibitors 1-6 demonstrated efficacy against the three microbial β-

glucuronidases purified to date (*Ec*βG, *Sa*βG and *Cp*βG), Inhibitors 7 and 8 indicate that certain chemical scaffolds will exhibit selectivity toward specific β-glucuronidase orthologues.

	in vitro K_i	
	*Sa*βG	*Cp*βG
Inhibitor 1	0.97 ± 0.1	1.4 ± 0.4
Inhibitor 2	1.1 ± 0.5	3.0 ± 1
Inhibitor 3	7.8 ± 0.9	11 ± 3
Inhibitor 4	24 ± 3	36 ± 5
Inhibitor 5	0.54 ± 0.2	0.81 ± 0.2
Inhibitor 6	6.1 ± 2	2.8 ± 0.3
Inhibitor 7	NI	NI
Inhibitor 8	NI	NI

Table 2.3. Enzyme inhibition properties of small molecule inhibitors against representative β-glucuronidase enzymes from the mammalian microbiome. Data are presented as the average ($N > 3$) ± SEM. NI: no inhibition.

2.4.3 Selectivity for Bacterial β-Glucuronidase

We next tested the ability of Inhibitors 5-8 to disrupt the activity of purified β-glucuronidase from bovine liver, a mammalian enzyme orthologue**.** We found that Inhibitors 5-8 were ineffective at concentrations up to 100 μM (**Figure 2.2**). These same results were previously seen for Inhibitors 1-4 (74). Using the appropriate substrate, we additionally probed the *in vitro* effects of these compounds on related glycoside hydrolases, which included four commercially-available enzymes: a plant β-glucosidase (from the almond tree *Prunis dulcis*), a mollusk β-mannosidase (from *Helix pomatia*), and β-galactosidases from *E. coli* and bovine sources. In all cases, Inhibitors 1-8 failed to exhibit inhibition at compound concentrations up to 100 μM (data not shown). Thus, we conclude that the β-glucuronidase inhibitors, Inhibitors 1-8, do not inhibit either mammalian β-glucuronidase or members of the related family of sugar-cleaving enzymes from a range of sources, demonstrating selectivity.

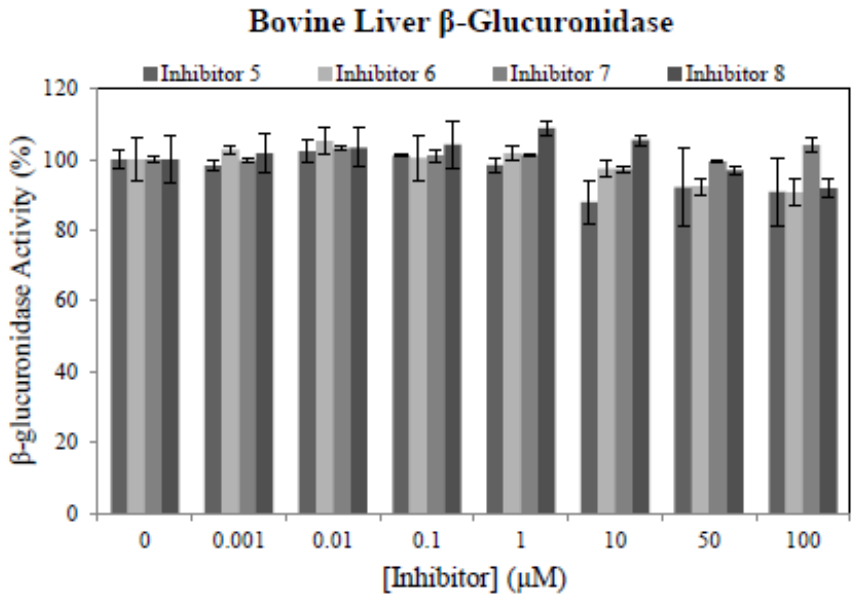

Figure 2.2. Impact of increasing concentrations of Inhibitors 5-8 on the activity of a representative mammalian β-glucuronidase.

2.4.4 Lethality to Bacterial and Mammalian Cells

Disruption of GI-associated microbial β-glucuronidases in order to eliminate toxic drug metabolites but maintain proper physiology requires that compounds are not toxic. Therefore, we tested the potential lethality of Inhibitors 5-8 to cultured *E. coli* or HCT116 human colon cancer cells at compound concentrations up to 100 μM. We found that all four inhibitors did not affect the survival of either *E. coli* or HCT116 cells (**Figure 2.3**). Thus, they appear to satisfy the criteria that successful compounds are relatively non-toxic to bacterial or human epithelial cells.

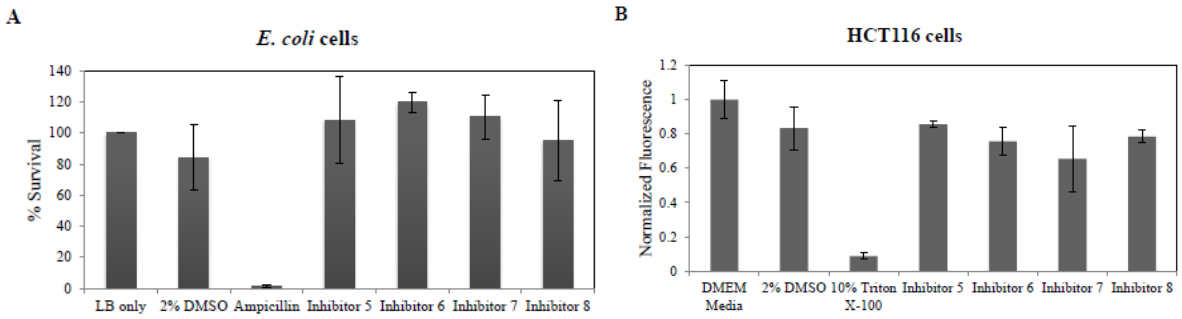

Figure 2.3. Impact of Inhibitors 5-8 at 100 μM on the survival of *E. coli* (**A**) and HCT116 cells (**B**). Ampicillin and 10% Triton-X100 are used as positive controls for microbial and human cell lethality, respectively. DMSO, in which the inhibitors are solubilized, is also shown.

2.4.5 Structure of *Ec*βG in Complex with Inhibitor 8

To further the understanding of the molecular basis of *Ec*βG inhibition, we determined the 2.8 Å resolution crystal structure of the enzyme in complex with Inhibitor 8 (PDB ID 4JHZ) (**Table 2.4**). The asymmetric unit contained two β-glucuronidase monomers (**Figure 2.4A**), while C2 crystallographic symmetry produced the physiologically relevant β-glucuronidase tetramer (74). The apo (unliganded) structure of *Ec*βG was used as a molecular replacement search model to eliminate any previous ligand model bias. After careful refinement of the protein structure, electron density at 1.0 σ level in the composite omit map was present for Inhibitor 8 in both monomers of the asymmetric unit (**Figure 2.4B**). After refinement of the atomic positions as well as their thermal displacement parameters (B-factors), the ligands had an occupancy of 0.93 and 0.91 with an average B-factors of 66.4 $Å^2$ and 76.5 $Å^2$ for chain A and B, respectively.

Data Collection	
Structure	*Ec*βG – Inhibitor 8
X-ray source	APS ANL, SER-CAT 22-ID
Space group	C2
Unit cell: a, b, c (Å); α, β, γ (°)	168, 77, 126; 90, 125, 90
Resolution (Å) (highest shell)	41.8 - 2.83 (2.93 - 2.83)
I/σ	10.1 (2.22)
Completeness (%)	99 (97)
Redundancy	4.1 (3.7)
Refinement	
Resolution (Å)	41.8 - 2.83
No. of unique reflections	31648 (3115)
R_{work}	0.196 (0.265)
R_{free}	0.244 (0.329)
Molecules per asymmetric unit (AU)	2 *Ec*βG, 2 Inh8
No. of amino acids per AU	1192
No. of waters per AU	124
R.M.S. deviations	
Bond lengths (Å)	0.006
Bond angles (°)	1.02
Ramachandran (%)	
Favored	93
Allowed	6.6
Outliers	0.42

Table 2.4. Crystallographic Statistics of full-length *Ec*βG in complex with Inhibitor 8.

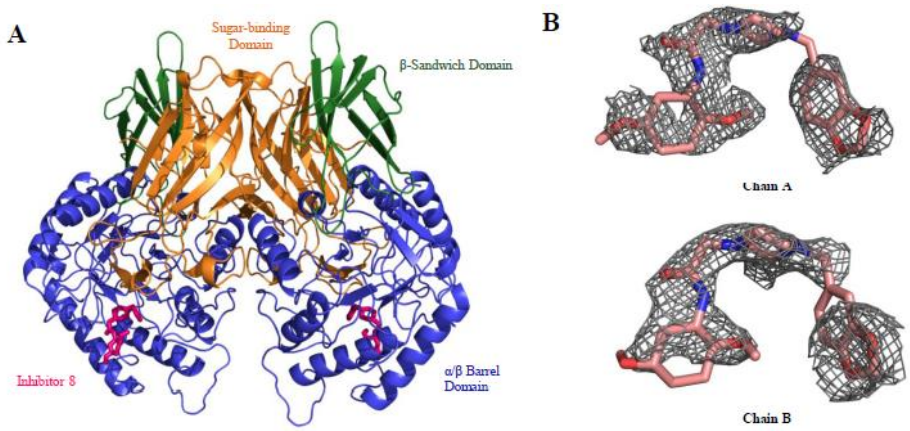

Figure 2.4. A. Crystal structure of the *Ec*βG dimer in complex with Inhibitor 8 (PDB ID 4JHZ). **B.** Composite annealing omit (σA-weighted) 2.8 Å resolution electron density contoured at 1.0 σ for Inhibitor 8 in the active site of each monomer of *Ec*βG.

Inhibitor 8 was placed in an orientation that both satisfies the electron density and makes chemically reasonable interactions with the neighboring amino acid side chains. It binds to the entrance to the active site cleft (**Figure 2.4A**), contacting Asp-163, Val-446, Phe-448, Tyr-472, and Arg-562 within the active site region of the enzyme and 3.5 Å from the catalytic residue Glu-413 residue (**Figure 2.5**). Notably, in chain A it directly contacts Leu-361 of the "bacterial loop," a region that is unique to the microbial forms of the β-glucuronidase relative to the mammalian β-glucuronidases (74, 101). Inhibitor 8 binds in a similar manner to Inhibitors 2 and 3 described previously in complexes with *Ec*βG (74), occupying a similar location in the enzyme and contacting 5 of the same residues (**Figure 2.5**). Indeed, the root-mean-square deviation between the Cα positions of the Inhibitor 2- and Inhibitor 8-bound structures of *Ec*βG is 0.54 Å. However, while most residues contacted by Inhibitor 8 are in the same position in the Inhibitor 2 complex structure, the side chain of Leu-361 shifts by 3.6 Å. This observation suggests that the "bacterial loop" is capable of conforming to the presence of different bound ligands. Electron density in the simulated annealing omit and $2F_o$-F_c maps is less complete for Leu-361 in chain B compared to chain A.

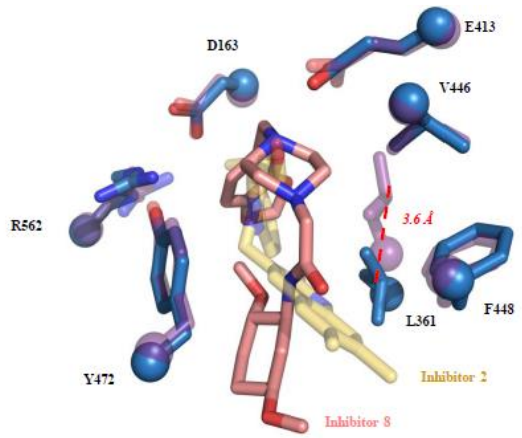

Figure 2.5. Contacts formed by Inhibitor 8 (pink) at the active site of *Ec*βG. Inhibitor 2 (yellow) from a previously resolved structure is also shown, as are the side chains for the Inhibitor 8 and Inhibitor 2 complexes (blue and purple, respectively).

The full "bacterial loop" of *Ec*βG, residues 360-376, was visualized in the Inhibitor 2 and 3 co-crystal structures (74); in complex with Inhibitor 8, though, only residues 372-376 are ordered with average B-factors less than 80 $Å^2$ (**Figure 2.6A**). In the absence of a bound ligand, the "bacterial loop" is not observed, as it gave no interpretable electron density in the structure of apo *Ec*βG reported previously (74). Thus, we conclude that *Ec*βG can be inhibited effectively by compounds, like Inhibitor 8, capable of contacting a portion of the loop unique to the microbial β-glucuronidases. In support of this conclusion, we found that a form of *Ec*βG in which the "bacterial loop" was deleted, Δ360-376, was not inhibited by up to 100 μM of Inhibitors 5-8 (**Figure 2.6B**). The Δ360-376 *Ec*βG exhibited comparable K_M (260 μM for Δ360-376, 360 μM for wild-type) values, but the k_{cat} (0.24 sec^{-1} for Δ360-376, 40 sec^{-1} for wild-type) values were reduced by 2 orders of magnitude. Thus, the "bacterial loop" is essential for full activity of *Ec*βG, as well as its selective inhibition.

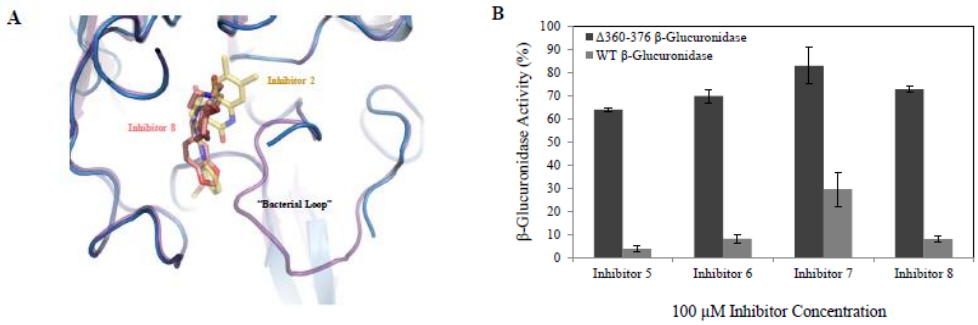

Figure 2.6. A. Bound Inhibitor 8 (pink) adjacent to the largely disordered "bacterial loop" of *Ec*βG (blue). The completely ordered "bacterial loop" of *Ec*βG (purple) in complex with Inhibitor 2 (yellow) is overlaid for comparison. The image is in the same orientation as Figure 5 **B.** Inhibitors 5-8 at 100 μM inhibit wild-type (WT) *Ec*βG, but not a mutant *Ec*βG in which the "bacterial loop" (residues 360-376) has been deleted.

2.4.6 Structural Comparison of *Sa*βG and *Cp*βG to *Ec*βG in Complex with Inhibitor 8

Overlaying the structure of *Ec*βG in complex with Inhibitor 8 with un-liganded *Cp*βG, steric clashes appear from residues in *Cp*βG against the Inhibitor 8 binding site (**Figure 2.7A**). A slight clash is created by the *Cp*βG active site residue Leu-447, but a much larger clash can be seen from Met-364, part of the "bacterial loop". Overlaying the *Sa*βG $P2_12_12$ structure (**Figure 2.7B**), steric clashes between Inhibitor 8 and Met-444 and Leu-443 residues are seen. In the *Sa*βG I222 structure (**Figure 2.7B**), however, there is a slight clash between Inhibitor 8 and residue Met-444, but Leu-443 is in a slightly different conformation that eliminates the clash seen in the *Sa*βG $P2_12_12$ structure. This discrepancy between the two *Sa*βG structures provides a potential mechanism for the partial inhibition of Inhibitor 8 against purified *Sa*βG.

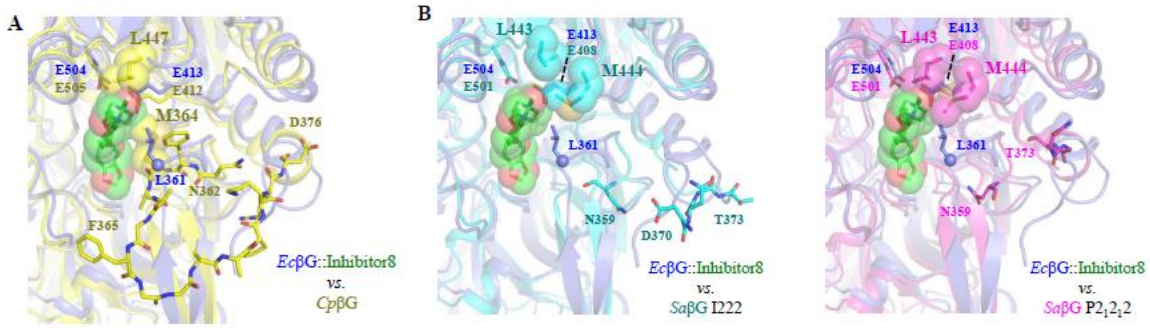

Figure 2.7. (A) Aligned structures of *Ec*βG Inhibitor 8-bound (Inh8) structure with *Cp*βG highlighting the "bacterial loop" region. Key residues adjacent to the inhibitor binding site are displayed. Steric clashes between key residues in the *Cp*βG structure and the bound Inhibitor 8 molecule from the *Ec*βG structure are emphasized with spheres. **(B)** Aligned structures of *Ec*βG Inhibitor 8-bound structure with the two *Sa*βG crystal structures. Key residues adjacent to the inhibitor binding site are displayed. Steric clashes between key residues in the two *Sa*βG structures and the bound Inhibitor 8 molecule from the *Ec*βG structure are emphasized with spheres.

Although the active sites of the *Cp*βG and *Sa*βG structures are unchanged with respect to published *Ec*βG-bound structures, the binding site for Inhibitors 5-8 are more divergent. **Figure 2.8** depicts the active site residues directly surround the bound Inhibitor 8 in the *Ec*βG structure. A structural alignment of the *Cp*βG and two *Sa*βG structures reveals both similarities and differences in amino acid composition and side chain conformations surrounding Inhibitor 8. Conserved residues in *Cp*βG include the active site residues Glu-413 and Glu-504, as well as the additional residues Asp-164, Thr-557, Ser-558, Arg-563, Tyr-468, Val-473, and Tyr-472. Similar to the *E. coli* structure, Ile-562, Met-364, Leu-447, and Met-448 provide hydrophobic contacts. The *Sa*βG inhibitor binding site also consists of Asp-160, Thr-553, Arg-559, Leu-558, Tyr-468, Val-469, Tyr-464, and the catalytic residues Glu-413 and Glu-504, all of which are conserved in the *Ec*βG enzyme for bound inhibitors.

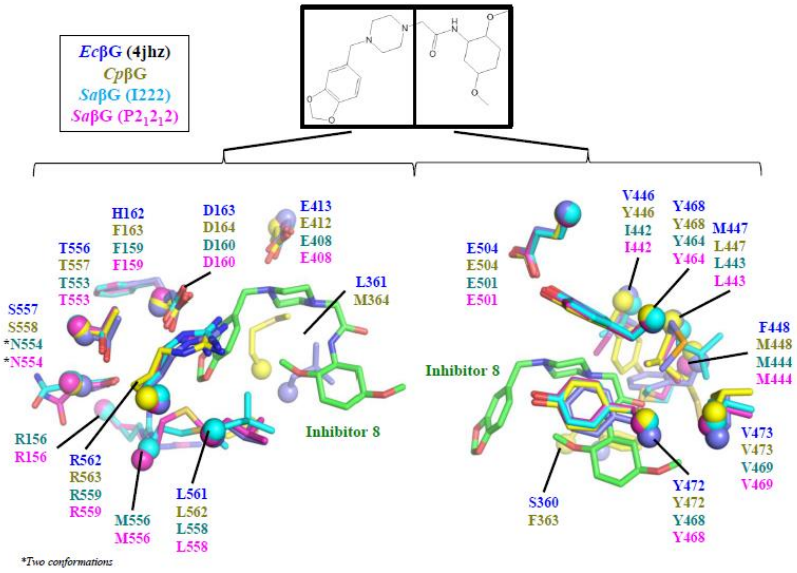

Figure 2.8. Structural overlay of the β-glucuronidase structures reported here along with the active site of the Inhibitor 8-bound *Ec*βG structure. Residues that interact on both sides of the Inhibitor 8 molecule are predicted to be highly conserved spatially, and nearly identical as well.

A number of differences in the environment surrounding the inhibitor binding site are observed when comparing the *Ec*βG to the *Cp*βG and *Sa*βG structures (**Figures 2.8**). Surrounding the 1,3-benzodioxol moiety for Inhibitor 8, *Cp*βG and *Sa*βG have a phenylalanine (Phe-163 and Phe-159) in place of His-162 in the *Ec*βG enzyme. Furthermore, the *Sa*βG enzyme has Asn-554 in two conformations, replacing the Ser-557 and Ser-558 found in the *Ec*βG and *Cp*βG structures, respectively. Encompassing the 2,5-dimethoxycyclohexyl moiety for Inhibitor 8, the *Cp*βG enzyme has Tyr-446 and Phe-363 that replace Val-446 and Ser-460 in *Ec*βG. Side-chain conformations of residues in the *Sa*βG and *Cp*βG structures that do not align well with the *Ec*βG residues detail areas that may limit strong inhibitor binding.

2.4.7 Alleviation of CPT-11 Toxicity in Mice

We tested the ability of the most potent compound examined in this study, Inhibitor 5 (K_i = 180 nM, EC_{50} = 300 nM), to alleviate CPT-11-induced intestinal toxicity in mice. We divided BALB/cJ female mice into four groups of nine animals each. Group 1 received an equivalent volume of only the vehicle (0.25% (w/v) carboxymethylcellulose sodium salt solution) intraperitoneally (i.p.) and by oral

gavage twice per day. Group 2 received an oral gavage of Inhibitor 5 (10 μg/day) twice per day starting on day ⁻1, as well as an i.p. injection of the vehicle solution once per day. Group 3 was injected with CPT-11 (50 mg/kg) i.p. once per day and received an oral gavage of the vehicle solution twice per day. Group 4 received both an injection of CPT-11 (50 mg/kg) once per day and an oral gavage of Inhibitor 5 (10 μg/day) twice per day. The mice were observed and weighed daily, and were examined for incidence of diarrhea and bloody diarrhea (**Figure 2.9**). Groups 1 and 2 showed no evidence of toxicity throughout the experiment. In group 3, GI symptoms were observed as early as day 2 and incidences of bloody diarrhea were observed in a third of the mice at day 8, and in all animals by day 10. In comparison, in group 4, where the mice were pretreated with Inhibitor 5, no mice showed evidence of bloody diarrhea by day 8 and less than 30% of mice showed symptoms by day 10 (**Figure 2.9A**).

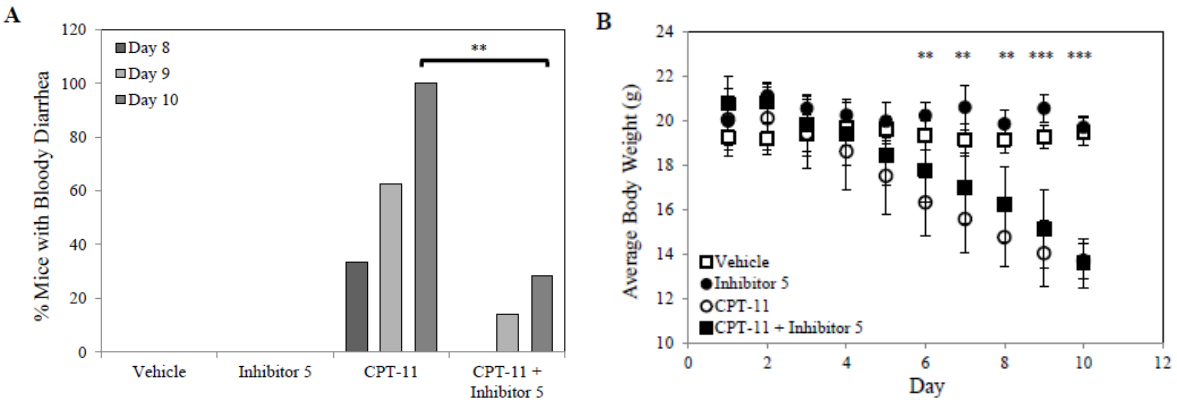

Figure 2.9. A. Groups of nine BALB/cJ mice were dose with either vehicle, Inhibitor 5, CPT-11, or pre-treated with Inhibitor 5 followed by CPT-11, and then examined for incidences of CPT-11-induced toxicity (i.e., bloody diarrhea). **B**. The mice were weighed daily. Administration of CPT-11 incited the loss of body weight during treatment. Oral administration of Inhibitor 5 had no protective effects on body weight during CPT-11 treatment. The Inhibitor 5 only and CPT-11 + Inhibitor 5 groups were analyzed for statistical significance. **, $p < 0.01$ and ***, $p < 0.001$

The body weight of each mouse was also recorded each day during the course of the experiment (**Figure 2.9B**). Although Inhibitor 5 alleviated most of the toxicity associated with the CPT-11 treatment, it had no effect on the average body weight of the mice. Moreover, group 2, which only received treatment with Inhibitor 5, showed comparable body weights to the vehicle-only group, but had significantly higher body weights, starting at day 6, than group 4, which received treatment with Inhibitor 5 in addition to CPT-11. These data indicate that the presence of Inhibitor 5 significantly reduces the incidence of acute GI toxicity caused by CPT-11, and they suggest that Inhibitor 5 does not impact the systemic effects of this anticancer drug, as measured by weight loss.

2.5 Discussion

Research endeavors like the Human Microbiome Project continue to expand the appreciation of the roles the symbiotic microbiota play in mammalian physiology (1). It also appears that widespread use of antibiotics may have subtle but serious side effects on human health (102). Additionally, for patients with colorectal cancer, the use of antibiotics to treat CPT-11-induced toxicity may lead to the increased prevalence of subdominant bacterial species with higher overall β-glucuronidase activity in the GI tract,

and thus, increased toxicity (63). Studies have also shown that the long-term use of neomycin in mice leads to increased serum bilirubin that may interfere with proper hepatic CPT-11 metabolism (103). These observations lead to the conclusion that the selective, non-lethal inhibition of components of the GI microbiome will be an important method of enhancing drug efficacy and tolerance. In this report, we interrogate the roles bacterial β-glucuronidases play in mammalian GI drug toxicity by pharmacologically targeting this enzyme with potent and selective inhibitors.

Inhibitors 5-8 exhibited strong *in vitro* inhibition of *Ec*βG (**Table 2.1**) but did not affect the viability of either cultured bacterial or mammalian cells (**Figure 2.3**). Only Inhibitor 7 failed to disrupt β-glucuronidase activity in living *E. coli* cells. Furthermore, because compounds were ineffective against mammalian β-glucuronidase (**Figure 2.2**) and a range of enzymes from the glycosidase family, each inhibitor displayed selectivity toward *Ec*βG. The selectivity of the inhibitors is particularly critical because human β-glucuronidase expressed by tumor cells appears to play an important role in the anti-tumor efficacy of CPT-11 through the reactivation of SN-38G to SN-38 in the tumor microenvironment (88, 104). Of Inhibitors 5-8, only Inhibitor 5 (K_i = 180 nM, IC_{50} = 540 nM) displayed potency comparable to previously-characterized inhibitors, which have a scaffold not shared by the four inhibitors outlined in this study (74).

Because β-glucuronidase activity has been shown in a range of bacterial species, we purified β-glucuronidases from *Clostridium perfringens* and *Streptococcus agalactiae*, symbiotic species known to populate the human GI tract. Moreover, these enzymes belong to a different phylum (Firmicute) than the orthologous *Ec*βG protein (Proteobacteria), but share a 42-47% sequence identity and high degree of structural conservation. Kinetic analysis shows that *Cp*βG and *Sa*βG are slower enzymes than *Ec*βG. *Sa*βG has a 10-fold decrease in catalytic efficiency, while *Cp*βG is 100-fold slower. Mutagenesis studies, likely focused on divergent residues in the "bacterial loop," will be required to understand these observed differences in activity. Each of the eight inhibitors was additionally tested against these newly purified enzymes. Only Inhibitors 1 and 5 maintained potency, and Inhibitors 7 and 8 proved ineffective. As such,

these data advance the understanding of the chemical moieties capable of selective bacterial β-glucuronidase inhibition.

Contributing to the mechanism of *Ec*βG inhibition that includes the structures of the complexes of Inhibitors 2 and 3 reported previously (74), we successfully determined the x-ray crystal structure of one inhibitor (Inhibitor 8) in complex with *Ec*βG (**Figure 2.4**). Similar to those structures, Inhibitor 8 binds at the entrance to the active site cleft and forms related contacts, including one with the catalytic glutamic acid residue, Glu-413. Importantly, Inhibitor 8 also makes a hydrophobic contact with Leu-361, which is part of the "bacterial loop" unique to the microbial enzymes. Overlaying the structures of the complexes with Inhibitor 2 and Inhibitor 8, it is apparent that Leu-361 has shifted to facilitate binding, suggesting that "bacterial loop" flexibility is involved in inhibition (**Figure 2.6**). The observation that the "bacterial loop" in the Inhibitor 8 complex structure is disordered for the eight residues C-terminal to Leu-361 supports that conclusion. Mutagenesis studies in which the "bacterial loop" has been deleted confirm its importance in microbial β-glucuronidase inhibition (**Figure 2.6**).

Unlike Inhibitors 1-4, Inhibitors 5-8 do not share a common scaffold from which to draw conclusions about their mechanism of inhibition or non-inhibition. Using the x-ray crystal structure of *Ec*βG in complex with Inhibitor 8, we can begin to draw conclusions as to why Inhibitor 8 is not an inhibitor for *Cp*βG and only a partial inhibitor for *Sa*βG. By overlaying the Inhibitor 8-bound *Ec*βG structure with the *Cp*βG and *Sa*βG structures (**Figure 2.7**), we hypothesize that differences in the structure and conformation of active site residues in *Cp*βG and *Sa*βG obstruct binding of the Inhibitor 8 molecule, and thus, prevent inhibition.

Only the previously reported Inhibitor 1 had been examined to date in drug-induced GI toxicity studies in mice (74, 85). In this report, we tested the *in vivo* efficacy of the most effective compound outlined here, Inhibitor 5, in a mouse model of CPT-11 toxicity (**Figure 2.9**). Groups of BALB/cJ mice were dosed with Inhibitor 5, CPT-11, or a combination of both. The group that received CPT-11 alone developed bloody diarrhea by day 8, and 100% of the mice showed signs of this toxicity by day 10. The group that was treated with Inhibitor 5 orally, along with CPT-11 by i.p., had significantly fewer incidents

of bloody diarrhea compared to the CPT-11 group, highlighting the protective effects of Inhibitor 5. It is also interesting to note that the mice that received CPT-11 lost body weight at the same rate regardless of treatment with Inhibitor 5. This suggests that Inhibitor 5 protects against CPT-11-induced GI toxicity, but the pharmacodynamics of CPT-11 in the mouse are not impacted. A more comprehensive examination of tumor xenografts and pharmacokinetics will be required to substantiate this conclusion.

We have described the inhibitory profile of a range of chemically-distinct compounds and assessed their potential as orally delivered pharmacological agents. They are *in vitro* inhibitors with varied potencies to the tested bacterial β-glucuronidases and, with the exception of Inhibitor 7, are also effective in *E. coli* cells. Moreover, the inhibitors appear to be selective for bacterial β-glucuronidase and non-lethal to bacterial and mammalian cells. The structural data presented here, along with the data from previously-characterized inhibitors, will allow us to better understand their mechanism of selective microbial β-glucuronidase inhibition. As such, they may facilitate the development of therapeutics capable of alleviating drug-induced GI toxicity generated by symbiotic microbial β-glucuronidases.

Chapter 3

Novel Inhibitors Designed Toward Altered Pharmacokinetic Properties Using Structural and Chemical Biology

3.1 Summary

Prior work has demonstrated the ability and the utility in designing small-molecule inhibitors that target a symbiotic microbial enzyme for a therapeutic outcome. Certain drugs, most notably NSAIDs and the widely-used anti-cancer drug CPT-11, are hampered by gastrointestinal toxicities that limit the drugs' efficacy and may potentially be fatal. In each case, a microbial enzyme, β-glucuronidase, has been implicated in mediating toxicities. Our lab has worked on developing selective, non-toxic inhibitors of β-glucuronidase to alleviate these toxic side effects. We have demonstrated the utility of the system in models of CPT-11-induced diarrhea and in models of NSAID-induced intestinal injuries. Here, we continue the development of a potential therapeutic by rationally designing inhibitor analogues of a lead compound to decrease intestinal absorption and increase the amount of compound that reaches the intestinal microbiota. The design successfully decreased the bioavailability of inhibitors in mice, but the analogues suffered from a loss of *in vitro* potency that led to a decrease in *in vivo* efficacy. Preliminary *in vivo* studies using xenografted tumors in mice indicate that the system of inhibition does not negatively affect the pharmacokinetic profile or the anti-tumor ability of CPT-11.Further work is needed to establish improved CPT-11 efficacy with reduced toxicity.

3.2 Introduction

Although the need to maintain a healthy microbiota is becoming increasingly appreciated, one area that the microbiota play a clear and direct role in a negative outcome for humans is drug-induced toxicity (32, 33, 63, 79). Xenobiotic compounds, ingested or otherwise administered, are typically detoxified in the liver, first through oxidation (Phase I), and then through conjugation (Phase II) with an often polar moiety. These inactive metabolites are then circulated through the bile system to be excreted. However, enzymes expressed by the host microbiota in the intestinal tract are able to reverse the detoxifying conjugation reaction, reactivating the parent drug, before the compounds are harmlessly excreted (82, 87). Although this reaction is beneficial in some cases through enterohepatic circulation and an increase in the amount of active drug in systemic circulation over a longer period of time, the reaction may also engender toxic side effects locally in the intestinal tract. Importantly, in combination with increasing appreciation of the interplay between microbiota and host metabolism, the key players present in the microbiome are, for the first time, viewed as drug targets for a therapeutic outcome for the host (90).

Although we have since begun to investigate additional models of drug-induced toxicity, work from our lab had first focused on the dose-limiting side effect of the anti-cancer drug, CPT-11. Given intravenously, CPT-11 is a prodrug for its active metabolite, SN-38, which is subsequently detoxified in the liver through conjugation with UDP-glucuronic acid, producing SN-38-glucuronide (SN-38G) (58). This inactive metabolite then acts a substrate for a microbial enzyme, known as β-glucuronidase, which hydrolyzes the glucuronide moiety as a source of carbon and reproduces the active metabolite, SN-38, into the intestinal lumen, which is then taken up into the intestinal epithelial cells, where it mediates cell damage and death (63, 105). Indeed, the same traits that make CPT-11 such an effective anti-cancer treatment also make it quite toxic to healthy cells.

We have developed microbial-specific β-glucuronidase inhibitors (74, 106). Previous work has outlined the discovery and biochemical characterization of a group of putative inhibitors against β-glucuronidases purified from GI-associated bacteria, but in this work, we seek to expand the

understanding of the *in vivo* effects of the inhibitors. We also outline initial attempts at developing chemical modifications to lead compounds in order increase their *in vivo* efficacy and the successes and pitfalls that came with those attempts. Lastly, we move forward with the lead compound into *in vivo* efficacy studies.

3.3 Materials and Methods

Reagents

The assay substrate p-nitrophenyl β-D-glucuronide (PNPG) and bovine liver β-glucuronidase were purchased from Sigma-Aldrich (St. Louis, MO). β-glucuronidase (EC 3.2.1.31) from *E. coli, S. agalactiae,* and *C. perfringens* (*Ec*βG, *Sa*βG, and *Cp*βG, respectively) were expressed and purified as described previously (74). Purified β-glucuronidase was stored in 20 mM HEPES, 50 mM NaCl, pH 7.4 at ~10 mg/mL at $^{-}80\ ^{o}C$. Inhibitors 1-8 were synthesized by Asinex, Inc. (Winston-Salem, NC). Inhibitors were identified by high-throughput screening and secondary validation was performed in-house (37).

Kinetic and Equilibrium Inhibition Assays.

Inhibition assays were conducted by measuring the β-glucuronidase-catalyzed conversion of PNPG to p-nitrophenol (PNP). PNPG was stored by dissolving in water at 250 mM. The conversion of increasing concentrations of PNPG to PNP, in the presence of 10 nM enzyme, was measured in the presence of increasing concentrations of putative inhibitors; zero-substrate and zero-inhibitor controls were carried out at the same time. Reactions were conducted in 96-well, clear-bottom assay plates (Costar, Tewksbury, MA) at 37 ^{o}C in 50 µL of total volume. The reaction consisted of 10 µL of assay buffer (5% DMSO and 500 mM HEPES, pH 7.4), 5 µL of inhibitor solution (various concentrations), 5 µL of 100 nM enzyme, and 30 µL of substrate (various concentrations). Product formation was calculated by measuring the change in absorbance over time at 410 nm using a PHERAstar *Plus* microplate reader (BMG Labtech, Ortenberg, Germany). The acquired data were analyzed using Microsoft Excel and Sigmaplot 11.0. From these data, K_i values were calculated for each of the inhibitors.

A related assay was employed to calculate the IC_{50} values in the following manner. An analogous 50 µL reaction, consisting of enzyme (1 nM final), buffer, PNPG (1 mM final), and variable concentrations of the inhibitors, was incubated at 37 ^{o}C for 6 hours to allow the reaction to reach equilibrium and then quenched with 100 µL 0.2 M sodium carbonate. The percent inhibition for each concentration of inhibitor was calculated based on changes in absorbance and used to plot a dose-response curve. The IC_{50} value was calculated as the concentration of inhibitor that produced 50% *in vitro* inhibition. The same assay was performed with purified bovine liver β-glucuronidase with PNPG as the substrate.

We also tested the ability of these compounds to inhibit β-glucuronidase activity in *E. coli* cells. We grew HB101 *E. coli* cells, transformed with the pET-28a vector containing the β-glucuronidase gene, to an OD_{600} of 0.6 in LB medium and used a small aliquot in an assay similar to the *in vitro* IC_{50} assay described above. The cells (39 µL) were incubated with 1 µL of variable concentrations of inhibitor and 10 µL of 1 mM PNPG at 37 ^{o}C for 6 hours. The reaction was quenched with 100 µL 0.2 M sodium carbonate. The amount of substrate turnover and therefore the amount of inhibition is calculated from the change in absorbance compared to zero-inhibitor controls. EC_{50} values were calculated as the amount of inhibitor necessary to produce 50% inhibition. The *in vitro* and cell-based assays employed here were similar to those reported previously (74).

Toxicity of Inhibitors toward Cultured Cells

The toxicity of inhibitors to bacterial cells was examined by incubating HB101 *E. coli* cells, transformed with the pET-28a vector containing the β-glucuronidase gene, grown to an OD_{600} of 0.6 in LB medium with each compound, as well as DMSO and ampicillin as controls, for 6 hours. Cell survivability was measured by plating a 10^{-5} dilution of the cells on LB media enriched with kanamycin. After overnight incubation, colonies were counted to quantify cell viability. We used a similar assay to assess the inhibitor's toxicity toward cultured HCT116 human colon cancer cells, which were grown and cultured in DMEM media. Aliquots of HCT116 cells were incubated with 100 µM of each lead for 24 hours. The resulting viability of the cells was quantified by using the CellQuanti-Blue™ Cell Viability

Assay Kit (BioAssay Systems, Hayward, CA). Cells are incubated with CellQuanti-Blue™ Reagent and fluorescence was measured.

Crystal Structure Determination

Crystals of *Ec*βG were obtained at 2 mg/mL protein with 30-fold molar excess Inhibitor R1 in 16% PEG-3350 (w/v), 200 mM magnesium acetate, and 0.02% sodium azide (w/v) at 16 °C. Crystals first appeared after 5 days, and were immediately cryo-protected with perfluoropolyether vacuum pump oil (Sigma-Aldrich, St. Louis, MO) and flash-cooled in liquid nitrogen. Diffraction data were collected on the 23-ID beam line at GM/CA-CAT (Advanced Photon Source, Argonne National Laboratory). Data in space group C2 were indexed and scaled using HKL2000 (93) to 2.39 Å resolution. The asymmetric unit contained two monomers. The structure was determined with Phaser (94) using molecular replacement with the apo *Ec*βG structure (PDB ID 3K46) as a search model. The structure was refined using simulated annealing and torsion angle refinement with the maximum likelihood function target in CNS, and monitored using both the crystallographic R and cross-validating R-free statistics (95). The software suite PHENIX (96) was also employed for B-factor and TLS refinement. The model was manually adjusted using Coot (97) and $2F_o$-F_c and F_o-F_c electron density maps. The ligand model and definition files were generated using PRODRG (98) and were placed into electron density in the active site of both monomers in the asymmetric unit.

Toxicity Studies in Mice

Animal experiments were performed according to the Institutional Animal Care and Use guidelines approved by the Institutional Animal Care and Use Committee of the Albert Einstein College of Medicine, Bronx, New York. CPT-11 (20 mg/mL) and Inhibitor R1 (100 μg/mL) were dissolved in 0.25% (w/v) carboxymethylcellulose sodium salt to make stock solutions. As a vehicle control, all animals received an equivalent volume (compared to experimental groups) of 0.25% (w/v) carboxymethylcellulose sodium salt solution. BALB/cJ female mice were divided into four groups: Group 1, vehicle controls received equivalent volume of 0.25% (w/v) carboxymethylcellulose sodium salt solution intraperitoneally (i.p.) and by oral gavage (~100 μL twice per day); Group 2, Inhibitor R1

gavaged (10 µg/day) twice per day (every 10 hours) starting on day ¯1 with oral gavage of 0.25% (w/v) carboxymethylcellulose sodium salt solution, and i.p. once per day; Group 3, CPT-11 injected (50 mg/kg) i.p. once daily in the morning with oral gavage of 0.25% (w/v) carboxymethylcellulose sodium salt solution; Group 4, CPT-11 injected (50mg/kg) i.p. once daily in the morning, and Inhibitor R1 gavaged (10 µg/day) twice per day (every 10 hours). Total injected volume was identical for each animal. Mice were examined daily for signs of diarrhea (fecal staining of skin, lose watery stool) and bloody diarrhea (black sticky stool) using methods previously published (74, 99). Previous studies indicate that dosing at ~60-80 mg/kg/day of CPT-11 for 4 days allows for observation of delayed diarrhea around 15 days (100). A dosing scheme of 50 mg/kg/day, once daily for 9 days, was chosen with the intention of accelerating the onset of diarrhea while preventing death. As outlined previously, 50 mg/kg CPT-11 in mice is roughly equivalent to the 5 mg/kg typical human CPT- 11 dose based on differences in body surface area (63, 100).

Bioavailability Studies in Mice

Healthy male Swiss Albino mice (10-12 weeks old) purchased from In Vivo Biosciences were divided into 4 groups of 4 mice each. The first group received a control IV dose of Inhibitor 1. The second group was pretreated with an oral dose of a formulation of 1-aminobenzotriazole (ABT) at 50 mg/kg 2 hours prior before receiving an IV dose of Inhibitor 1. The third group received an oral dose of Inhibitor 1 in a suspension formulation at 3 mg/kg. The fourth group received the same oral dose of Inhibitor 1 but was first treated with the same formulation of ABT as group two. The first and third groups received a control oral dose of vehicle in place of ABT treatment. Blood samples (approximately 60 µL) were collected at set time intervals (0.08, 0.25, 0.5, 1, 2, 4, 8, and 24 hr) after treatment with Inhibitor 1. Plasma was immediately harvested via centrifugation after collection of blood samples and store at -70 ^{o}C before analysis. Protein were precipitated from samples using acetonitrile and analyzed by LC-MS/MS.

PK Studies in Mice

Healthy mice received the same dosing schedule as the toxicity studies outlined previously. In short, groups of mice received either vehicle (0.25% (w/v) carboxymethylcellulose sodium salt solution), CPT-11 (injected 50 mg/kg i.p. once daily in the morning with oral gavage of 0.25% (w/v) carboxymethylcellulose sodium salt solution), or CPT-11 plus Inhibitor 1 (CPT-11 injected 50mg/kg i.p. once daily in the morning, and Inhibitor 1 gavaged orally 10 μg/day twice per day every 10 hours). Plasma samples were taken at regular time intervals. Samples were analyzed by mass spectrometry (Thermo LTQ Orbitrap Discovery) following calibration using commercially-available purified CPT-11, SN-38, and SN-38G. These experiments were performed by the lab of William C. Zamboni, PharmD, PhD (UNC Chapel Hill).

Tumor Studies in Mice

Efficacy experiments in mice were performed according to the Institutional Animal Care and Use guidelines approved by the Institutional Animal Care and Use Committee of the Albert Einstein College of Medicine, Bronx, New York. Healthy BALB/cJ female mice were divided into three groups of three mice each. Group 1 was untreated controls. Group 2 received CPT-11 treatment. Group 3 received CPT-11 treatment with pre-treatment with Inhibitor 1. Mice were initially xenografted with tumors of similar volume. Following treatment, tumors were excised. Efficacy of CPT-11 was quantified by measuring the final volume of the tumors.

3.4 Results

3.4.1 Rational Design of Novel Inhibitor Analogues

We have previously characterized a group of inhibitors discovered via high-throughput screening against a range of β-glucuronidase enzymes from *E. coli*, *Streptococcus agalactiae*, and *Clostridium perfringens* (*Ec*βG, *Sa*βG, and *Cp*βG, respectively; Chapter 2). Our next goal was to make chemical modifications to the most promising compounds in order to strengthen *in vivo* efficacy. Contrary to a typical drug development process, our system necessitates that compounds have a *low* bioavailability via

GI absorption. As opposed to a typical drug that requires robust absorption into the systemic circulation, these compounds are designed to stay in the digestive tract and thus, have a low bioavailability. Focusing on the modifications of the O-ethyl group on Inhibitor 1, we designed analogues in order to decrease their ability to be absorbed through cell membranes **(Figure 3.1)**. Compounds were designed with the assistance of Dr. Jian Jin (Center for Integrative Chemical Biology and Drug Discovery, UNC-Chapel Hill), and were synthesized by CDS. By increasing the charge of that side chain, we believed that we could decrease the gastrointestinal (GI) absorption of these compounds. Of the synthesized compounds, two (Inhibitor R1 and Inhibitor R3) were shown to maintain their ability to inhibit *Ec*βG.

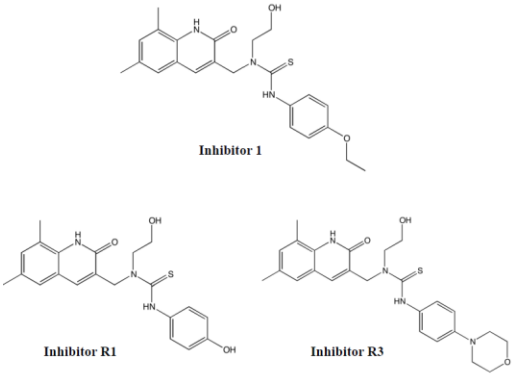

Figure 3.1. Chemical structures of novel analogues and the parent compound from which they were synthesized.

3.4.2 Inhibitory Characterization of Novel Analogues

We first characterized the novel analogues against *Ec*βG *in vitro* as well as against cultured *E. coli* cells using the substrate p-nitrophenyl glucuronide (PNPG) **(Table 3.1)**. Although the newly synthesized compounds maintained their ability to inhibit *in vitro* and in cell-based assays, there was a loss in potency. Compared to Inhibitor 1 (K_i = 160 nM), Inhibitor R1 (K_i = 1900 nM) had a10-fold decrease in potency, and Inhibitor R3 (K_i = 610 nM) exhibited a 4-fold decrease. In cell-based assays, Inhibitors R1 and R3 produced an approximately 3- and 2-fold decrease in their ability to inhibit β-glucuronidase activity (EC_{50} = 4.5 µM, EC_{50} = 3.1 µM, respectively). The drop in potency, however,

would not necessarily preclude the compounds from being used in *in vivo* experiments, but we hypothesized that it would result in reduced efficacy of amelioration of drug-induced toxicity.

	*Ec*βG *in vitro*		*E. coli* cell-based
	K_i (μM)	IC_{50} (μM)	EC_{50} (μM)
Inhibitor 1	0.16 ± 0.01	1.1 ± 0.09	1.3 ± 0.09
Inhibitor R1	1.9 ± 0.5	4.4 ± 0.4	4.5 ± 0.7
Inhibitor R3	0.61 ± 0.2	3.9 ± 0.1	3.1 ± 0.1

Table 3.1. Inhibition against *Ec*βG

3.4.3 Crystal Structure of *Ec*βG in Complex with Inhibitor R1

In order to better understand differences in their inhibitory potency, we determined the crystal structure of *Ec*βG in complex with Inhibitor R1 **(Table 3.2, Figure 3.2A)**. The protein crystallized as a dimer in the asymmetric unit with one Inhibitor R1 molecule located at the active site in each monomer. The unit cell is analogous to each of the previously determined inhibitor-bound structures of *Ec*βG. By focusing on the ligand binding pocket, adjacent to the active site, we were surprised to find a different orientation of the inhibitor and the active site residues relative to previously determined structures of Inhibitor R1 homologues, Inhibitor 2 and Inhibitor 3 (74). In previous structures, two tyrosines (Tyr-469 and Tyr-472) located adjacent to the active site would "flip in" upon inhibitor binding relative to the un-liganded structure. However, presented here is the first case where upon binding of an inhibitor, the tyrosines remain in their un-liganded conformation as evidenced by the apo *Ec*βG crystal structure **(Figure 3.2B)**. It is not clear whether this enzyme orientation explains the reduced potency of Inhibitor R1 relative to Inhibitor 1. More data with compounds found to bind in the same manner as Inhibitor R1 and to have similarly reduced potency would be required to confirm this hypothesis.

Data Collection	
Structure	*Ec*βG – InhR1
X-ray source	APS GM/CA-CAT 23-ID
Space group	C2
Unit cell: a, b, c (Å); α, β, γ (°)	169, 76, 126; 90, 125, 90
Resolution (Å) (highest shell)	42.01 - 2.39 (2.48 - 2.39)
I/σ	12.28 (2.24)
Completeness (%)	99 (91)
Redundancy	5.1 (5.1)
Refinement	
Resolution (Å)	42.01 - 2.39
No. of unique reflections	51255 (4627)
R_{work}	0.196 (0.268)
R_{free}	0.246 (0.328)
Molecules per asymmetric unit (AU)	2 *Ec*βG, 2 InhR1
No. of amino acids per AU	1201
No. of waters per AU	407
R.M.S. deviations	
Bond lengths (Å)	0.01
Bond angles (°)	1.32
Ramachandran (%)	
Favored	94
Allowed	5.4
Outliers	0.59

Table 3.2. Crystallographic statistics of *Ec*βG in complex with Inhibitor

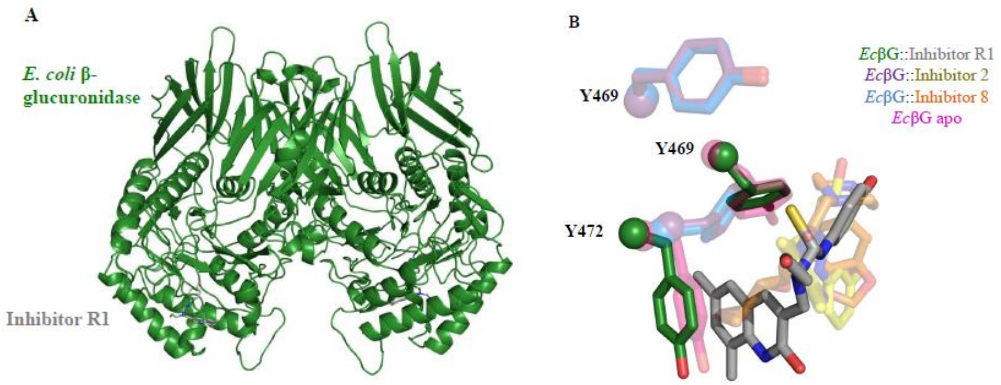

Figure 3.2. (A) Crystal structure of *Ec*βG dimer (green) in complex with Inhibitor R1 (gray), bound at the active site of each monomer. **(B)** Overlay of ligand binding tyrosines of Inhibitor R1-bound structure with previously determined structures: *Ec*βG (purple) bound to Inhibitor 2 (yellow) (PDB ID 3LPG), *Ec*βG (blue) bound to Inhibitor 8 (orange) (PDB ID 4JHZ), and un-liganded *Ec*βG (pink) (PDB ID 3K46).

3.4.4 Inhibitory Characterization of Novel Analogues against *Sa*βG and *Cp*βG

We next tested the inhibitor analogues against purified *Sa*βG and *Cp*βG. Although Inhibitor 1 maintained potency, the analogues displayed no apparent inhibition **(Table 3.3)**. In order to better understand this difference, we compared the Inhibitor R1-bound *Ec*βG structure to previously determined

un-liganded structures of *Sa*βG and *Cp*βG. Despite the high degree of structural similarity between species, focusing on the ligand-binding tyrosines, they are in the same "flipped-in" conformation for the un-liganded *Sa*βG and *Cp*βG structures as in the ligand-bound forms of *Ec*βG and in the opposite position as the un-liganded and the Inhibitor R1-bound *Ec*βG structure (**Figure 3.3A)**. The sequences directly adjacent to the tyorsines are highly conserved among *Ec*βG, *Sa*βG and *Cp*βG **(Figure 3.3B)**, so there is no clear explanation for these observed differences. Additional mutagenesis or crystallographic analysis is needed.

	K_i (μM)	
	*Sa*βG	*Cp*βG
Inhibitor 1	0.97 ± 0.1	1.4 ± 0.4
Inhibitor R1	NI	NI
Inhibitor R3	NI	NI

Table 3.3. Inhibition against *Sa*βG and *Cp*βG.

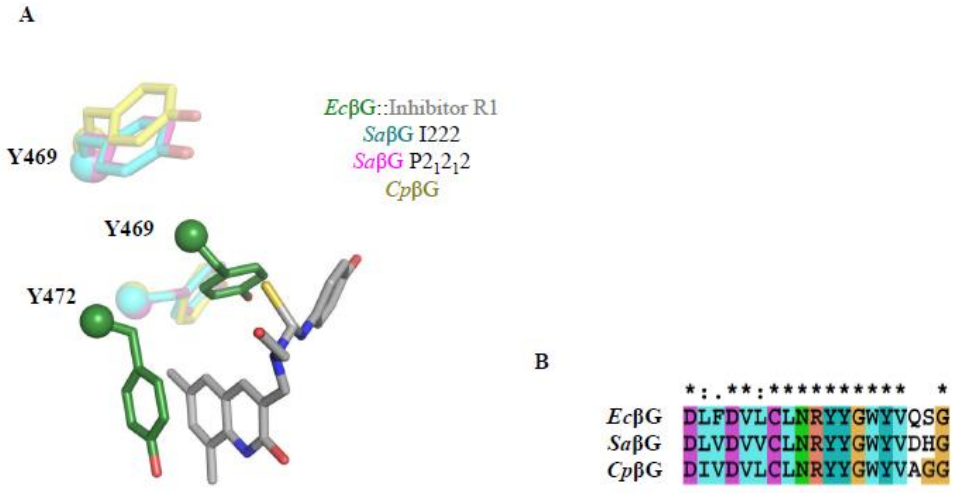

Figure 3.3. (A) Overlay of ligand binding tyrosines of *Ec*βG (green) in complex with Inhibitor R1 (gray) with previously determined structures: *Cp*βG (yellow) (PDB ID 4JKL), *Sa*βG (blue) in space group I222 (PDB ID 4JKK), and *Sa*βG (pink) in space group $P2_12_12$ (PDB ID 4JKM). **(B)** Sequence alignment of flexible, active site tyrosines and adjacent residues for *Ec*βG, *Sa*βG, and *Cp*βG. Based on residue numbering of Inhibitor R1-bound *Ec*βG, the alignment begins at Asp-458 and ends at Gly-476. Symbols represent the relative amount of sequence conservation

3.4.5 Inhibitor Plasma Pharmacokinetic Profile

We next investigated the plasma pharmacokinetics of each inhibitor to test our original conceit - that these analogues would display decreased systemic absorption than their parent compound. Mice were given a 3 mg/kg dose of Inhibitor 1, R1, or R3, either orally or intravenously (IV) **(Figure 3.4)**. There were 9 mice in each group, and each time point consists of samples from 3 mice such that the same groups of 3 mice were sampled for each 4th time point. In each case, both routes produced a peak half-life of less than 1 hour. Unsurprisingly, the IV route produced larger peaks. After IV administration, Inhibitor 1 reached its peak half-life at 0.25 hours, longer than Inhibitors R1 and R3, which reached their peak half-life at 0.08 hours **(Figure 3.4A)**. Inhibitor R1 had a lower peak concentration (1400 ng/mL) than either Inhibitor 1 (4800 ng/mL) or Inhibitor R3 (5500 ng/mL). The same trends between inhibitors were observed following oral administration **(Figure 3.4B)**. These data present Inhibitor R1 as an improved clinical candidate for the purpose of alleviating drug-induced toxicity mediated by bacterial β-glucuronidases.

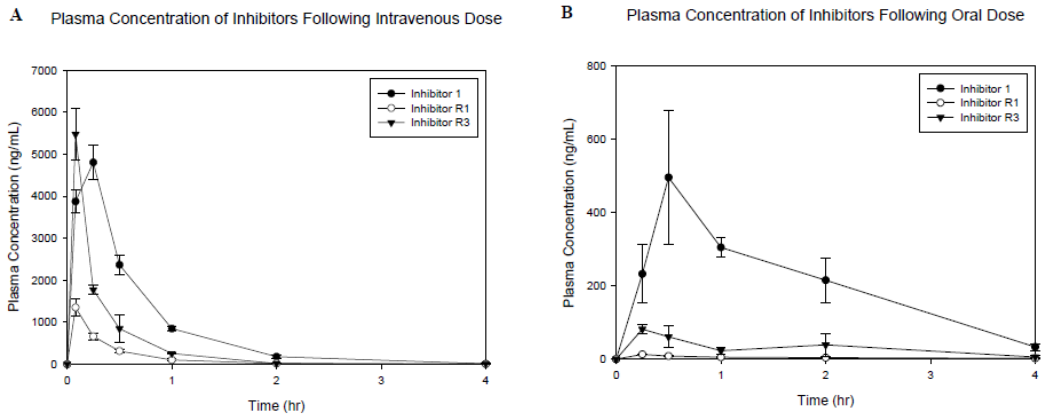

Figure 3.4. Mice (N = 9) were given either an intravenous **(A)** or oral **(B)** dose of the inhibitors. Concentrations of the compound were then measured in the blood at regular time intervals (N = 3).

3.4.6 Oral Bioavailability of Novel Analogues

We further tested our hypothesis by measuring the oral bioavailability (%F) of the inhibitors, the amount of the compound that reaches systemic circulation **(Table 3.4)**. Healthy Swiss Albino mice

received a 3 mg/kg dose of each inhibitor and plasma samples were drawn at regular time intervals. In support of our strategy, the bioavailability of the inhibitor analogues were decreased 6- and 3- fold from 21% for Inhibitor 1 to 3.5% and 6.3% for Inhibitors R1 and R3, respectively. These results, however, do not take into account first-pass metabolism of each of the dosed inhibitors, so we interrogated how degradation of these xenobiotic compounds in the liver contributed to decreased bioavailability. To do this, mice were pretreated with 1-aminobenzotriazole (ABT) at 50 mg/kg two hours prior to the same dose of inhibitor. ABT is a pan-inhibitor of cytochrome P450 enzymes, a main route of initial xenobiotic degradation. By eliminating cytochrome P450 activity, we see how first-pass metabolism affects compound levels in plasma. In that case, the bioavailability of Inhibitor 1 increased from 21% to 99%, indicating that the majority of Inhibitor 1 given to mice is subject to cytochrome P450 metabolism. The bioavailability of Inhibitor R3 similarly increased from 6.3% to 74%. Inhibitor R1, however, only produced a relatively minimal increase, from 3.5% to 12%, indicating that more of Inhibitor R1 is not subject to the same degree of metabolism by cytochrome P450 enzymes in mice as Inhibitors 1 or R3.

	Oral %F	Oral %F + ABT
Inhibitor 1	21	99
Inhibitor R1	3.5	12
Inhibitor R3	6.3	74

Table 3.4. Oral bioavailability (%F) of inhibitors in mice with and without the pan-cytochrome p450 inhibitor, ABT.

3.4.7 Comparison of the Alleviation of CPT-11 Diarrhea by Novel Analogues

Although our attempts were met with only partial success, we took this opportunity to understand how each of these elements factor into greater *in vivo* success. To test this, we performed an experiment where a group of mice were treated with CPT-11.Another group of mice would be given the same dose of CPT-11 and pretreated with either Inhibitor 1 or R1. In doing this, we saw that Inhibitor 1was more effective at alleviating the drug-induced diarrhea than Inhibitor R1 **(Figure 3.5)**. For example, on day 8

following CPT-11 treatment, 14% of mice had developed bloody diarrhea in the group pre-treated with Inhibitor R1, while in the same time frame, no mice had developed the same symptoms in the group pre-treated with Inhibitor 1.

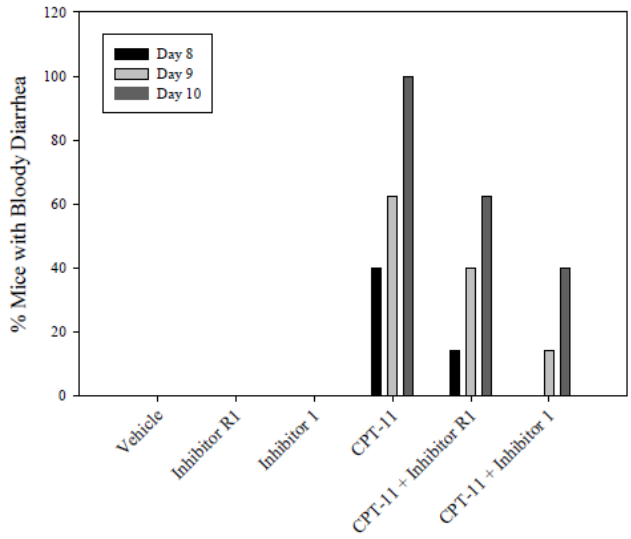

Figure 3.5. Alleviation of CPT-11-induced diarrhea in mice that were give a dose of CPT-11 either with or without pretreatment of either Inhibitor 1 or Inhibitor R1.

3.4.8 Effects of Pre-treatment with Inhibitor 1 on CPT-11 Plasma Pharmacokinetic Profile

Although we have shown that inhibition of bacterial β-glucuronidase is able to alleviate the dose-limiting diarrhea in mice, we have not shown that if, by doing so, we are impacting the efficacy of CPT-11 by altering its pharmacokinetics. The efficacy of some chemotherapeutics has been postulated to require enterohepatic recirculation of reactivated metabolites created by the GI β-glucuronidases (e.g., sorafenib), so it is important to understand if inhibition impacts plasma levels of CPT-11 and its metabolites SN-38 and SN-38G. Thus, we measured the plasma pharmacokinetic profile of CPT-11 in mice with and without pretreatment of Inhibitor 1. CPT-11 and Inhibitor 1 dosing were performed as described in previous toxicity studies (74). As shown in **Figure 3.6**, we observed no change in the pharmacokinetic profile of CPT-11. These data indicate that levels of CPT-11 and its metabolites in the plasma of mice are not impacted by inhibition of GI-associated bacterial β-glucuronidases in these animals.

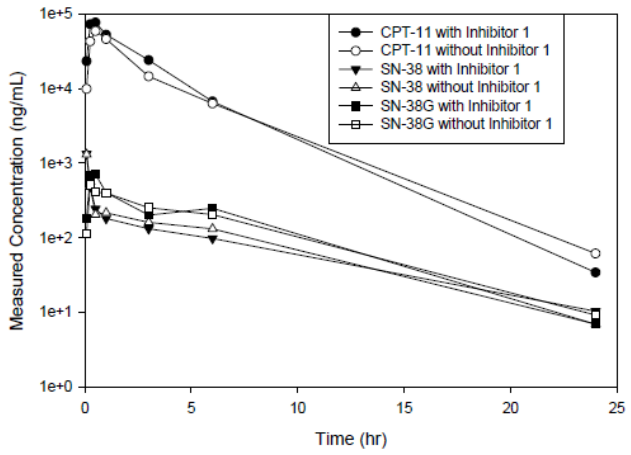

Figure 3.6. Effects on plasma pharmacokinetic profile of CPT-11 after pretreatment with Inhibitor 1

3.4.9 Effects of Pre-treatment with Inhibitor 1 on Anti-tumor Ability of CPT-11

By demonstrating that SN-38 plasma levels remain the same in the presence of the bacterial β-glucuronidase inhibitor, Inhibitor 1, it suggests that antitumor efficacy of CPT-11 would also remain intact. Thus, we tested how Inhibitor 1 would affect the anti-tumor activity of CPT-11 in preliminary studies with only a small number of mice, using doses of CPT-11 and Inhibitor 1 employed previously. Mice were transplanted with xenografted tumors grown from primary cells taken during surgery from a colon cancer patient at Einstein College of Medicine. Groups of these mice were then untreated (N = 4), treated with CPT-11 (N = 3), or pretreated with Inhibitor 1 prior to CPT-11 treatment (N = 3). We saw no change in the anti-tumor activity of CPT-11, as measured by reduction in tumor size, with or without pretreatment with Inhibitor 1 **(Figure 3.7)**. These results provide the first data to support the conclusion that the GI toxicity of CPT-11 can be reduced without impacting anticancer activity and indicate that with more work on dosing regimen, improved antitumor efficacy could also be achieved.

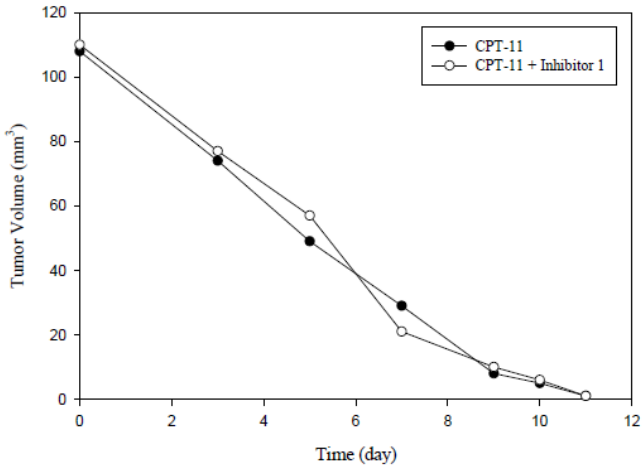

Figure 3.7. Effects on anti-tumor efficacy of CPT-11 after pretreatment with Inhibitor 1

3.5 Discussion

Previous work from this lab has led to the discovery of non-toxic small-molecule β-glucuronidase inhibitors selective for the bacterial enzyme over the mammalian orthologue or familial bacterial enzymes. These inhibitors were tested in order to develop a potential therapeutic for use in humans in order to alleviate GI toxicity as a side effect of the reactivation of conjugated drug metabolites by symbiotic GI-associated microbiota. The development of a lead candidate, however, requires more than potent *in vitro* inhibition. It must also demonstrate essential *in vivo* properties for use as a drug. For most drugs that require trafficking to sites throughout the body, one crucial property is bioavailability, the amount of the drug that reaches systemic circulation. For our purposes, however, the site of action for potential therapeutics is not reached via systemic circulation. Instead, we seek to develop a compound with a low bioavailability, such that the compound may possibly stay in the digestive tract where it impacts the β-glucuronidase activity of the microbiota population that naturally resides in the host intestine. Therefore, in this investigation, we sought to chemically modify a lead compound in order to decrease its bioavailability.

The O-ethyl side chain of the lead compound, termed Inhibitor 1, was modified to increase the overall charge in the hopes of decreasing GI absorption **(Figure 3.1)**. Two analogues that were produced, termed Inhibitors R1 and R3, maintained potent inhibition of *Ec*βG **(Table 3.1)**. We then measured the

bioavailability for each compound in mice. Indeed, both analogues produced a marked decrease in the amount of compound to reach systemic circulation compared to the parent compound **(Table 3.4)**. These results were magnified when, upon repeating the experiment but pretreating the mice with a pan-cytochrome P450 inhibitor (ABT), eliminating the variable of degradation in the liver that may lower the measured bioavailability, only Inhibitor R1 maintained a sufficiently low bioavailability. These data indicate that the modifications made to Inhibitor R1 altering its overall charge will lower bioavailability.

Before we accept that Inhibitor R1 experiences more residence time in the intestine where it could effectively inhibit bacterial β-glucuronidases, we must make the following assumptions. First, because we have not directly measured the levels of the inhibitors in the feces of treated mice, we cannot conclude that reductions in bioavailability correlate with increases in the GI lumen presence of these compounds. Second, we are assuming that the unmodified compounds are the only forms of these chemicals that are active on target GI bacterial enzymes. It is possible that metabolic drug products or microbial processing of these compounds will reduce drug-induced toxicity. A complete pharmacokinetic profile of each compound would be required to understand the roles played by each metabolite in diarrhea amelioration.

Unfortunately, the analogues proved ineffective at inhibiting purified β-glucuronidases from two GI-associated bacterial species, *Clostridium perfringens* and *Streptococcus agalactiae* **(Table 3.3)**. It is possible that only enzymes more closely related to *Ec*βG (e.g., from the same phylum) would still maintain inhibition by Inhibitor R1, while more distantly related enzymes (e.g., Firmicutes such as *Sa*βG and *Cp*βG) would not. Sequence alignment between these enzymes does not clarify the differences **(Figure 3.3B)**, but crystallographic analysis highlights ligand-binding tyrosines that are "flipped-in" in un-liganded *Sa*βG and *Cp*βG structures relative to the Inhibitor R1-bound structure of *Ec*βG **(Figure 3.3A)**. Interestingly, the tyrosines had previously only been observed to "flip-in" to accommodate binding based on structures of inhibitor-bound *Ec*βG relative to the un-liganded *Ec*βG structure. While the *Sa*βG and *Cp*βG structures present the enzymes in their un-liganded forms, these comparisons allow us to draw preliminary conclusions. For instance, contrary to *Ec*βG structures that show that these tyrosines are

dynamic upon ligand binding, it is possible that these tyrosines are rigid in the "flipped-in" position in *Sa*βG and *Cp*βG. For all of the previously studied inhibitors, this is not a problem because the tyorsines need to be "flipped-in" to allow for proper binding contacts. Inhibitor R1 is the first case of a ligand that necessitates the opposite position for these tyrosines, as seen in the wild-type *Ec*βG structure. Thus, if these tyrosines in *Sa*βG and *Cp*βG are not dynamic, but rigid instead, then Inhibitor R1 will not be an effective broad-spectrum inhibitor, as observed experimentally. This leads one to believe that Inhibitor 1, which is more effective *in vivo*, binds in a mode similar to other structurally similar compounds, Inhibitor 2 and Inhibitor 3 where the tyrosines are "flipped-in" (74). Further crystallographic analysis and testing with additional bacterial enzymes would be necessary to support or refute this hypothesis.

Since the three tested enzymes only represent a portion of the total β-glucuronidase activity in GI-associated microbiota, the lack of observed broad-spectrum inhibition does not necessarily preclude the analogues from *in vivo* success. Thus, we tested Inhibitor R1 *in vivo* to better understand whether broad-spectrum inhibitory efficacy or low bioavailability translates to the ability of the compound to alleviate CPT-11-induced diarrhea **(Figure 3.5)**. From these results in mice indicating that Inhibitor 1 is more effective at alleviating the dose-limiting toxic side effect of CPT-11, it appears the ability for a compound to potently inhibit a range of β-glucuronidase enzymes across bacterial species makes a compound a more effective therapeutic. A full pharmacokinetic profile of the inhibitors would be necessary to understand this possibility, with the goal of finding an effective broad-spectrum inhibitor that possesses low bioavailability. The success of Inhibitor R1 producing a lower bioavailability should direct us to develop more analogues that possess both of these characteristics.

Still, we moved forward with Inhibitor 1 as a lead candidate. Although it has proven effective at alleviating drug-induced toxicity, there are questions that remain to be answered regarding its effect on the anti-tumor ability of CPT-11. We first tested Inhibitor 1 in a model to measure effects on the plasma pharmacokinetic profile of CPT-11 **(Figure 3.6)**. Comparing groups of mice that received CPT-11 alone and mice that received CPT-11 but were pretreated with Inhibitor 1, there were no significant differences in the pharmacokinetics of CPT-11 in plasma, including SN-38 or SN-38G, suggesting that Inhibitor 1

should not affect the anti-tumor efficacy of CPT-11, and more broadly, that the efficacy of CPT-11 does not rely on the enterohepatic circulation of its active metabolite, SN-38. This is an important result because it has been hypothesized that, in addition to mediate toxicity, bacterial reactivation of SN-38 in the intestinal lumen is critical for the broad anti-cancer ability of CPT-11 via enterohepatic circulation. Therefore, if we can show that levels of SN-38, the active metabolite, in systemic circulation are not effected by β-glucuronidase inhibition, then it follows that the anti-cancer efficacy of CPT-11 should not be effect either.

More directly, we tested the system of inhibition in a model that could alter the efficacy of CPT-11 in reducing tumor size **(Figure 3.7)**. Groups of mice were implanted with foreign tumors and then received no treatment, CPT-11 only, or CPT-11 preceded by an oral dose of Inhibitor 1. Strikingly, upon pretreatment with Inhibitor 1, there were no changes in the ability of CPT-11 to shrink the tumor. These results are preliminary and thus, do not show a statistical significance, but qualitatively, the results are encouraging and warrant further experimentation.

Here, we have shown that we are able to chemically modify a putative β-glucuronidase inhibitor to profoundly change its *in vivo* properties. Unfortunately, these alterations, in this case, also produced negative results *in vitro*. Testing these conflicting results, the ability to alleviate drug-induced toxicity indicated that the capacity of the inhibitors to impact a range of enzymes from different bacterial species outweighs improved *in vivo* bioavailability. Taking the lead compound, Inhibitor 1, we further investigated its biological relationship to CPT-11. We demonstrated that, in mice, pretreatment with Inhibitor 1 does not impact that plasma pharmacokinetic profile of CPT-11. Strikingly, preliminary results indicate that Inhibitor 1 does not affect the ability of CPT-11 to shrink tumors in mice. These data will allow us to move forward with a focused plan to chemically modify lead compounds in order to produce a more robust *in vivo* result.

Chapter 4

Design of Novel Inhibitors with Increased Potency Using Structural and Chemical Biology

4.1 Summary

Drug-induced toxicity represents a serious, yet often underreported and difficult to treat, complication in chronic and acute therapeutics. For example, CPT-11, used for treatment of colorectal cancer, and NSAIDs, the most widely prescribed class of drugs in the world, are hindered by gastrointestinal complications, which may be fatal. The symbiotic GI microbiota, specifically a hydrolytic enzyme known as β-glucuronidase, have been implicated in mediating these toxicities through the reactivation of drug metabolites. Targeted bacterial β-glucuronidase inhibitors have been shown to alleviate these toxicities in mouse models. We synthesized analogues of the most potent compound with the goal of increasing potency by focusing on the solvent exposed side chain of the ligand based on crystallographic analysis. Kinetic analysis demonstrated a slight increase in potency in assays with three bacterial β-glucuronidases. One compound, however, exhibited a 10-fold increase in potency in IC_{50} assays against the enzyme from *Clostridium perfringens* perhaps due to a unique symmetry in the side chains, observed in crystal structures producing multiple conformations of bound inhibitor. This compound is the most potent β-glucuronidase inhibitor known to date.

4.2 Materials and Methods

Reagents

The assay substrate p-nitrophenyl β-D-glucuronide (PNPG) was purchased from Sigma-Aldrich (St. Louis, MO). Inhibitor 9 was synthesized by Asinex, Inc. (Winston-Salem, NC). Inhibitors were identified by high-throughput screening and secondary validation was performed in-house (37). β-glucuronidase (EC 3.2.1.31) from *E. coli*, *S. agalactiae*, and *C. perfringens* (*Ec*βG, *Sa*βG, and *Cp*βG, respectively) were expressed and purified as described previously (74). Purified β-glucuronidase was stored in 20 mM HEPES, 50 mM NaCl, pH 7.4 at ≈10 mg/mL at $^{-}80\ ^{o}C$.

Kinetic and Equilibrium Inhibition Assays.

Inhibition assays were conducted by measuring the β-glucuronidase-catalyzed conversion of PNPG to p-nitrophenol (PNP). The conversion of increasing concentrations of PNPG to PNP, in the presence of 10 nM enzyme, was measured in the presence of increasing concentrations of putative inhibitors; zero-substrate and zero-inhibitor controls were carried out at the same time. Reactions were conducted in 96-well, clear-bottom assay plates (Costar, Tewksbury, MA) at 37 ^{o}C in 50 µL of total volume. The reaction consisted of 10 µL of assay buffer (5% DMSO and 500 mM HEPES, pH 7.4), 5 µL of inhibitor solution (various concentrations), 5 µL of 100 nM enzyme, and 30 µL of substrate (various concentrations). Product formation was calculated by measuring the change in absorbance over time at 410 nm using a PHERAstar *Plus* microplate reader (BMG Labtech, Ortenberg, Germany). The acquired data were analyzed using Microsoft Excel and Sigmaplot 11.0. From these data, K_i values were calculated for each of the inhibitors.

A related assay was employed to calculate the IC_{50} values in the following manner. An analogous 50 µL reaction, consisting of enzyme (1 nM final), buffer, PNPG (1 mM final), and variable concentrations of the inhibitors, was incubated at 37 ^{o}C for 6 hours to allow the reaction to reach equilibrium and then quenched with 100 µL 0.2 M sodium carbonate. The percent inhibition for each concentration of inhibitor was calculated based on changes in absorbance and used to plot a dose-response curve. The IC_{50} value was calculated as the concentration of inhibitor that produced 50% *in vitro*

inhibition. The same assay was performed with purified bovine liver β-glucuronidase with PNPG as the substrate.

We also tested the ability of these compounds to inhibit β-glucuronidase activity in *E. coli* cells. We grew HB101 *E. coli* cells, transformed with the pET-28a vector containing the β-glucuronidase gene, to an OD_{600} of 0.6 in LB medium and used a small aliquot in an assay similar to the *in vitro* IC_{50} assay described above. The cells (39 µL) were incubated with 1 µL of variable concentrations of inhibitor and 10 µL of 1 mM PNPG at 37 ^{o}C for 6 hours. The reaction was quenched with 100 µL 0.2 M sodium carbonate. The amount of substrate turnover and therefore the amount of inhibition is calculated from the change in absorbance compared to zero-inhibitor controls. EC_{50} values were calculated as the amount of inhibitor necessary to produce 50% inhibition. The *in vitro* and cell-based assays employed here were similar to those reported previously (74).

Crystal Structure Determination

Crystals of *Ec*βG were obtained at 2 mg/mL protein with 30-fold molar excess Inhibitor 9-77 in 18% PEG-3350 (w/v), 250 mM magnesium acetate, and 0.02% sodium azide (w/v) at 16°C and with 30-fold molar excess Inhibitor 9-79 in 21% PEG-3350 (w/v), 300 mM magnesium acetate, and 0.02% sodium azide (w/v) at 16 °C and a 2:1 ratio of protein to crystallant. Crystals first appeared after 5 days, and were immediately cryo-protected with perfluoropolyether vacuum pump oil (Sigma-Aldrich, St. Louis, MO) and flash-cooled in liquid nitrogen. Diffraction data were collected on the 23-ID beam line at GM/CA-CAT (Advanced Photon Source, Argonne National Laboratory). Data in space group C2 were indexed and scaled using HKL2000 (93) to 2.79 Å resolution and 2.28 Å resolution for Inhibitors 9-77 and 9-79, respectively. The asymmetric units contained two monomers. The structures were determined with Phaser (94) using molecular replacement with the recent apo *Ec*βG structure (PDB ID 3K46) as a search model. The structures were refined using simulated annealing and torsion angle refinement with the maximum likelihood function target in CNS, and monitored using both the crystallographic R and cross-validating R-free statistics (95). The software suite PHENIX (96) was also employed for B-factor and TLS refinement. The models were manually adjusted using Coot (97) and $2F_o$-F_c and F_o-F_c electron

density maps. The ligand models and definition files were generated using PRODRG (98) and were placed into electron density in the active site of each monomer in the asymmetric unit.

Toxicity Studies in Mice

Animal experiments were performed according to the Institutional Animal Care and Use guidelines approved by the Institutional Animal Care and Use Committee of the Albert Einstein College of Medicine, Bronx, New York. CPT-11 (20 mg/mL) and Inhibitor 9 (100 μg/mL) were dissolved in 0.25% (w/v) carboxymethylcellulose sodium salt to make stock solutions. As a vehicle control, all animals received an equivalent volume (compared to experimental groups) of 0.25% (w/v) carboxymethylcellulose sodium salt solution. BALB/cJ female mice were divided into four groups: Group 1, vehicle controls received equivalent volume of 0.25% (w/v) carboxymethylcellulose sodium salt solution intraperitoneally (i.p.) and by oral gavage (~100 μL twice per day); Group 2, Inhibitor 9 gavaged (10 μg/day) twice per day (every 10 hours) starting on day $^{-}$1 with oral gavage of 0.25% (w/v) carboxymethylcellulose sodium salt solution, and i.p. once per day; Group 3, CPT-11 injected (50 mg/kg) i.p. once daily in the morning with oral gavage of 0.25% (w/v) carboxymethylcellulose sodium salt solution; Group 4, CPT-11 injected (50mg/kg) i.p. once daily in the morning, and Inhibitor 9 gavaged (10 μg/day) twice per day (every 10 hours). Total injected volume was identical for each animal. Mice were examined daily for signs of diarrhea (fecal staining of skin, lose watery stool) and bloody diarrhea (black sticky stool) using methods previously published (74, 99). Previous studies indicate that dosing at ~60-80 mg/kg/day of CPT-11 for 4 days allows for observation of delayed diarrhea around 15 days (100). A dosing scheme of 50 mg/kg/day, once daily for 9 days, was chosen with the intention of accelerating the onset of diarrhea while preventing death. As outlined previously, 50 mg/kg CPT-11 in mice is roughly equivalent to the 5 mg/kg typical human CPT- 11 dose based on differences in body surface area (63, 100).

4.3 Results

4.3.1 Design of Novel Inhibitor Analogues

The crystal structure of Inhibitor 9 in complex with a bacterial β-glucuronidase highlighted structural features of Inhibitor 9 critical for binding. This structure was determined and refined by Dr. Bret Wallace, a previous graduate student in the Redinbo Lab. Of particular interest is the terminal piperazine group that bound in the active site gorge, closest to the catalytic residues **(Figure 4.1A)**. To test the theory that the hydrogen-bond potential of the nitrogen is critical for inhibition, we synthesized an analogue of Inhibitor 9 with the piperazine nitrogen replaced by a carbon to create a piperidine group (Inhibitor 9-70; **Figure 4.1B)**. As expected, Inhibitor 9-70 displayed no inhibition against purified bacterial β-glucuronidases from *E. coli*, *Streptococcus agalactiae*, and *Clostridium perfringens* (*Ec*βG, *Sa*βG, and *Cp*βG, respectively) (data not shown). This is an important confirmation of the structure-activity relationship considered critical to Inhibitor 9 efficacy against these bacterial enzymes and validates the conclusion that the piperazine makes crucial contacts with the active site.

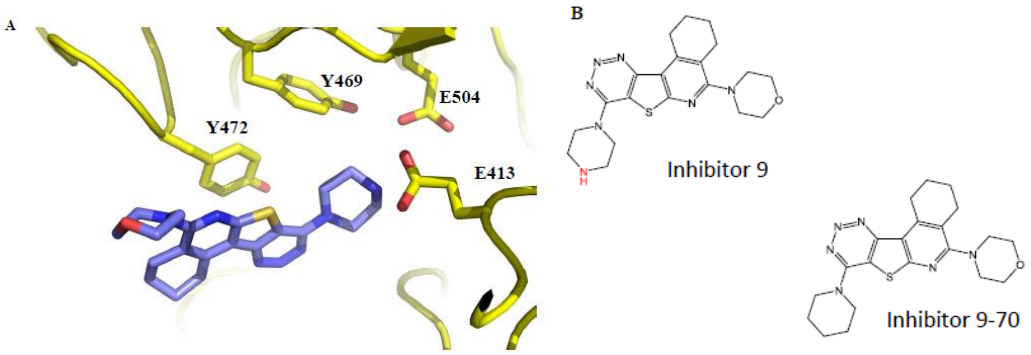

Figure 4.1. A) Previously determined x-ray crystal structure of Inhibitor 9 (purple) in complex with *Cp*βG (yellow) highlighting the ligand-binding pocket. The terminal piperazine group binds adjacent to active site tyrosines and catalytic glutamic acid residues. The solvent-exposed morpholine group does not make protein contacts, making it a target for modification. **B)** Chemical structure of Inhibitor 9 and a derivative designed to be inactive by substituting the nitrogen (red) in the piperazine side chain.

4.3.2 Characterization of Novel Inhibitor Analogues

Based on the Inhibitor 9-bound *Cp*βG structure **(Figure 4.1A)**, we targeted the solvent-exposed morpholine group for modification to minimize risk of reducing potency and, thus, synthesized a small

group of compounds with simple amine alterations that were amenable via the route of synthesis employed **(Figure 4.2)**. Compounds were designed with the assistance of Dr. Jian Jin (Center for Integrative Chemical Biology and Drug Discovery, UNC-Chapel Hill), and were synthesized by CDS. We characterized the newly synthesized analogues using the substrate p-nitrophenyl glucuronide (PNPG) by measuring absolute K_i values for each inhibitor against *Ec*βG, equilibrium inhibition against each *Ec*βG, *Sa*βG, and *Cp*βG, and equilibrium inhibition of β-glucuronidase activity in cultured *E. coli* cells **(Table 4.1)**. Inhibitor 9, the parent compound, displayed low-nanomolar (EC_{50} = 5 nM) inhibition in *E. coli* cells, and each analogue maintained the same level of inhibition. Inhibitor 9-81 and Inhibitor 9-79 showed the greatest improvement (EC_{50} = 1.6 nM and EC_{50} = 2.6 nM, respectively). We saw improved K_i values across the board with 2- to 10-fold increased potency relative to Inhibitor 9 (K_i = 54 nM). Inhibitor 9-81 (K_i = 4 nM) and Inhibitor 9-79 (K_i = 10 nM) were once again the most potent.

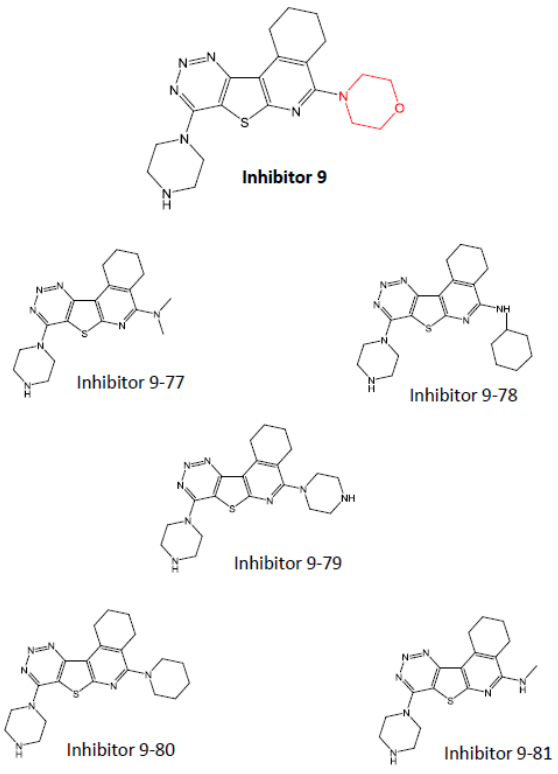

Figure 4.2. Chemical structure of Inhibitor 9 and analogues designed from it to increase potency by substituting the morpholine side chain (red).

	in-cell EC_{50} (nM)	*in vitro* K_i (nM)	*in vitro* IC_{50} (nM)		
	E. coli	*Ec*βG	*Ec*βG	*Sa*βG	*Cp*βG
Inhibitor 9	5.0 ± 2	54 ± 9	16 ± 8	9.7 ± 2	72 ± 20
Inhibitor 9-77	2.9 ± 1	17 ± 4	6.5 ± 3	3.9 ± 1	58 ± 20
Inhibitor 9-78	5.0 ± 1	17 ± 3	13 ± 4	6.0 ± 0.6	75 ± 20
Inhibitor 9-79	2.6 ± 1	10 ± 3	6.6 ± 2	5.6 ± 0.8	4.5 ± 1
Inhibitor 9-80	8.3 ± 4	23 ± 3	20 ± 10	11 ± 5	80 ± 20
Inhibitor 9-81	1.6 ± 0.7	4 ± 1	2.7 ± 2	6.2 ± 2	73 ± 20

Table 4.1. Cell-based and *in vitro* inhibition of β-glucuronidase activity using PNPG as the substrate. Data are represented as the average (N = 3) ± SEM.

Inhibitor analogues maintained potent IC_{50} values against *Ec*βG and *Sa*βG compared to Inhibitor 9. The largest improvement from these assays arose from IC_{50} values against *Cp*βG, of which Inhibitor 9 exhibited a 10-fold decrease in potency (IC_{50} = 72 nM) compared to *Ec*βG and *Sa*βG. This relative level of potency was maintained for each analogue, except for Inhibitor 9-79, which exhibited a 10-fold increase in potency (IC_{50} = 4.5 nM). Thus, Inhibitor 9-79 is attractive as a lead compound for this project because it shows nearly the highest potency observed to date in *E. coli* cell-based assays (EC_{50} = 2.6 nM) and the highest potency across the board with the purified β-glucuronidases in-hand, separating itself from its Inhibitor 9 analogue counterparts in *Cp*βG IC_{50} assays. *Cp*βG is by far the least catalytically efficient enzyme studied as yet **(see Table 2.2)**. As such, it's unclear that broad-spectrum potency for all bacterial β-glucuronidases will be essential for *in vivo* success, and future studies will be required to resolve that question.

4.3.3 Crystal Structures of Inhibitor Analogues in Complex with *EcβG*

To better understand the structural basis of analogue efficacy, we sought to resolve the crystal structure of these compounds in complex with the tested enzymes. We successfully determined two structures of *Ec*βG – complexes with Inhibitor 9-77 to 2.8 Å resolution and Inhibitor 9-79 to 2.3 Å resolution **(Figure 4.3, Table 4.2)**. Each crystalized in space group C2 with two monomers in the asymmetric unit. One molecule of Inhibitor 9-77 was observed in the ligand binding pocket of the enzyme, adjacent to the catalytic sugar-binding pocket and in a mode analogous to all previously-

determined crystal structures of bacterial β-glucuronidase inhibitor complexes, including Inhibitor 9. Overlaying the active site with previously determined structures, including the un-liganded structures from *Sa*βG and *Cp*βG, the side chains of the catalytic glutamic acid residues and the ligand-binding tyrosines remain in the same positions regardless of the presence of the inhibitor analogue **(Figure 4.4)**.

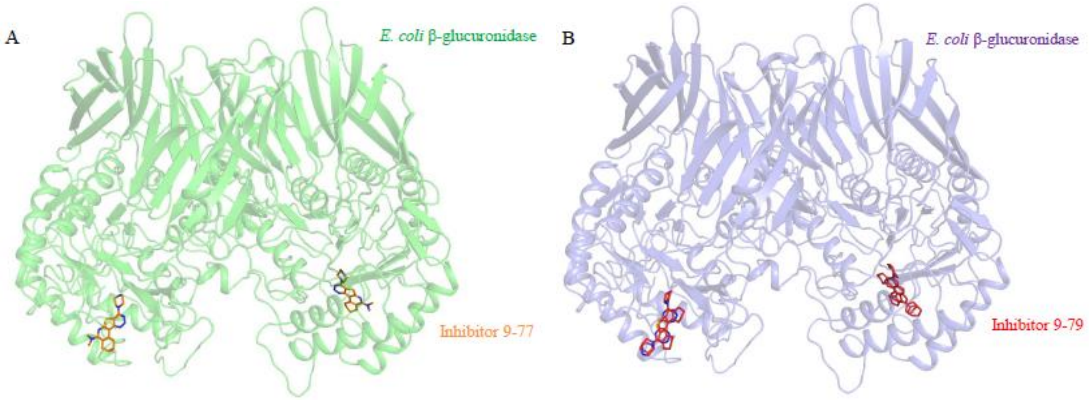

Figure 4.3. Full length structures of *Ec*βG in complex with Inhibitor 9-77 **(A)** and Inhibitor 9-79 **(B)**. Pictured is the asymmetric unit each containing two *Ec*βG monomers with one molecule of each inhibitor bound in the ligand-binding pocket of each monomer.

Data Collection		
Structure (RCSB ID)	*Ec*βG – Inhibitor 9-77	*Ec*βG – Inhibitor 9-79
X-ray source	APS GM/CA-CAT 23-ID	
Space group	C2	C2
Unit cell: a, b, c (Å); α, β, γ (°)	167, 77.7, 126; 90, 125, 90	167, 77.6, 126; 90, 125, 90
Resolution (Å) (highest shell)	48.1 - 2.79 (2.89 - 2.79)	48.1 - 2.28 (2.36 - 2.28)
I/σ	15.9 (2.67)	15.3 (2.52)
Completeness (%)	99.5 (94.9)	99.8 (98.7)
Redundancy	9.6 (8.7)	5.3 (5.2)
Refinement		
Resolution (Å)	48.13 - 2.79	48.1 - 2.28
No. of unique reflections	33078 (3282)	60382 (5944)
R_{work}	0.246 (0.343)	0.216 (0.283)
R_{free}	0.278 (0.368)	0.263 (0.316)
Molecules per asymmetric unit (AU)	2 *Ec*βG, 2 Inhibitor 9-77	2 *Ec*βG, 2 Inhibitor 9-79
No. of amino acids per AU	1197	1192
No. of waters per AU	114	440
R.M.S. deviations		
Bond lengths (Å)	0.016	0.012
Bond angles (°)	1.89	1.49
Ramachandran (%)		
Favored	94	96
Allowed	4.8	3.6
Outliers	1.2	0.42

Table 4.2. Crystallographic statistics of two structures of full-length *Ec*βG in complex with Inhibitor 9-77 and Inhibitor 9-79.

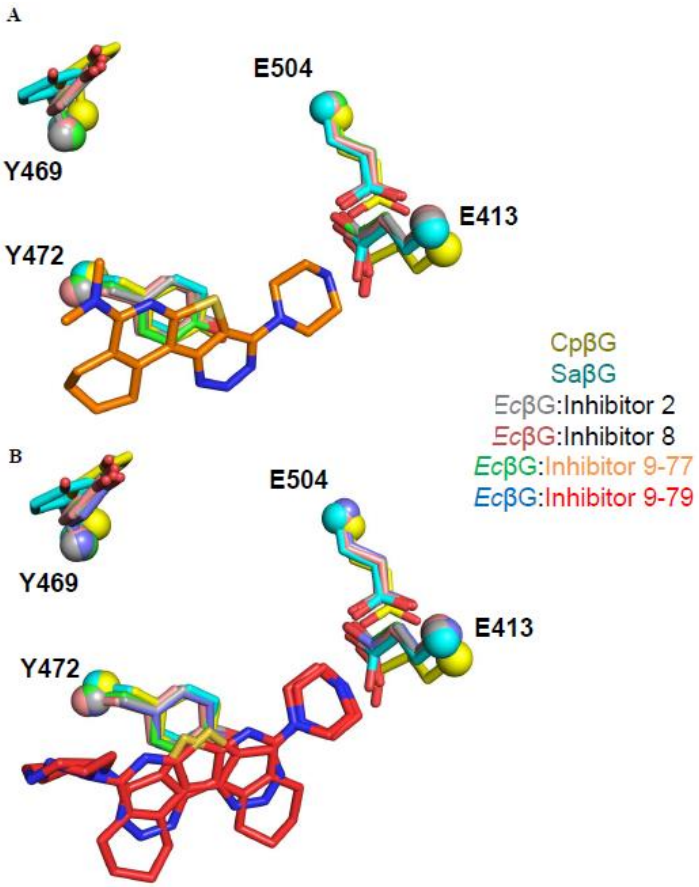

Figure 4.4. Overlay of ligand-binding pocket of *Ec*βG in complex with Inhibitor 9-77 **(A)** And Inhibitor 9-79 **(B)** with previously determined structures of bacterial β-glucuronidases highlighting catalytic residues and flexible tyrosines.

The structure of Inhibitor 9-79 in complex with *Ec*βG exhibited unique features relative to Inhibitor 9 and Inhibitor 9-77 complexes. The bound Inhibitor 9-79 produced incomplete electron density from the composite omit map outside of the core 4-ring scaffold **(Figure 4.5)**. As seen in Figure 4.6, there was unsettled density on the bottom left and right of the 4-ring scaffold that could not be explained through a single ligand conformation. Thus, we built alternative conformations into the electron density, and upon refinement, the occupancies of each conformation bound to chain B plateaued at 0.54 and 0.42 with average B-values of 86.73 and 87.72 $Å^2$, respectively. For comparison, the B-factors for Inhibitor 9 and Inhibitor 9-77 were 88.85 and 47.62 $Å^2$, respectively. Inhibitor 9-79 is unique from the other members of this series because the morpholine side chain was substituted for a piperazine group that effectively duplicates the moiety previously determined to be critical for inhibition. Indeed, the two

binding orientations of Inhibitor 9-79 place each piperazine in the active site and in contact with the catalytic glutamic acid residues **(Figure 4.4B)**. These two orientations, which are unique to Inhibitor 9-79, may explain the increase in potency in regards to *Cp*βG, although structure-function-mutagenesis experiments would be required to adequately answer that question.

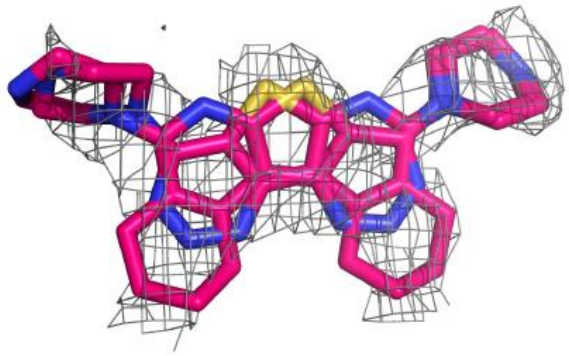

Figure 4.5. Orientation of Inhibitor 9-79 bound to *Ec*βG. Unresolved density in the composite omit map (grey) was accounted for through multiple conformations. Map is contoured at 1.0 σ.

4.3.4 Alleviation of CPT-11-Induced Diarrhea

We tested the lead compound, Inhibitor 9, in a model of drug-induced toxicity in mice. Specifically, groups of mice received either vehicle controls or a toxic dose of CPT-11 with or without pretreatment with Inhibitor 9 **(Figure 4.6)**. The dosing scheme has been established in previous investigations (74). The mice that were pretreated with Inhibitor 9 developed significantly less toxic diarrhea by day 10 compared to the CPT-11-only group, indicating that Inhibitor 9 is effective at alleviating CPT-11-induced toxicity in mice. These experiments are currently being repeated with Inhibitor 9-79 in order to relate increased broad spectrum potency to *in vivo* efficacy.

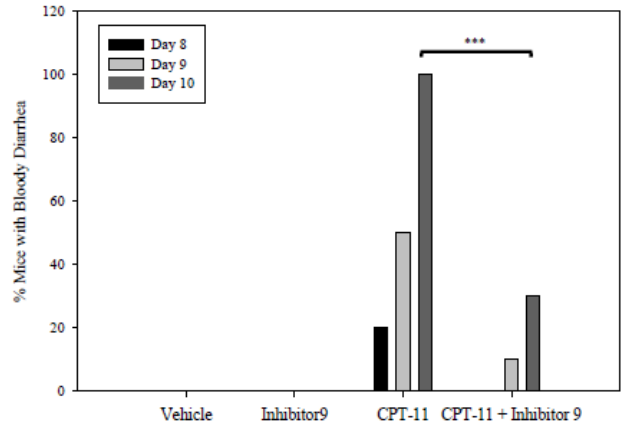

Figure 4.6. Mouse models of CPT-11-induced toxicity were employed to measure the therapeutic effects of Inhibitor 9. Groups of mice (N = 10) received either vehicle control or doses of CPT-11 with or without pretreatment with Inhibitor 9. Incidences of bloody diarrhea were observed and measure throughout the experiment. ***, $p < 0.001$

4.4 Discussion

We have described here the synthesis of inhibitor analogous, designed to increase potency for an already potent compound. Based on a previously determined structure of the parent compound in complex with *Cp*βG **(Figure 4.1)**, synthesis strategies revolved around the solvent-exposed morpholine group, altering the size and charge in an attempt to increase potency **(Figure 4.2)**. With the exception of Inhibitor 9-80, where a piperidine group was substituted, each analogue saw an increase in potency irrespective of the measurement. Inhibitor 9-79 stood out from its counterpart analogues due to a 10-fold increase in potency as measured by the IC_{50} value against *Cp*βG **(Table 4.1)**.

With the goal of better understanding the differences in the mechanism for inhibition, we successfully determined the x-ray crystal structures of *Ec*βG in complex with Inhibitors 9-77 and 9-79 **(Figure 4.3)**. Inhibitor 9-77 bound in the same general location, in the ligand-binding pocket, as all previously determined structures of *Ec*βG in complex with novel inhibitors. Importantly, Inhibitor 9-79 is unique in that it appears that the compound binds in two conformations, owing to its symmetric piperazine groups, the original of which had been previously shown to be critical for inhibition **(Figure 4.4)**.

Based on catalytic and inhibition data, it appears that there is an upper limit for inhibition for Inhibitor 9 and its analogues in the single-digit nanomolar range. Compared to *Ec*βG and *Sa*βG, *Cp*βG has a 100- and 10-fold decrease in catalytic efficiency, respectively (see Chapter 3). Something in this lack of activity relative to faster GI bacterial enzymes, perhaps as a result of the loop composition, means that this panel of inhibitors cannot reach that upper limit while binding to *Cp*βG, with the exception of Inhibitor 9-79. Thus, we hypothesize that the symmetry of Inhibitor 9-79 allows it to bind to *Cp*βG in a way to produce inhibition with greater efficiency than its counterparts, and this advantage is not realized with *Ec*βG and *Sa*βG because the upper limit of inhibition has already been reached.

These synthesized analogues, to date, have displayed the greatest potency of any studied β-glucuronidase inhibitors. As such, it will be necessary to continue the characterization of these compounds by analyzing their *in vivo* properties in preclinical models of drug-induced toxicity and efficacy. Studies of CPT-11-induced toxicity in mice show that Inhibitor 9 is among the most potent *in vivo* compound tested to-date **(Figure 4.6)**. However, Inhibitor 9-79 has yet to be tested in preclinical models including pharmacokinetic and bioavailability analysis. Nonetheless, we hypothesize that, owing to its unique symmetry where it appears to effectively inhibit in two conformations, Inhibitor-9-79 would be a more effective broad-spectrum inhibitor of bacterial β-glucuronidases *in vivo* than previously studied compounds. And because we have already shown that broad-spectrum inhibition is relatively critical to *in vivo* success (see Chapter 3), Inhibitor 9-79 should display potent *in vivo* efficacy that could translate to the clinical setting.

`

Chapter 5

Identification of Bacterial β-Glucuronidase Inhibitors via High-Throughput Screening of a Large Chemical Diversity Library

5.1 Summary

The toxicity of certain therapeutics has been linked to commensal bacterial β-glucuronidases, which cleave glucuronides from inactivated drug conjugates, allowing the reactivated drugs to then damage the gastrointestinal epithelium. This mechanism has been substantiated for the anticancer drug CPT-11, which produces large intestinal damage and dose-limiting diarrhea, and for non-steroidal anti-inflammatory drugs, which cause small intestinal ulcerations. In both cases, initial small molecule hit compounds served as selective but non-lethal bacterial β-glucuronidase inhibitors that alleviated gastrointestinal damage. Here, results from a high-throughput screen of a diverse 100,000 compound chemical library identify novel, chemically-distinct, potent and selective bacterial β-glucuronidase inhibitors. Of the 379 hit compounds, 298 were validated with IC_{50} values less than 30 μM, and 19 compounds displayed nanomolar inhibition. Five representative chemically-distinct compounds are shown to have no effect on the mammalian enzyme orthologue, to be non-lethal to bacterial or human cells, and effective against the enzyme target in cultured *E. coli* bacteria. These data broaden and deepen the understanding of the chemical and structural features capable of inhibiting this novel class of drug targets, the first to be identified in the mammalian microbiome.

5.2 Introduction

Disrupting the delicate relationship between host and commensal bacteria can be significantly detrimental, in a manner conceptually similar to auto-immune disorders (1–4, 11, 107–109). One enzyme in particular, β-glucuronidase, expressed by intestinal symbiotic bacteria, plays a critical role in the enterohepatic circulation of endogenous and xenobiotic compounds marked for gastrointestinal (GI) excretion by glucuronide conjugation (110–112). Furthermore, a range of drug toxicities mediated by symbiotic bacterial enzymes, including β-glucuronidase, pose serious health problems that are increasingly being appreciated (87, 90). In the GI tract, commensal β-glucuronidases remove the glucuronide sugar moiety, which is used by the bacteria as a carbon source, from circulated compounds and release the previously conjugated compound as an aglycone. In the case of bilirubin, for example, this facilitates reabsorption and recirculation of this vital endobiotic (113). However, this same pathway is now established in the development of dose-limiting diarrhea induced by the anti-cancer drug CPT-11 (irinotecan) (37–44).

We have previously shown that the GI toxicity of CPT-11 can be alleviated by selectively inhibiting the symbiotic bacterial β-glucuronidases (74, 106) by identifying novel β-glucuronidase inhibitors that disrupt enzyme activity in viable bacterial cells with no apparent toxic effects. We further showed, using x-ray crystallography and biochemical assays, that the novel inhibitors bound to a loop unique to the bacterial β-glucuronidases and critical for inhibition, and thus, exerted no effect on mammalian β-glucuronidases. Bacterial β-glucuronidases have been similarly implicated in NSAID-induced toxicity of the small intestine, which is an increasingly appreciated side effect of these widely used therapeutics (82). Certain NSAIDs have been known to undergo the same metabolism through glucuronide drug conjugates, and although the cause of the toxicity remained elusive, we demonstrated that bacterial β-glucuronidase inhibitors alleviate the toxicity associated with the NSAIDs diclofenac, indomethacin, and ketoprofen (85, 86).

Preliminary inhibitors were discovered using a relatively small, 10,000 compound chemical library screen (74, 106). Here, we describe the results from a 10-fold larger high-throughput screen

(HTS) of a 100,000 compound chemical diversity set performed at the UNC Center for Integrative Chemical Biology and Drug Discovery (CICBDD). We identified and validated 379 compounds that inhibited purified *E. coli* β-glucuronidase. Compounds representative of five structurally-diverse regions of chemical space were selected for *in vitro* and cell-based characterization.

5.3 Materials and Methods

HTS Reagents

The assay substrate 4-nitrophenyl β-D-glucuronide (PNPG) and bovine liver β-glucuronidase were purchased from Sigma-Aldrich (St. Louis, MO), and control initial Inhibitor 1 was purchased from Asinex, Inc. (Winston-Salem, NC). The expression and purification of *E. coli* β-glucuronidase (*Ec*βG), and the performance of the *in vitro* and cell-based assays, were conducted as described previously (74, 106).

LOPAC Compound Collection

The Library of Pharmacologically Active Compounds (LOPAC) was purchased from Sigma-Aldrich as 1 mM stocks in dimethyl sulfoxide (DMSO). The library was previously prepared as 1 μL samples in 384-well V-bottom polypropylene microplates (Greiner, Monroe, NC), sealed by an ALPS 3000 microplate heat sealer (Thermo Fisher Scientific, Hudson, NH) and stored at ⁻20°C. On the day of use, the compounds were thawed and diluted to 50 μM (5x final concentration) in reaction buffer (20 mM HEPES, 50 mM NaCl, pH 7.4) over two steps using a Thermo Scientific MultidropCombi Reagent Dispenser (Waltham, MA) and Multimek NSX-1536 assay workstation system fitted with a 384-well head (Nanoscreen, Charleston, SC). Finally, 1 μL of this stock was spotted into the wells of a 384-well black PerkinElmer Proxiplate (Waltham, MA) for assay use, as described below.

100K Diversity Screening Compound Collection

The 100K Diversity Collection of screening compounds was selected from the Enamine's HTS collection (enamine.net) based on diversity and drug-likeness criteria. Murcko scaffolds were used for the diversity selection (114). Essentially, a compound's Murcko scaffold includes contiguous ring systems

plus chains that link two or more rings. These scaffolds may be used to group compounds of a large collection into clusters, in each of which the compounds share the same Murcko scaffold. Here, for each Murcko cluster, at most 20 compounds were randomly selected in order to maximize the scaffold diversity of the 100K screening collection. Compounds were also filtered to eliminate reactive functional groups (REOS score > ⁻2) (115) and include compounds that obey the "rule of five" (116) with slight deviations to permit slightly larger and more lipophilic compounds. Based on the above selection process, a set of 100,000 compounds was purchased from Enamine Ltd (Kiev, Ukraine). The compound collection plates were prepared by resuspending the powder stock to 1 mM in DMSO in barcoded glass vials with sonication using a Covaris S2 (Covaris, Woburn, MA). Compounds were plated at 1 mM in 100% DMSO in 384-well V-bottom polypropylene microplates using a Tecan Genesis 200 (Münnedorf, Switzerland). A Multimek spotted 1 µL of the 1 mM compounds into 384-well V-bottom polypropylene microplates and plates were heat-sealed and stored at ⁻20 °C.

HTS Assay

The diversity library plates (1 mM in 100% DMSO and a volume of 1 µL as described above) were removed from ⁻20 ^{o}C freezers and allowed to reach room temperature. Each compound plate was diluted 1:20 in enzyme buffer (20 mM HEPES, 50 mM NaCl, pH 7.4) to a concentration of 50 µM (20 µl final volume) using a Multidrop dispenser. Control solutions were prepared in a separate 384-well plate consisting of the negative (20 mM HEPES, 50 mM NaCl, 5% DMSO, pH 7.4) and positive (20 mM HEPES, 50 mM NaCl, 5% DMSO, 0.2 M sodium carbonate, pH 7.4) control buffers, as well as a known β-glucuronidase inhibitor (Inhibitor 1) at two concentrations that produce approximately 50% and 100% inhibition diluted to 5% DMSO in enzyme buffer. The enzymatic reaction used in the HTS consisted of three addition steps. The first step consisted of the addition of 5 µl of diluted diversity library compounds and controls using the Multimek into an assay plate. This process was repeated for all of the assay plates. A Multidrop dispenser then added 10 µL of purified *E. coli* β-glucuronidase (20 mM HEPES, 50 mM NaCl, 3.75 nM *E. coli* β-glucuronidase, 0.15% BSA, pH 7.4). The plates were incubated for 10 minutes to allow for proper binding between the compound and the enzyme. A second Multidrop dispenser then

initiated the reaction with the addition 10 µL of substrate (20 mM HEPES, 50 mM NaCl, 0.4 mM PNPG, 0.1% BSA, pH 7.4). The plates were then immediately transferred to an EnVision Multilabel Reader (PerkinElmer) and the absorbance was measured at 405 nm at one minute intervals over the initial 10 minute period, corresponding to enzymatic production of 4-nitrophenol.

Compounds for dose–response curves were resuspended to a concentration of 10 mM in DMSO. The HTS hits were transferred into 384-well V-bottom polypropylene microplates and diluted as 3-fold dilutions over 10 points using the Tecan. Compound titration series of all hits for IC_{50} evaluation were then spotted at 1 µL by the Multimek into 384-well V-bottom microplates and diluted 20-fold in enzyme buffer using a Multidrop dispenser. The diluted titrations were then spotted at 1 µL into 384-well black Proxiplates in triplicate, and reagents were added to initiate the assay as described above. The final top concentration of dose–response curves was 10 µM compound (1% DMSO).

Data Analysis

Screening data were processed using ScreenAble software (Screenable Solutions, Chapel Hill, NC). The percent inhibition was determined on a plate-to-plate basis by comparing the rate of product formation for the compound versus the negative controls.

During assay development and validation, the Z' factor was calculated for each assay plate to assess the quality and robustness of the HTS. The Z' factor was determined using the following formula:

$$Z' = 1 - \left(\frac{3\sigma_{max} + 3\sigma_{min}}{|\mu_{max} - \mu_{min}|}\right)$$

where σ_{max} and σ_{min} are standard deviations (SDs) in respective plate maximum and minimum signal controls, and μ_{max} and μ_{min} are the plate-averages of the respective controls, as defined above.

During HTS, trimmed Z factors were calculated using the same controls and formula but using a MIDMEAN calculation (R v2.1.5) to determine control well averages.

Compound IC_{50} values were calculated by first converting the rate of product formation to percent inhibition with respect to on-plate controls and then fitting the percent inhibition values to curve

equations using ScreenAble. The IC_{50} values of the representative selection hits and Kinase Focus Set hits were calculated using ScreenAble with a 3- or 4-parameter curve fit.

Hit Analysis

379 hit compounds from the 100K Diversity Collection were grouped into homogeneous clusters, in which the similarity between any two compounds was at least 65% according to the Tanimoto metrics with ECFP4 fingerprints (Pipeline Pilot, ver 7.5; Accelrys Software, Inc.; 2009). The clustering procedure revealed 37 clusters (of more than 3 compounds) and 85 individual compounds. Only compounds with validated IC_{50} values less than 2 µM were considered for further evaluation. Compounds from the largest clusters, as well as compounds from individual or 2-hit clusters, were selected to provide a diverse group of compounds in order to build more diverse structure-activity relationships (SAR).

***In vitro* Assays**

The β-glucuronidases from *Streptococcus agalactiae* (*Sa*βG) and *Clostridium perfringens* (*Cp*βG) were expressed and purified as described (74, 106). Inhibition assays using these enzymes, in addition to *Ec*βG, were conducted by measuring the β-glucuronidase-catalyzed conversion of PNPG to 4-nitrophenol. Reactions were conducted in 96-well, clear-bottom assay plates (Costar, Tewksbury, MA) at 37 ^{o}C in 50 µL of total volume. The reaction consisted of 10 µL of assay buffer (100 mM HEPES, 250 mM NaCl, pH 7.4), 5 µL of inhibitor (various concentrations), 5 µL of 10 nM enzyme, and 30 µL of substrate (200 µM final). The reaction was incubated at 37 ^{o}C for 6 hours to allow the reaction to reach equilibrium and then quenched with 100 µL 0.2 M sodium carbonate. The product formation was measured using a PHERAstar *Plus* microplate reader (BMG Labtech, Ortenberg, Germany). The acquired data were analyzed using Microsoft Excel and Sigmaplot 11.0. The percent inhibition for each concentration was calculated based on changes in absorbance versus zero-inhibitor controls and used to plot a dose-response curve. The IC_{50} value was calculated as the concentration that produced 50% *in vitro* inhibition. The same assay was performed with purified bovine liver β-glucuronidase with PNPG as the substrate.

We also tested the ability of these compounds to inhibit β-glucuronidase activity in *E. coli* cells. We grew HB101 *E. coli* cells, transformed with the pET-28a vector containing the β-glucuronidase gene,

to an OD_{600} of 0.6 in LB medium and used a small aliquot in an assay similar to the *in vitro* IC_{50} assay described above. The cells (39 µL) were incubated with 1 µL of variable concentrations of inhibitor and 10 µL of 1 mM PNPG at 37 ^{o}C for 6 hours. The reaction was quenched with 100 µL 0.2 M sodium carbonate. The amount of substrate turnover and therefore the amount of inhibition is calculated from the change in absorbance compared to zero-inhibitor controls. EC_{50} values were calculated as the amount of compound necessary to produce 50% inhibition.

Toxicity of Inhibitors Toward Cultured Cells

The toxicity of inhibitors to bacterial cells was examined by incubating HB101 *E. coli* cells, transformed with the pET-28a vector containing the β-glucuronidase gene, grown to an OD_{600} of 0.6 in LB medium with each compound, as well as DMSO and ampicillin as controls, for 6 hours. Cell survivability was measured by plating a 10^{-5} dilution of the cells on LB media enriched with kanamycin. After overnight incubation, colonies were counted to quantify cell viability.

5.4 Results

5.4.1 HTS Assay Conditions

We have previously described several assays with purified *E. coli* β-glucuronidase (*Ec*βG) to assess the potential inhibitory capacity of small molecule compounds (74). For the high-throughput screen (HTS), 4-nitrophenyl β-D-glucuronide (PNPG) was used as the assay substrate; the products of its hydrolysis by β-glucuronidase are the glucuronic acid sugar and 4-nitrophenol, which readily absorbs at 405 nm **(Figure 5.1A)**. Because some of the compounds in the diversity library also absorb at this wavelength, we measured the initial linear rate of change in absorbance in the HTS reaction. Therefore, a significantly decreased rate of product formation relative to negative controls indicated a positive hit, and the change in the rate of product formation, as a percent of the negative controls, was used to quantify the amount of inhibition.

Purified *Ec*βG was validated for its use in this HTS by maintaining activity at room temperature for 6 hours **(Figure 5.1B)**. The enzyme's tolerance to DMSO, in which the diversity library compounds

are dissolved, was also tested. Past experiments have indicated that DMSO will denature bacterial β-glucuronidase (117); indeed, we found a significant decrease in activity after a 15 minute incubation in 1% DMSO. However, this effect can be prevented with the addition of bovine serum albumin (BSA) **(Figure 5.1C)**. *Ec*βG maintains its activity in up to 5% DMSO in the presence of 0.1% BSA **(Figure 5.1D)**. As such, we added BSA to the enzyme and substrate stocks during the screen (to a 0.1% BSA final concentration) to preserve consistent enzyme activity.

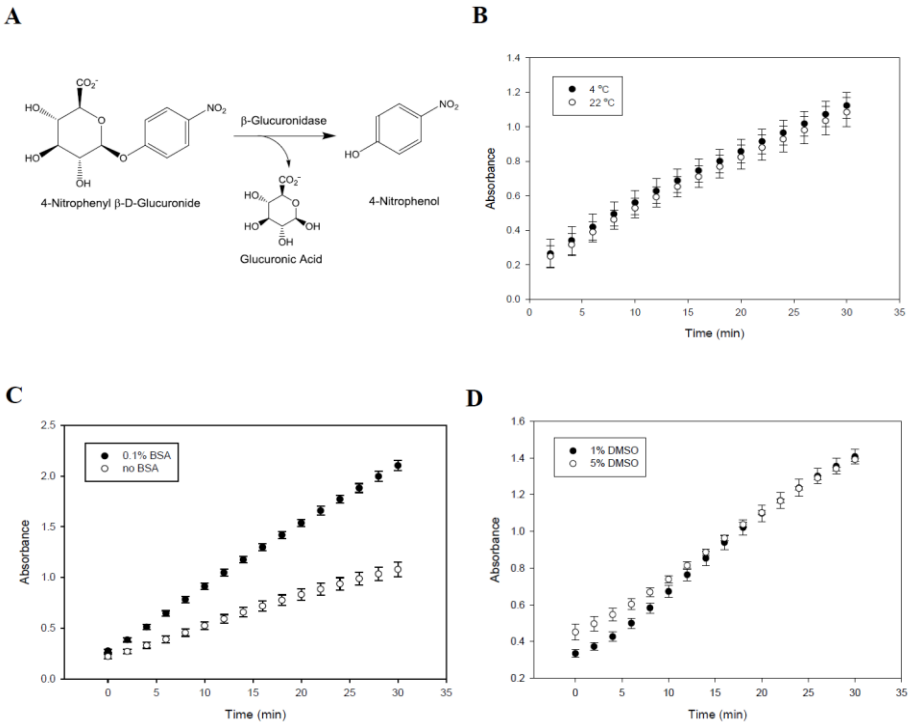

Figure 5.1. (A) Reaction utilized for HTS assay. **(B)** Temperature effects on *Ec*βG in the HTS assay. Data are presented as ± SD. **(C)** Addition of BSA to the HTS assay improves *Ec*βG activity. Data are presented as ± SD. **(D)** DMSO tolerance of *Ec*βG in the HTS assay. Data are presented as ± SD.

The K_M of PNPG was determined experimentally to be 0.16 mM (data not shown). Therefore, we titrated the enzyme to the K_M concentration, and chose the initial 10 minute period for data collection because it demonstrated a linear and robust rate of 4-nitrophenol production. Finally, we found that the reaction could be quenched with the addition of sodium carbonate. Ultimately, the concentrations for the HTS reaction were 1.5 nM *Ec*βG, 0.1% BSA, and 0.16 mM PNPG; each component was diluted in

enzyme buffer (20 mM HEPES, 50 mM NaCl, pH 7.4). The reaction was validated in 384-well microplate format, with a final reaction volume of 25 µL.

5.4.2 HTS Assay

The HTS reaction was initiated by the addition of substrate to solutions containing buffer, compounds and enzyme, and the increase in absorbance at 405 nm was measured over the initial 10 minutes **(Figure 5.2A)**. Negative controls consisted of DMSO in the initial buffer in place of the compounds. The reaction was quenched for the positive control wells with the addition of 3.4 M sodium carbonate to the initial buffer addition. Each plate also consisted of "standard" control reactions using one previously discovered putative inhibitor, Inhibitor 1, at two concentrations that would produce 100% and approximately 50% inhibition in order to ensure operational consistency during the screen. The diversity library was screened at a final concentration of 10 µM, corresponding to a final DMSO concentration of 1%. The HTS reaction was initially tested for day-to-day operational consistency and maintained Z-factors around 0.8 (data not shown). Initial compounds from the Library of Pharmacologically Active Compounds (LOPAC) screened in duplicate displayed very good reproducibility with a low false-positive rate **(Figure 5.2B)**.

During the screen, each plate maintained trimmed Z factors greater than 0.8, with only a few exceptions (**Figure 5.2C**). The screen produced 405 hits with greater than 45% inhibition **(Figure 5.2D)**. This list was narrowed to 379 compounds using drug-likeness filtering. All 379 hits were examined in full dose-response curves using the HTS assay. Of those hits, 298 compounds were validated with IC_{50} values less than 30 µM, and 19 compounds displayed nanomolar inhibition. From these data, we selected a group of potent (IC_{50} < 1.5 µM), chemically distinct compounds for further evaluation.

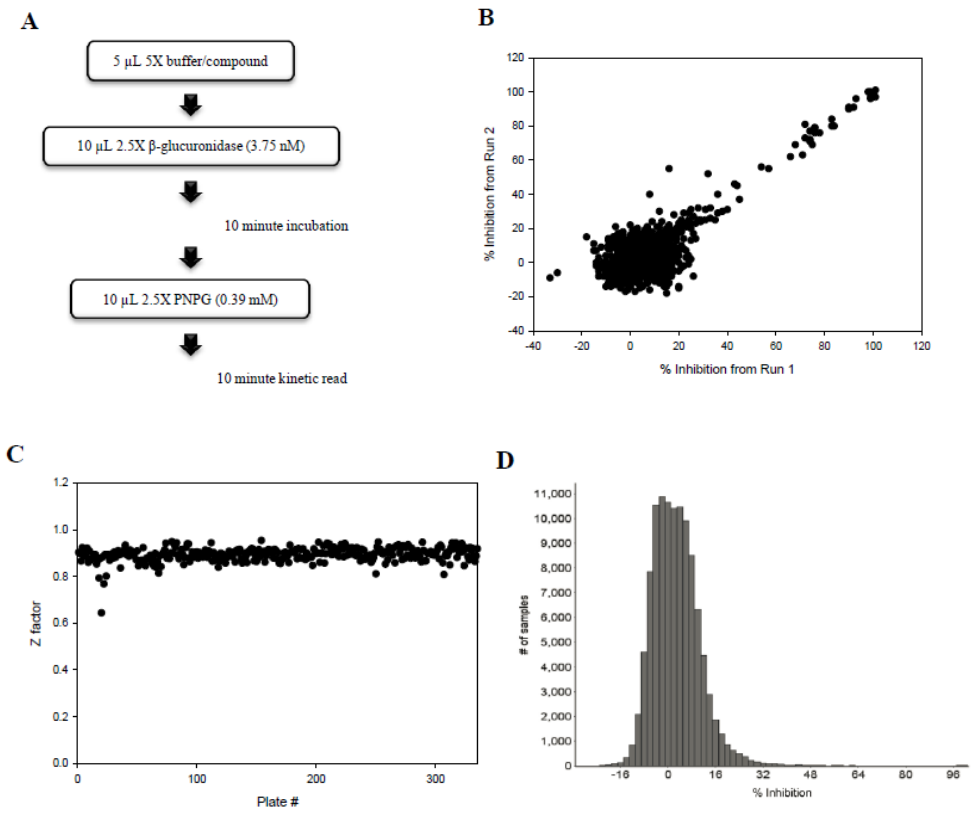

Figure 5.2. (A) HTS assay procedure. **(B)** Operational consistency of the HTS assay using preliminary LOPAC library. Inhibition values from duplicate runs are compared on the x and y axes. **(C)** Z-factors for each HTS plate. **(D)** For the complete 100,000 diversity library, the number of compounds (samples) observed for bins of percent inhibition; arrow indicates where the small number of effective hits was found.

5.4.3 Representative Compound Characterization

From the 298 validated hits with IC_{50} values less than 30 µM, we established 37 chemically-related clusters that contain 3 or more compounds and left 85 individual compounds. At this point, chemicals representative of five structurally-diverse regions of chemical space were selected for complete *in vitro* and cell-based characterization **(Figure 5.3)**. The five representative compounds, termed Inhibitors C, M, N, O and P, range from 297 to 420 Da in size, and contain from one (Inhibitor C) to four (Inhibitor O) conjugated rings with intervening polar linkages. Furthermore, they are representative of a range of chemical clustering results from the full HTS screen, from singletons (Inhibitor C), to small 2-compound clusters (Inhibitors M, O, and P), and up to a larger 16-compound cluster (Inhibitor N). For further characterization, each compound was first confirmed to be selective for inhibiting bacterial β-

glucuronidase versus bovine liver β-glucuronidase, a representative mammalian enzyme orthologue, at up to 370 µM inhibitor concentrations **(Figure 5.4A)**. Compounds were also found to be non-toxic to cultured mammalian HEK293T cells at 100 µM concentrations for 24 hours (data not shown), or to cultured *E. coli* cells at the same concentrations **(Figure 5.4B)**. Thus, these representative hits are selectively capable of inhibiting bacterial β-glucuronidases, and appear non-toxic to either bacterial or mammalian cells.

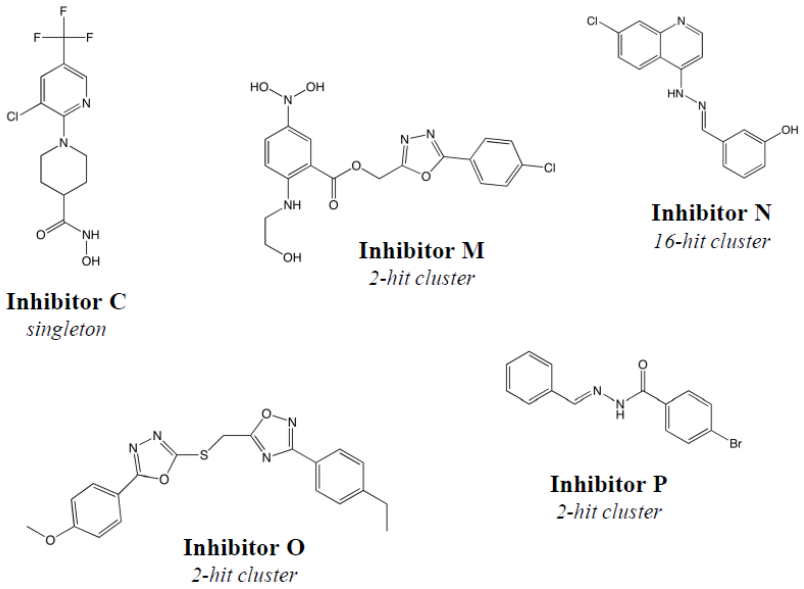

Figure 5.3. Chemical structures of five hits pursued for further analysis, along with the size of the clusters of associated hits from the full HTS.

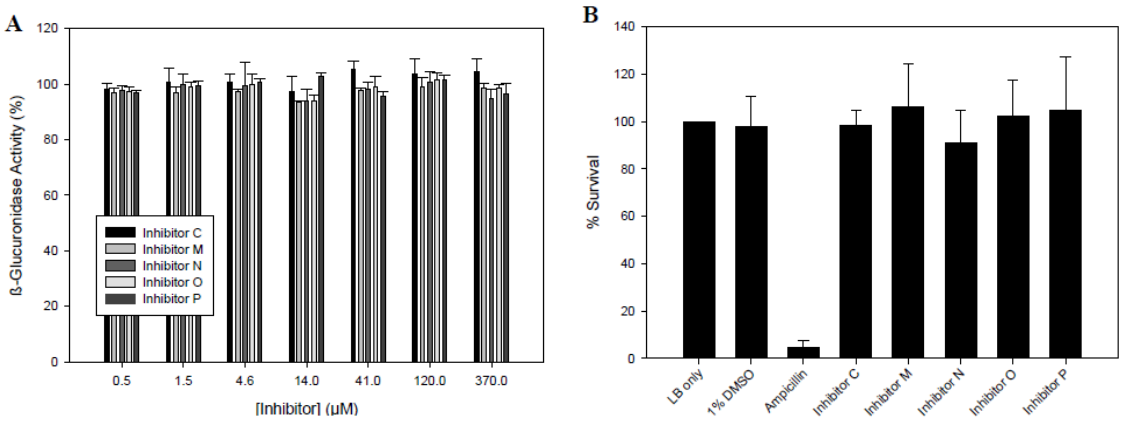

Figure 5.4. (A) Inhibition properties of hits against a representative mammalian β-glucuronidase, from bovine liver. **(B)** Hits do not kill cultured *E. coli* cells at 100 μM concentrations; ampicillin at 10 nM is used as a positive control, and the LB-only group is used to calculate the percent survival. Data are presented as ± SEM.

The five representative novel inhibitors were examined for their ability to inhibit purified bacterial β-glucuronidases *in vitro*, as well as for their efficacy against the enzyme target in cultured *E. coli* cells. Compounds were measured for their ability to inhibit *Ec*βG *in vitro*. Measured K_i values against *Ec*βG were comparable, ranging from 220 to 570 nM for Inhibitor P and Inhibitor N, respectively. β-glucuronidases from the GI-associated commensals *Clostridium perfringens* (*Cp*βG) and *Streptococcus agalactiae* (*Sa*βG) were purified, and IC_{50} values were measured for each compound against those enzymes in addition to *Ec*βG. Each proved to be inhibitors of *Ec*βG, with IC_{50} values ranging from 130 nM (Inhibitor O) to 2.2 μM (Inhibitor N), but IC_{50} values varied with the other purified enzymes **(Table 5.1)**. No inhibition was observed for Inhibitor N against *Cp*βG and *Sa*βG, and Inhibitors C and M were between 3- and 30-fold less active against *Cp*βG and *Sa*βG relative to *Ec*βG. Furthermore, Inhibitors M and P were 10- and 30-fold more potent, respectively, against *Sa*βG compared to *Cp*βG, while Inhibitor O was 5-fold more potent for the *Cp*βG compared to *Sa*βG. Only Inhibitor O maintained sub-micromolar inhibition against all three β-glucuronidase orthologues. Finally, each compound was validated in an *E. coli* cell-based assay and proved to be effective inhibitors with EC_{50} values ranging from 12 nM (Inhibitor C) to 1.4 μM (Inhibitor M). Inhibitor O was the second most potent compound at 130 nM. Thus, several

novel non-lethal inhibitors selective for bacterial β-glucuronidases were validated to be potent and effective in living bacteria against this drug target in the mammalian microbiome.

	in vitro K_i (nM)	in-cell EC_{50} (nM)	*in vitro* IC_{50} (nM)		
	*Ec*βG	*E. coli*	*Ec*βG	*Sa*βG	*Cp*βG
Inhibitor C	360 ± 50	12 ± 3	410 ± 50	8000 ± 900	7400 ± 4000
Inhibitor M	240 ± 70	1400 ± 200	830 ± 50	2300 ± 1000	28000 ± 9000
Inhibitor N	570 ± 90	600 ± 200	1100 ± 500	NI	NI
Inhibitor O	440 ± 60	130 ± 20	130 ± 8	670 ± 20	140 ± 40
Inhibitor P	220 ± 40	320 ± 70	720 ± 90	450 ± 50	14000 ± 4000

Table 5.1. Cell-based and *in vitro* inhibition of β-glucuronidase activity.

5.5 Discussion

The link between β-glucuronidase expressed by symbiotic GI-associated microbiota and dose-limiting toxicity caused by CPT-11 and NSAID treatments has been previously established (62, 74, 82, 85–87, 90, 106, 118). Indeed, using novel inhibitors, we have recently demonstrated that selective inhibition of bacterial β-glucuronidase in mice will alleviate the toxic diarrhea caused by CPT-11 treatment, as well as small intestinal ulcerations as a side effect of treatment with a variety of NSAIDs (74, 85, 86, 106). In this report, we screened a library of small molecule compounds with the goal of understanding the chemical and structural bases for bacterial β-glucuronidase inhibition. Five representative chemically-diverse compounds were validated, chosen for further evaluation, and were found to have the characteristics we consider important for *in vivo* use: potency both *in vitro* and in cells, selectivity for the bacterial enzymes and not the mammalian orthologue, and non-lethality to bacterial and mammalian cells.

Because we have utilized two newly purified GI-associated bacterial β-glucuronidases, we provide novel information on the structural basis for inhibitor activity across distinct microbial enzymes, as discussed below. The GI tract is composed of the Proteobacteria (e.g., *E. coli*), the Firmicutes (e.g., *S. agalactiae*, *C. perfringens*) and the Bacteroidetes (e.g., *Bacteroides fragilis*) phyla of bacteria. In this work, we examine representatives of the Proteobacteria and the Firmicute β-glucuronidases and show that

there is dissimilarity to the inhibition profiles observed. For example, Inhibitor N shows no impact on the Firmicute proteins but is effective against the representative Proteobacteria enzyme from *E. coli*. Although the enzymes studied in this report show a high degree of structural similarity, there are key deviations in two loop regions adjacent to the ligand binding site. In general, clearly, more work is required to examine a larger number of the Proteobacteria and Firmicute enzymes, as well as the characterization of Bacteroidetes proteins expected to perform this function.

Nevertheless, the data presented here are useful even at this early stage of understanding the enzyme orthologues present in the GI microbiota. *Sa*βG that was examined for inhibition by the five representative compounds shares 41% identity to *Ec*βG. By alignment, it contains an asparagine residue at the position equivalent to G364 and M365 in *Ec*βG and *Cp*βG, respectively, and a methionine corresponding to F450 and M448, respectively, in the other two proteins. Thus, *Sa*βG would appear to be intermediate between *Ec*βG and *Cp*βG with respect to these two positions suggested to be important in inhibitor efficacy. For example, the polarity of the *Sa*βG N residue equivalent to M365 in *Cp*βG perhaps allows the Inhibitor M compound improved ability to bind to *Sa*βG, as this inhibitor is 10-fold more effective toward this target orthologue **(Table 5.1)**.

Taken together, these data provide a framework for predicting potential efficacy against β-glucuronidases from other commensal bacterial strains across the GI-associated microbiota in order to successfully and completely alleviate toxic, drug-induced GI side effects. Such information will be important not only in designing more effective therapeutics, but also in understanding the potential impact of such targeted reagents on drug toxicity and efficacy, as well as on endobiotic and xenobiotic homeostasis involving glucuronide-dependent enterohepatic circulation.

Chapter 6

Conclusions and Further Work

6.1 Chemical Modification of Lead Compounds

Crystallographic analysis of bacterial β-glucuronidases in complex with our novel inhibitors has demonstrated that each molecule binds in essentially the same location at the mouth of the active site. Based on the structure of *E. coli* β-glucuronidase (*Ec*βG) in complex with glucaro-δ-lactam (GDL), an analogue of glucuronic acid, we believe that the glucuronide moiety generally binds further into the active site gorge, adjacent to the catalytic glutamic acid residues **(Figure 6.1)**. Therefore, one can envision new compounds based on the existing scaffolds of potent compounds with the addition of a GDL-type moiety to allow for more extensive binding in the β-glucuronidase active site. Previously determined structures facilitate the addition of the glucuronide group to the proper location on the inhibitor. Figure 6.1 outlines the potential for such a combined inhibitor. It overlays the Inhibitor 9-bound structure of *C. perfringens* β-glucuronidase (*Cp*βG) with the *Ec*βG structure in complex with GDL, highlighting that the ligands generally populate two separate areas in the active site. Although as it appears the ligands are too close together for proper binding, these bacterial β-glucuronidases have proven promiscuous and flexible as evidenced by the diversity of putative inhibitors. Thus, a combined inhibitor would still be effective and would ideally show increased potency by increasing the hydrogen bonding interactions between ligand and protein.

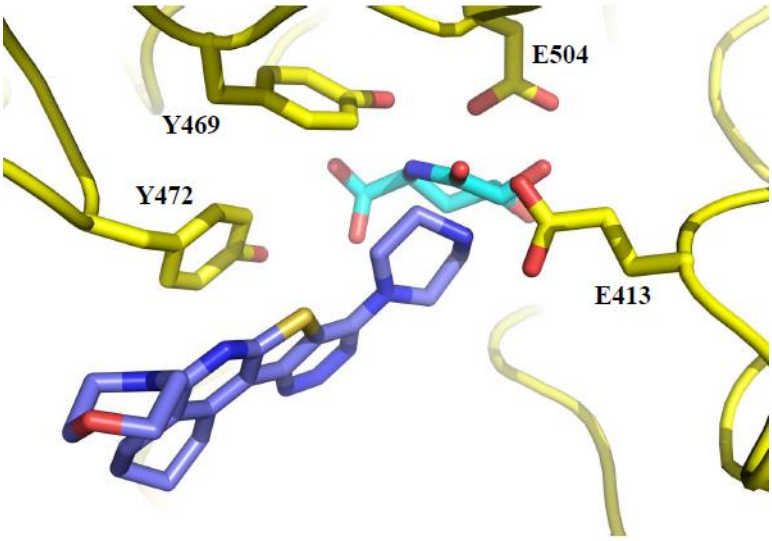

Figure 6.1. Overlay of *Cp*βG (yellow) in complex with Inhibitor 9 (purple) and GDL (cyan) bound to *Ec*βG (not pictured)

6.2 *Bacteroides* β-Glucuronidase

Metagenomic analysis identified two distinct genes responsible for β-glucuronidase activity (28). These genes, termed *gus* and *BG*, belong to distinct phyla of bacteria. The phyla Firmicutes and Proteobacterium contain the *gus* gene, while the Bacteroidetes phylum contains the *BG* gene. In this work, only proteins expressed from putative *gus* genes have been characterized. The *BG*-type enzymes share 21-25% identity to *Ec*βG and appear to contain a shorter, 5-8 residue, bacterial loop based on sequence alignments **(Figure 6.2)**. *BG*-type enzymes can be considerably longer (~900 residues) compared to *gus*-type enzymes (~600 residues). Although cultured *Bacteroides* bacteria have been shown to have considerably less β-glucuronidase activity than their Firmicute counterparts, *Bacteroides* are known to populate a much larger percentage of the mammalian gastrointestinal (GI) tract. Thus, their relative contribution to overall GI β-glucuronidase activity should be similar. Additionally, Wallace *et al.* demonstrated that our inhibitors are effective in cultured *Bacteroides* bacteria (74). Contrary to *gus*-type enzymes described here, the *in vitro* structure and function of *BG*-type β-glucuronidases has not been characterized.

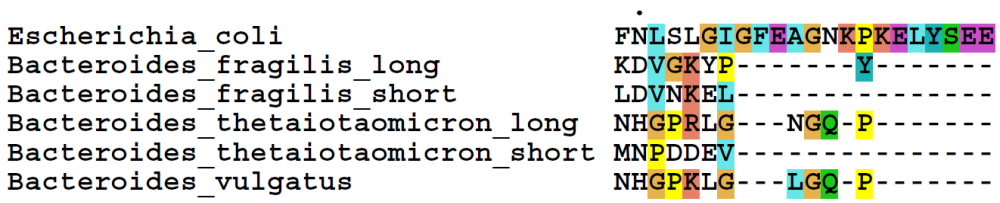

Figure 6.2. Sequence alignment of the putative "bacterial loop" region from *E. coli* compared to regions from various *Bacteroides* species.

For the system of β-glucuronidase inhibition to have *in vivo* success, we likely have to eliminate as much GI β-glucuronidase activity as possible. This would include the contribution of *Bacteroides* and thus, *BG*-type enzymes. Future work would include the expression and purification of putative β-glucuronidases from *Bacteroides* sources. In addition to the *in vitro* characterization of their kinetic properties, we would seek to determine the structural basis of their activity relative to *gus*-type enzymes already studied through x-ray crystallographic analysis. Mutagenesis studies would clarify the mechanisms for probable differences in activity. Any activity would be measured in the presence of lead compounds, and those compounds that prove effective will become more promising leads.

6.3 *In vivo* Mouse Studies

Analogous to studies performed with Inhibitor 1 outlined in Chapter 3, we wish to extend the *in vivo* results to additional lead compounds. For example, Inhibitor O (see Chapter 5) displayed potent *in vitro* and in-cell inhibition of *E. coli*. Distinguishing itself from its counterparts, Inhibitor O maintained *in vitro* potency against other GI-associated enzymes from *C. perfringens* and *S. agalactiae*. Inhibitor 5 (see Chapter 2) also maintained potency across all species and has already proved effective in alleviating CPT-11-induced diarrhea. The most promising compounds, however, belong to the class of analogues of Inhibitor 9 (see Chapter 4). Although each of these compounds display more promising characteristics than the other compounds described in this work, Inhibitor 9-79 distinguishes itself by exhibiting 10-fold greater potency relative to other Inhibitor 9 analogues in *Cp*βG IC_{50} assays.

In addition to repeating experiments with new and more promising lead compounds, including complete pharmacokinetic analysis and oral availability, we would like to extend the characterization of these compounds. New experiments would include the analysis of effects on the pharmacokinetic profile of CPT-11 and NSAIDs beyond systemic circulation and into key organ locations, including liver and feces, including effects on the formulation and administration schedule of lead compounds. Importantly, we would also like to illuminate effects on the anti-tumor efficacy of CPT-11 in a model that recapitulates the clinical setting. To do this, tumors would be grown in mice, as opposed to the experiment presented in Chapter 3 where tumors were xenografted. Mice would also be subjected to a dosing regimen that is comparable to the regimen performed in the clinic.

This work also does not include analysis on possible effects on GI-associated microbiota. Thus, we would like to perform 16S rRNA sequencing on the microbiota in mice, particularly focusing on GI-associated species, before and after treatment with toxic drugs, such as CPT-11 and various NSAIDs, to quantify potential changes in the relative abundance of the bacterial species. Additionally, we would probe, via RNA-Seq experiments, significant changes in the expression of particular genes in the microbiome based on treatments with toxic drugs and the inhibitors presented here. Such experiments would help clarify potential side effects of selective microbial β-glucuronidase inhibition *in vivo*.

6.4 New Models of GI Toxicity

Glucuronidation is a common pathway through which xenobiotic and endobiotic compounds are detoxified. This includes many classes of drugs that contain nucleophilic functional centers (16). By connecting these drugs with drugs that induce GI toxicity, we can search for new models of toxicity that may be alleviated through microbial β-glucuronidase inhibition. One such class of anti-cancer drugs includes topotecan (hycamtin), vorinostat (zolinza), idarubicin (idamycin) and epirubicin (ellence). Continued development of effective, targeted β-glucuronidase inhibitors may improve the tolerance and efficacy of these anticancer drugs. Additionally, it is well established that the active metabolite of morphine is morphine-6-glucuronide, so β-glucuronidase inhibitors may strengthen the efficacy of

morphine by increasing systemic levels of morphine-6-glucuronide. Of course, care must also be taken to avoid a potential toxic buildup of this active metabolite.

As outlined in Chapter 1, GI β-glucuronidases, in addition to familial glycoside hydrolases, play a critical role in homeostasis, particularly in regulating a healthy concentration of hormones or other endobiotics. Polymorphisms in such enzymes have been linked to serious if not fatal disorders. As such, deficiencies in glucuronide-conjugating metabolic reactions that result in an abundance of aglycones could be ameliorated through the use of microbial β-glucuronidase inhibitors, a main source of endogenous aglycone metabolites. It is also possible that the β-glucuronidase-targeted compounds could treat dark-pigment gallstones, which are created from reactivated bilirubin-glucuronide metabolites. With the progressive societal need for new and effective therapies, challenges of drug-induced toxicity will likely continue to emerge, and thus, the possibilities are literally endless.

6.5 Conclusions

Presented here is a system of specific, non-toxic bacterial β-glucuronidase inhibition that produces *in vivo* efficacy. From an initial high-throughput screen, we discovered the first set of novel inhibitors that were characterized structurally and biochemically and proved effective in models of drug-induced toxicity in mice. We expanded the search to a larger, more comprehensive screen that expanded our knowledge of the structure-activity relationship between the inhibitors and their target, bacterial β-glucuronidase. We delved deeper into creating a more promising clinical candidate by making chemical modifications to lead compounds, Inhibitor 1 and Inhibitor 9, to create superior *in vitro* potency and *in vivo* efficacy. Although we were successful in reducing bioavailability of Inhibitor 1 through analogue synthesis, the attempt to improve *in vivo* efficacy in models of toxicity was thwarted potentially by a lack of inhibition against a panel of bacterial β-glucuronidases purified from GI-associated species, *Streptococcus agalactiae* and *Clostridium perfringens*. Nonetheless, those results could prove useful in future endeavors. The most potent *in vitro* compound, Inhibitor 9, was improved in *in vitro* assays through chemical modification to a solvent-exposed side chain. The newly synthesized analogue,

Inhibitor 9-79, separated itself by maintaining low-nanomolar inhibition against each species of β-glucuronidase while Inhibitor 9 and the other synthesized analogues displayed 10-fold reduced potency in *Cp*βG IC_{50} assays. Further *in vivo* studies will be conducted to fully understand how these improvements translate to the preclinical setting.

We are working to improve clinical outcomes for patients that are debilitated by drug-induced GI toxicity. The unique approach begun here could become a co-therapy to a range of chemotherapeutic regimens, similar to the use of xofran (ondansetron) for upper GI toxicity and nausea. It is nonetheless the start towards the emergence of a range of therapeutic targets, those from microbial sources, that have previously been overlooked. The selective inhibition of enzymes in the microbial cells that make up 90% of all cells in the human body, if validated, has the potential to not only establish a new drug discovery paradigm, but also improve the treatment of cancer, pain and other maladies.

Appendix A

Structural Analysis of Mutant hCE1m6

The lab of Dr. Phil Potter has synthesized a mutant form of human carboxylesterase 1 (hCE1), a promiscuous enzyme found through mammalian tissues, with the goal of processing CPT-11 to SN-38 more quickly. This modified enzyme would be used as an enzyme/prodrug therapy to increase the amount of active metabolite that could reach the tumor site. The marker for successful mutations was the activity of rabbit carboxylesterase (rCE), which processes CPT-11 at 41 pmol/h/mg. In the same assay, wild-type hCE1 displayed no detectable CPT-11-converting activity. Therapy with rCE, however, would produce a harmful immunogenic reaction in humans while a modified human enzyme may overcome this concern. In Wierdl *et al.* from 2008, they created one particular mutant, termed hCE1-m6, that maintained levels of carboxylesterase activity relative to wild-type while producing improved CPT-11-converting activity levels, 40.5 pmol/h/mg, similar to rCE1. The mutant enzyme contained 7 point mutations from wild-type hCE1: M363L, L364M, K459R, F488Y, Q449R, L357I, S365G, Q361 insertion (119).

Our lab successfully determined the 2.8 Å un-liganded crystal structure of hCE1-m6 **(Figure A.1)**. The protein was crystallized in the presence of SN-38, but no discernible ligand density was observed beyond glycosylation that was also observed in previous hCE1 structures. The mutated residues fit within the active site in well-defined electron density. By overlaying the hCE1-m6 structure with known structures from hCE1 (bound to tacrine) and rCE, we see a high degree of structural conservation throughout **(Figure A.2)** (120, 121). In fact, there were no discernible structural alterations in the active site. The main differences occurred in solvent-exposed loops **(Figure A.3)**. These changes allow for changes in the active gorge. Viewed as a surface representation, we see that hCE1-m6 allows for less access to the catalytic serine **(Figure A.4)**. Paradoxically, less space in the active site gorge may allow for

more substrate specificity. For CPT-11, for example, a smaller gorge may allow for tighter binding and thus, a higher catalytic efficiency. Docking CPT-11 onto the crystal structures of hCE1 and hCE1-m6, we see that there is still sufficient space for binding **(Figure A.5)**.

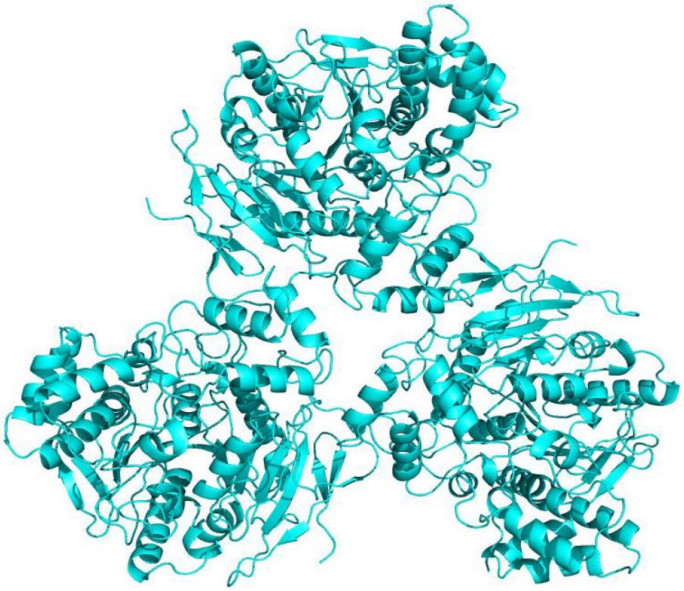

Figure A.1. Crystal structure of full-length hCE1m6

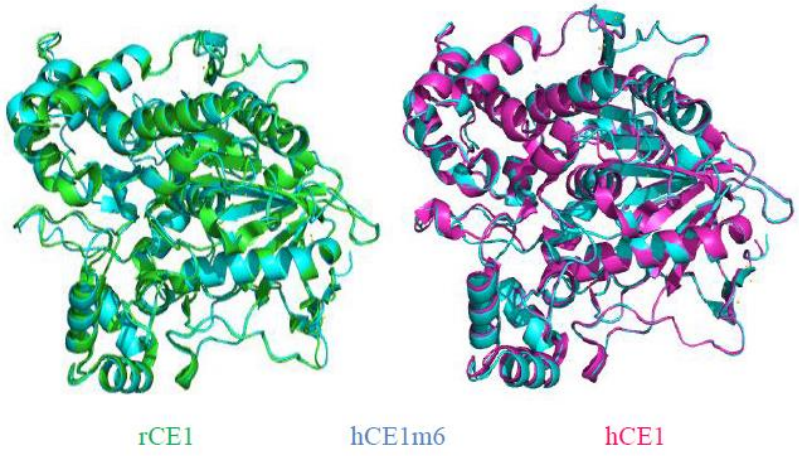

Figure A.2. Overlay of hCE1m6 (cyan) with previously determined structures of rCE (green) and hCE1 bound to tacrine (magenta).

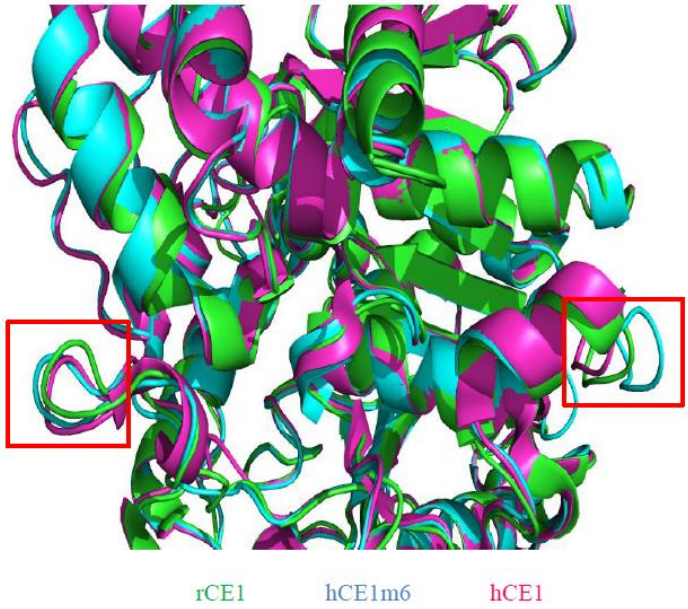

Figure A.3. Overlay of hCE1m6 (cyan) with rCE (green) and hCE1 bound to tacrine (magenta) highlighting differences in solvent-exposed loops (red boxes).

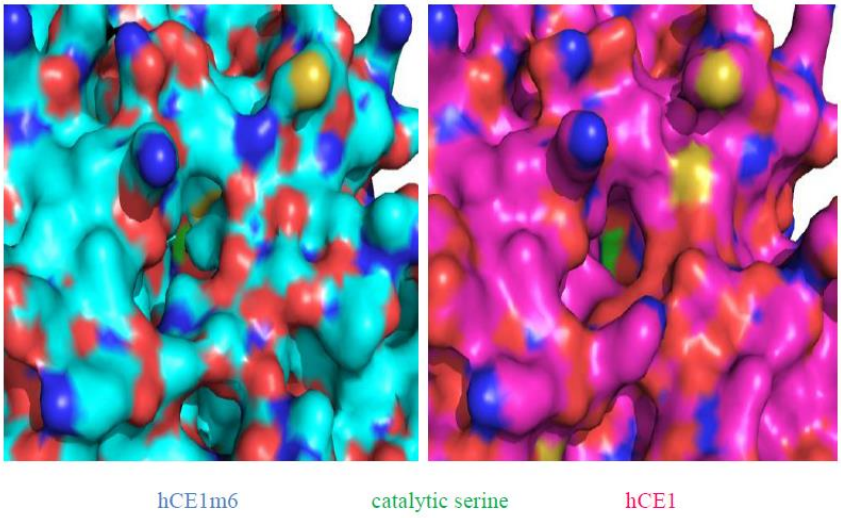

Figure A.4. Differences in the surface area of the catalytic gorge for hCE1m6 (cyan) and hCE1 bound to tacrine (magenta) highlighting access to the catalytic serine residue (green).

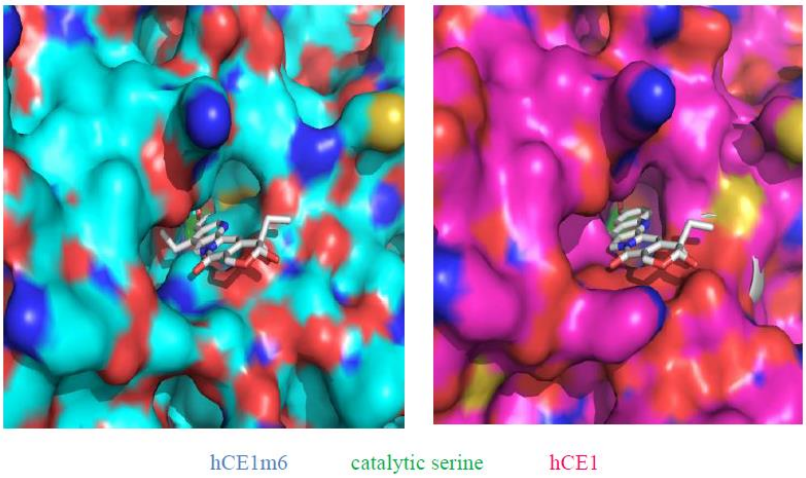

Figure A.5. Docking of CPT-11 in the catalytic gorge for hCE1m6 (cyan) and hCE1 bound to tacrine (magenta) highlighting access to the catalytic serine residue (green).

Appendix B

Immobilization of Active Human Carboxylesterase 1 in Biomimetic Silica Nanoparticles[2]

Summary

The encapsulation of proteins in biomimetic silica has recently been shown to successfully maintain enzymes in their active state. Organophosphate (OP) compounds are employed as pesticides as well as potent chemical warfare nerve agents. Thus, we sought to generate silica-encapsulated enzymes capable of responding to OPs. We present the silica encapsulation of human drug metabolism enzyme carboxylesterase 1 (hCE1) in the presence of a range of catalysts. hCE1 was successfully encapsulated into silica particles when lysozyme or the peptide R5 were used as catalysts; in contrast, polyethyleneimine (PEI), a catalyst employed to encapsulate other enzymes, did not facilitate hCE1 entrapment. hCE1 silica particles in a column chromatography format detect the presence of the OP pesticides paraoxon and dimethyl-p-nitrophenyl phosphate in solution. These results may lead to novel approaches to detect OP pesticides or other weaponized agents, which are known to bind to hCE1. Indeed, we show that hCE1 silicate particles in a column chromatography format detect the presence of the OP pesticides paraoxon and dimethyl-p-nitrophenyl phosphate in solution.

[2]Adapted from Edwards JS et al. (2011) Immobilization of active human carboxylesterase 1 in biomimetic silica nanoparticles. *Biotechnol Prog* 27:863–869.

Introduction

Sol-gel and biomimetic reactions have facilitated the use of immobilized enzymes in a range of applications (122). For example, several recent studies have employed the biomineralization of silica to encapsulate a variety of enzymes. This reaction occurs rapidly at room temperature using a source of silica, such as tetramethylorthosilicate (TMOS), and a polycationic catalyst to promote silica formation around the target enzyme. Proteins encapsulated using this approach can be used to catalyze highly specific reactions, screen for enzyme inhibitors, or detect the presence of chemical compounds. Indeed, silica particles containing enzymes have been employed in biosensing applications, including microfluidic devices and aerosol detectors (123, 124).

There are several advantages to using silica particles for encapsulation. The mild reaction conditions promote the capture of active enzymes and, in some systems, have been shown to increase enzyme stability (125). The simplicity and speed of the reaction also allow for rapid encapsulation and the cost-effective production of the particles for various needs. However, encapsulation efficiency varies with the catalyst-enzyme pair (126). Thus, optimal encapsulation conditions must be identified for each enzyme.

One promising application of encapsulated protein is the detection of chemical toxins, such as organophosphates (OP). OPs are employed as agricultural pesticides, but have also been weaponized for use as highly toxic nerve agents e.g. sarin, soman, and cyclosarin (127, 128). OP toxicity arises from the inhibition of acetylcholinesterase (AChE), which produces sustained acetylcholine stimulus of the muscarinic and nicotinic receptors and may lead to diaphragm incapacitation and suffocation. Biosensors containing enzymes inhibited by OPs have recently been explored for military and civilian applications (123, 129, 130).

The human liver carboxylesterase 1 (hCE1) is a promiscuous serine hydrolase that catalyze the hydrolysis of endo- and xenobiotics containing ester, amide, or thioester bonds (120, 121, 131–135). This structural AChE homolog is currently being explored as prophylactic bioscavenger to decontaminate OP (136). Based upon the ability of hCE1 to bind Ops (133), we sought to determine whether silica

encapsulation of hCE1 would result in nanoparticles containing active enzyme and whether such particles could be employed to detect the presence of OP compounds.

Materials and Methods

Expression and purification of hCE1. A secreted form of hCE1 was expressed using Baculovirus in *Spodptera frugiperda* Sf21 cells and purified as described (Morton and Potter 2000). hCE1 was concentrated in 50 mM HEPES (pH 7.4) and stored at 4 ^{o}C. Protein concentration was determined spectrophotometrically using an extinction coefficient 17700 M^{-1} cm^{-1} (NanoDrop, ND-1000 Spectrophotometer).

Preparation of silica nanoparticles with hCE1. All materials were purchased from Sigma-Aldrich unless otherwise noted. A stock solution of lysozyme at 100 mg/ml was prepared in 0.1 M potassium phosphate buffer (pH 7.4). A solution of hydrolyzed tetramethylorthosilicate (TMOS) was freshly prepared by diluting into 1 mM hydrochloric acid to a final concentration of 1 M. A typical reaction mixture consisted of 800 µl of 0.1 M potassium phosphate buffer containing 5 µg of hCE1, 100 µl of lysozyme or R5 solution (100 mg/ml), and 100 µl of 1 M hydrolyzed TMOS. The mixture was incubated at room temperature (22 ^{o}C) for 10 minutes with gentle shaking. The slurry was centrifuged for 60 s (13,000 rpm) to remove the particles and washed in ddH_2O three times. Control particles were produced in a similar manner using a reaction mixture without hCE1 by combining 800 µl of 0.1 M potassium phosphate buffer, 100 µl of lysozyme solution, and 100 µl of hydrolyzed TMOS. Combination particles were created using ratios of polyethyleneimine (1%) to lysozyme (100 mg/mL) 1:4, 1:1, 4:1 as the catalyst to compare the efficiency of enzyme incorporation. The total volume of catalyst used was always equal to 10% of the silica reaction.

Scanning and transmission electron microscopy. The morphology of silica-encapsulated hCE1 with various catalysts was observed with a Hitachi 4700 Scanning Electron Microscope (SEM) and a JEOL 2010F Transmission Electron Microscope (TEM). SEM samples were prepared by depositing dry powdered samples on a double-stick carbon tape on an aluminium SEM sample holder. The samples were

coated with a 3nm Au-Pd conductive coating in order to prevent charging effect during imaging. TEM samples were prepared by air drying a drop of concentrated reaction mixture on a carbon-stabilized copper grid (Ted Pella Inc.).

Determination of hCE1 enzyme activity. Activity of silica-encapsulated or solution hCE1 were monitored using para-nitrophenyl butyrate (pNPB) as a substrate and measuring the absorbance of the para-nitrophenol product at 410 nm using a Pherastar spectrophotometer (BMG Labtech). The substrate was dissolved in ethanol to a concentration of 1 M, and then diluted to 10 mM in 0.1 M phosphate buffer pH 7.4. hCE1 silica particles were mixed with substrate at a final concentration of 5 mM. Supernatants from the washes were saved and monitored in the same fashion to determine the incorporation efficiency of the silica reactions.

Kinetics of para-nitrophenyl butyrate hydrolysis. K_m, V_{max}, and k_{cat} values were determined by monitoring the conversions of para-nitrophenyl butyrate to nitrophenol product at 410 nm using a Pherastar spectrophotometer (BMG Labtech). Substrate was prepared the same way as described above. Data was collected over 4 minutes and the linear portions were used for the linear regressions to calculate the reaction velocities. Kinetic parameters were determined by fitting hyperbolic plots of reaction velocities versus substrate concentration. The Prism software packaged was used to fit the data (GraphPad, San Diego, CA).

Column-based experiments. Column activity of silica-encapsulated hCE1 was determined using a stainless steel microbore column (2 cm x 2 mm, Upchurch Scientific, Oak Harbor, WA) with 0.5 µm frits. The silica nanoparticle reaction mixture was scaled up to a total of 10 mL. The particles were resuspended in 0.1 M phosphate buffer pH 7.4 and pumped at a flow rate of 10 µL/min to pack the column. The column was washed with 10 column volumes of phosphate buffer prior to use. All column experiments were performed at room temperature (22 ^{o}C) at a flow rate of 100 µL/min using a NE-1000 syringe pump (New Era Pump Systems, Wantagh, NY). Phosphate buffer containing 5 mM substrate was flowed through the column. Samples were collected and analyzed in a Pherastar spectrophotometer to measure absorbance at 410 nm until the substrate hydrolysis had reached a maximum.

Organophosphate pesticide detection. Using a column constructed in the manner described above, phosphate buffer containing 5 mM substrate was applied and absorbance was measured until the substrate hydrolysis reached its maximum value. Phosphate buffer containing 5 mM substrate and paraoxon or DMPNPP (1mM) was then flowed through the column, and absorbance was measured to determine if OP was detected. The pesticides were diluted 1:10 in methanol and further diluted in 0.1 M phosphate buffer pH 7.4 to their final concentration. Inhibition was confirmed by flowing phosphate buffer containing 5 mM substrate through the column and monitoring absorbance at 410 nm.

Results

Silica Encapsulation of Active hCE1

Initial experiments employed lysozyme as the polycation catalyst for silica nanoparticle formation in reaction conditions containing hydrolyzed tetramethylorthosilicate (TMOS), lysozyme (100 mg/mL), and potassium phosphate buffer at pH 7.4 with 5 µg of hCE1 enzyme. Active hCE1was incorporated into the particles with high efficiency leaving no enzyme activity in the supernatant (**Figure B.1A**). In addition, no hCE1 activity was detected in the supernatant around the particles or in the solutions used to wash the particles after formation (**Figure B.1A**). hCE1 activity in the silica nanoparticles, as measured by *para*-nitrophenyl butyrate (pNPB) hydrolysis, reached the same maximal velocity as 5 µg of hCE1 in solution; however, the encapsulated enzyme exhibited a slightly reduced initial rate of product formation (**Figure B.1A, Table B.1**). Multiple washes of silica particles with phosphate buffer did not release active enzyme, indicating that the hCE1 activity associated with the silica particles did not arise from enzyme adhered to particle surfaces.

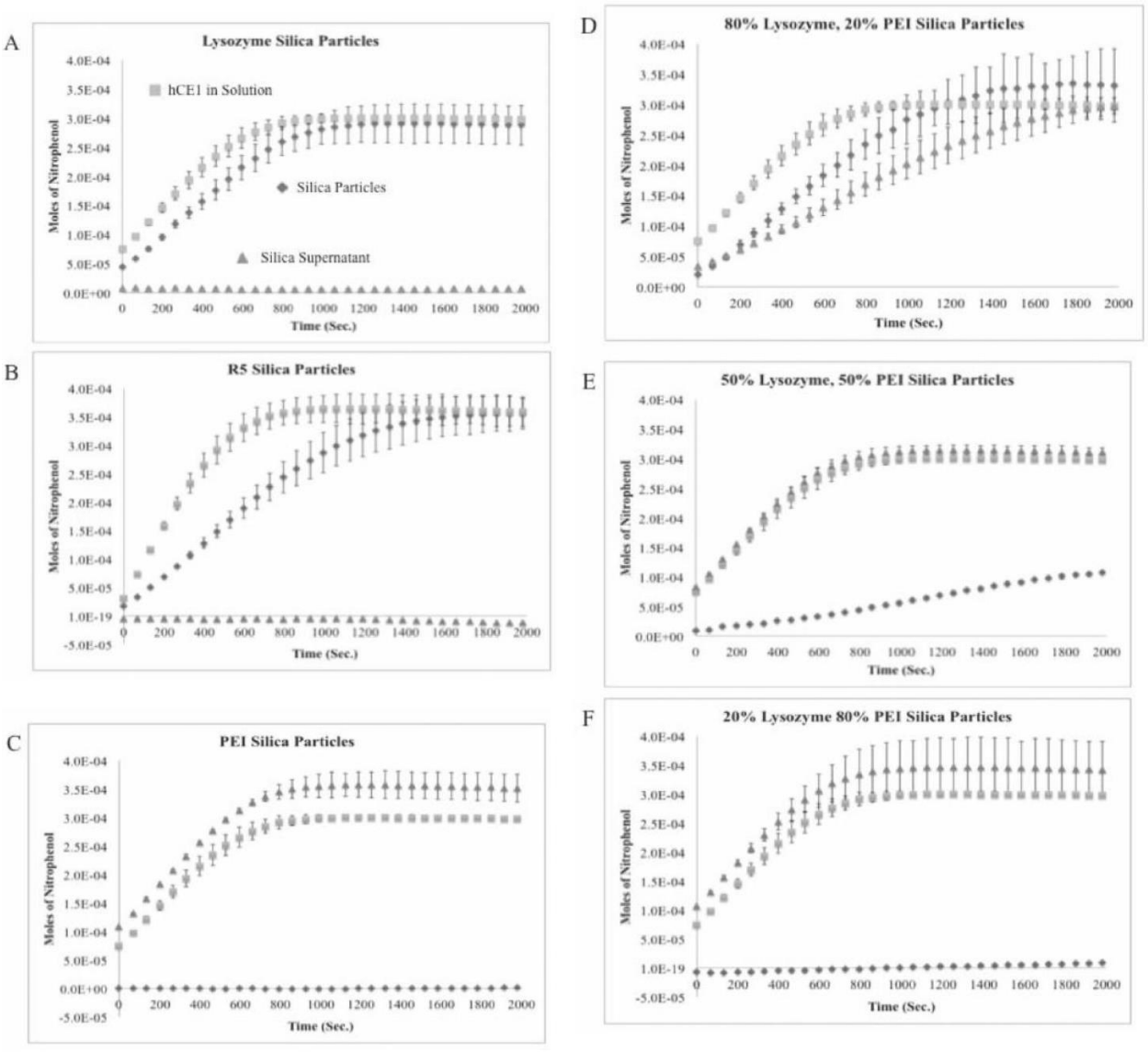

Figure B.1. Activity assays measuring the formation of para-nitrophenol at 410 nm. Silica particles were formed using the respective catalysts and the absorbance was measured over time. Activity was measured for the silica particles, and the supernatant from the reaction, and was compared to hCE1 in solution.

Sample	hCE1 Activity (moles of nitrophenol/second)	R^2
hCE1 in solution	3.42×10^{-7}	0.99
Lysozyme	2.74×10^{-7}	0.99
R5	2.90×10^{-7}	0.99
PEI	NA	
80% Lysozyme, 20% PEI	2.52×10^{-7}	0.99
50% Lysozyme, 50% PEI	3.03×10^{-8}	0.99
20% Lysozyme, 80% PEI	NA	
Lysozyme washed with 1% Tween 20	1.50×10^{-7}	0.99
hCE1 Solution with 1% Tween 20	6.04×10^{-8}	0.99

Table B.1. hCE1 rate of 4-nitrophenyl butyrate hydrolysis in solution compared to silica particles created with different catalysts. NA: not applicable, no enzyme activity contained in the particles.

Next we examined the effect of entrapping hCE1 in silica on the enzyme's ability to hydrolyze substrate. Kinetic experiments were performed maintaining a constant amount of enzyme with varied substrate concentrations to determine initial reaction velocities. Michaelis-Menten kinetics were assumed and the kinetic parameters were determined (**Table B.2**). hCE1 in silica had a K_m that was approximately three times higher than in solution. Furthermore, hCE1 in silica was not as efficient when compared to solution as can be seen by the smaller k_{cat}/K_m values determine. These values are in agreement with previously reported kinetic parameters of hCE1 in solution with pNPB (137). Taken together, these results demonstrate that active hCE1 can be efficiently incorporated into lysozyme-catalyzed silica nanoparticles.

Kinetic Parameters	hCE1 in Solution	hCE1 in Lysozyme Silica
K_m (mM)	3.30 ± 0.44	10.13 ± 0.85
V_{max} (µmole/min/mg)	97.71 ± 4.84	189.72 ± 7.41
Curve Fit (r^2)	0.99	0.99
k_{cat}/K_m ($s^{-1} M^{-1}$)	6.09×10^4	3.85×10^4

Table B.2. Kinetic parameters for the metabolism of PNPB by hCE1 in solution and in lysozyme catalyzed silica particles.

We next investigated the ability of other cationic catalysts to generate hCE1-encapsulated silica nanoparticles. Silica particles were synthesized in the presence of hCE1using the following catalysts: cationic peptide R5 (NH_2-SSKKSGSYSGSKGSKRRIL-CO_2H) (138) and polyethyleneimine (PEI). Silica particles formed with the R5 peptide exhibited similar incorporation efficiency as well as hCE1 enzyme activity relative to the lysozyme silica particles (**Figure B.1B, Table B.1**). In contrast, PEI catalyzed particles, which formed immediately upon mixing (compared to ~5 minutes with the lysozyme or R5 silica particles) excluded hCE1 into the supernatant and thus had no associated enzyme activity with the particles. (**Figure B.1C; Table B.1**). Moreover, the supernatant around the PEI catalyzed particles contained activity similar to the same amount hCE1 in solution.

Next, we sought to improve incorporation efficiency by using a combination of lysozyme and PEI as a catalyst for our biosilicification reaction. We created beads using different ratios of lysozyme and PEI in the presence of the same amount of hCE1 (80% lysozyme:20% PEI, 50% lysozyme:50% PEI, and 20% lysozyme:80% PEI). Increasing the amount of lysozyme relative to PEI improved the encapsulation of hCE1, but no silica particles that were formed in the presence of PEI exhibited higher levels of hCE1 activity than those formed without PEI (**Figures B.1D-F, Table B.1**). Additionally, hCE1 alone could not facilitate the precipitation of silica particles without either lysozyme or the R5 peptide (data not shown). We cooled the reaction to 4°C to see if we could slow the silica condensation in the presence of PEI. The reaction appeared to occur just as fast and no hCE1 was incorporated into the particles (**Data not shown**). Thus, macromolecular catalysts as small as the R5 peptide and as large as hen egg white lysozyme can mediate the formation of silica nanoparticles that encapsulate active hCE1.

Electron Microscopy of hCE1 Nanoparticles

Scanning electron microscopy (SEM) and transmission electron microscopy (TEM) were employed in order to examine the size and morphology of silica particles produced in the presence of hCE1. Silica hCE1 particles using lysozyme as the catalyst were larger than the particles obtained using either R5 or PEI as catalysts. Lysozyme-catalyzed particles were 0.8-1 μm in diameter and appeared to

fuse to form large aggregates on the order of ~ 2 μm (**Figure B.2A**). In contrast, silica particles obtained in the presence of hCE1 using R5 and PEI as catalysts formed individual particles 0.3-0.8 μm in diameter and an aggregate size of ~ 1 μm (**Figure B.2B, C**). Dynamic light scattering (DLS) performed on the lysozyme catalyzed silica particles confirmed the sizes measured from SEM analysis (data not shown). The silica particles formed using the combinations of lysozyme and PEI were smaller (~ 0.5 μm) and appear monodisperse as compared to the particles using only lysozyme or PEI as catalysts (**Figure B.2D, E, F**). Increasing amounts of PEI in the reaction led to the formation of smaller particles and smaller aggregate size.

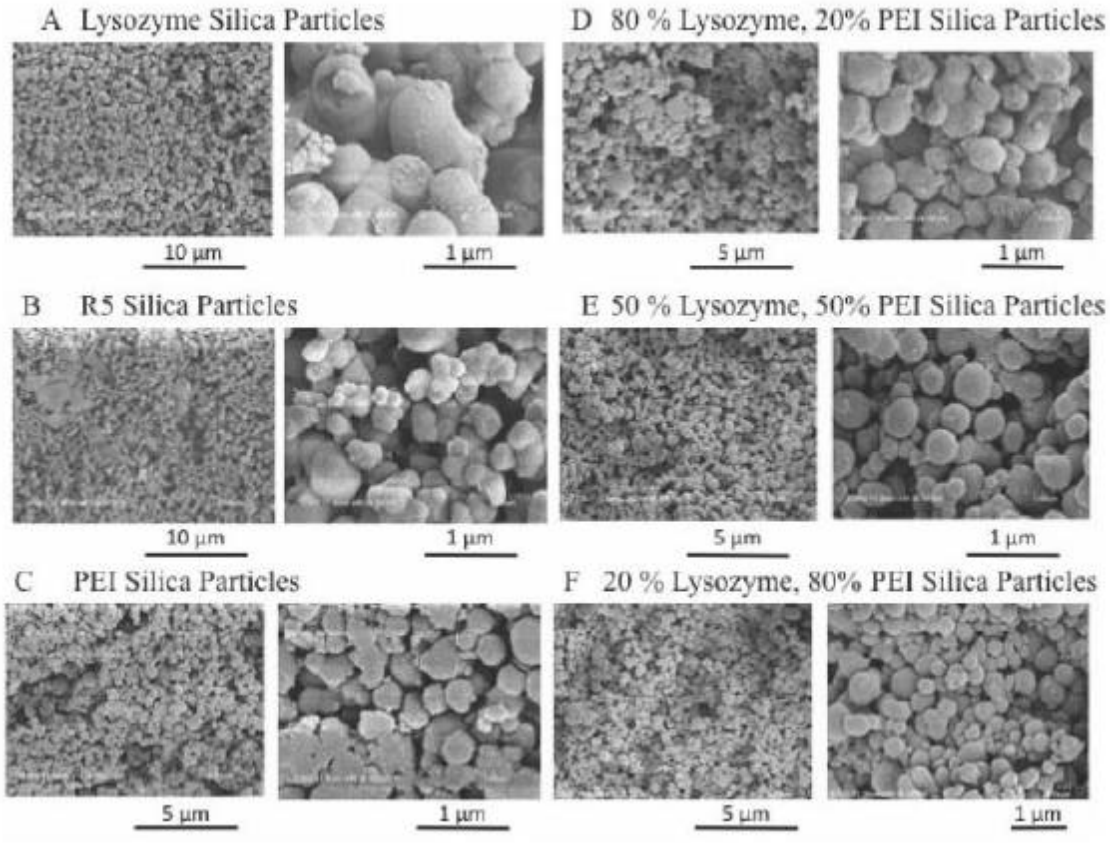

Figure B.2. SEM images of the silica particles containing hCE1 at two magnifications. The samples were sputtered with Au-Pd conductive coating prior to analyses.

TEM images corroborated the SEM data (**Figure B.3A, B**). For example, particles obtained in the presence of lysozyme were larger in size compared to that of the PEI-catalyzed silica particles. In

addition, the TEM images revealed that the lysozyme-catalyzed silica particles exhibited a smoother surface than that of the PEI-catalyzed particles. In contrast, the particles obtained using ratios of lysozyme and PEI as catalysts, appeared to have rougher surface features similar to that seen for the PEI catalyzed particles. This was presumably due to the presence of PEI on the particle surface (**Figure B.3C, D and E**).

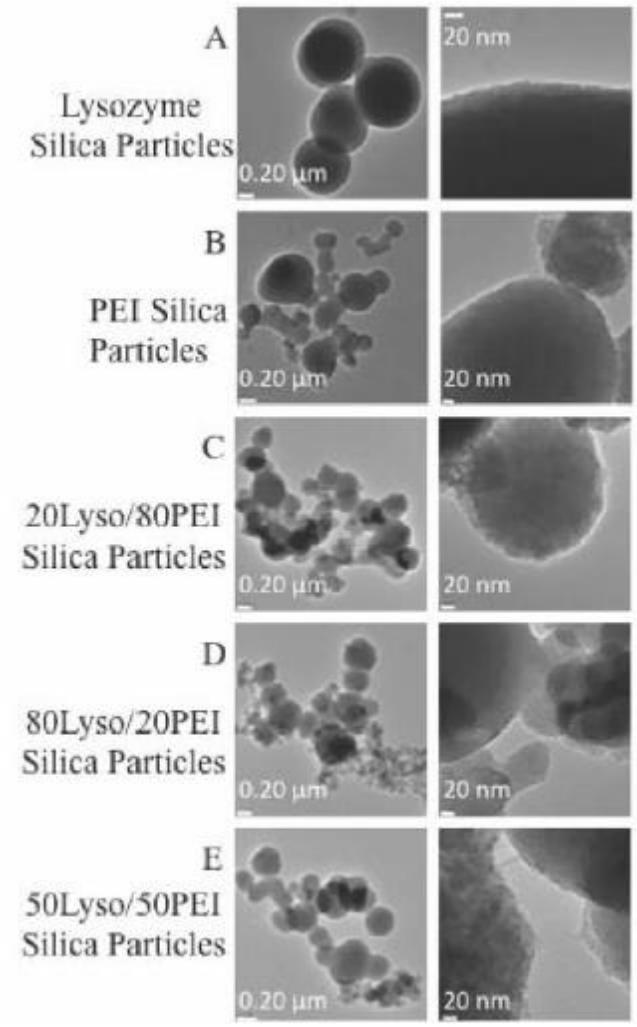

Figure B.3. TEM images of the hCE1 encapsulated silica particles at two magnifications.

Solution Detection Studies with hCE1 Nanoparticles

We examined whether silica nanoparticles containing active hCE1 could function in a column chromatography format. Biosilica particles formed with lysozyme and hCE1 (**see Figures B.1A, B.2A**)

were packed using buffer flow into a stainless steel microbore column (2 cm x 2 mm) with 0.5 µm frits, and subsequent studies controlled using a New Era single syringe pump (New Era Pump Systems, Wantagh, NY). Particles catalyzed with lysozyme in the presence of hCE1 were chosen because they were cost-effective and displayed robust entrapment efficiency and enzyme activity. After extensive washing of the column, pNPB was applied to the column and nitrophenol formation was observed, indicating that hCE1 retains its enzyme activity in the silica particles packed within the column (**Figure B.4**). No hCE1 activity was detected in the solutions used to wash the column, supporting the conclusion that the enzyme remained encapsulated in the column particles (data not shown).

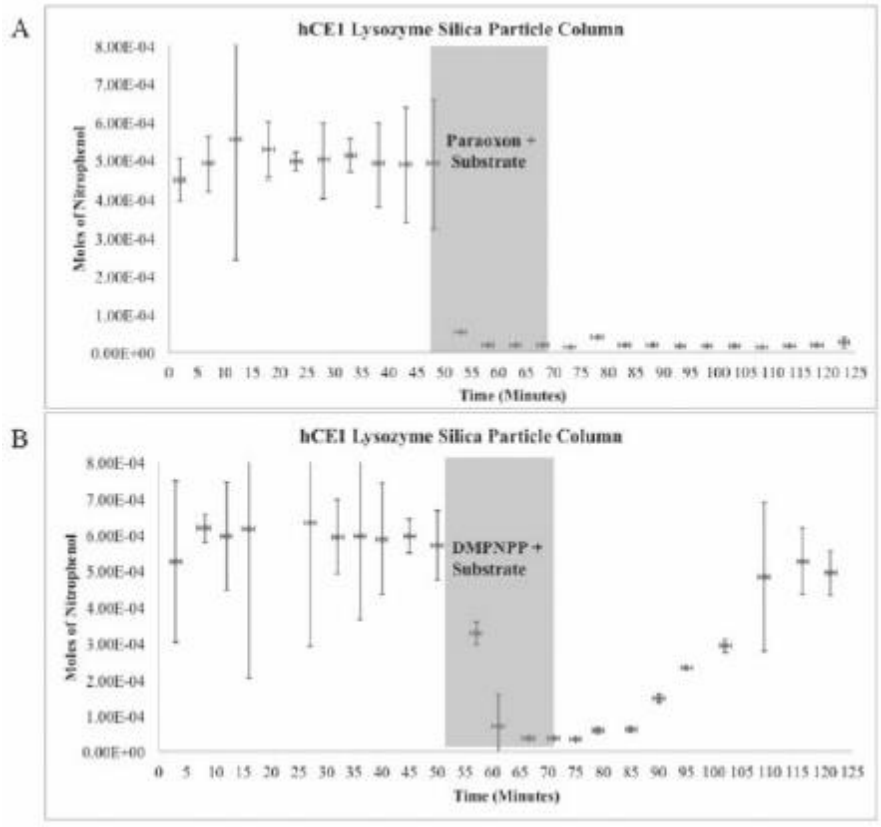

Figure B.4. Microbore columns packed with silica particles catalyzed by lysozyme and containing hCE1 used to detect pesticides. The columns were equilibrated at 25° C to maximum activity before pesticide was applied (grey box). The eluant from the column was collected and measured in triplicate at the respective time points.

We next investigated whether columns containing hCE1 biosilica nanoparticles were capable of detecting OP-pesticides. Columns were operated in the manner described above, and equilibrated such

that a stable amount of para-nitrophenol product was being formed over time (e.g. 10 μmol/min.). At that point, 1 mM diethyl para-nitrophenyl phosphate (paraoxon) was applied to a column, producing a dramatic drop in enzyme activity (**Figure B.4A**). Detection of the presence of this hCE1 inhibitor occurs rapidly, likely due to the small column volume of 16.2 μL. hCE1 remains permanently inhibited by paraoxon even 50 minutes (~70 column volumes) after this inhibitor is removed from the substrate-containing solution applied to the column (**Figure B.4A**). In a second study, dimethyl-*para*-nitrophenylphosphate (DMPNPP) was applied to a column instead of paraoxon. In this case, detection of the hCE1 inhibitor was rapid, but once the inhibitor was removed, hCE1 activity returned over time (**Figure B.4B**). Paraoxon inhibits hCE1 activity 3-fold more robustly in solution than DMPNPP (k_i values of $9.1 \pm 0.5 \times 10^6$ $min^{-1}M^{-1}$ and $2.9 \pm 0.3 \times 10^6$ $min^{-1}M^{-1}$, respectively; data not shown). Taken together, these results indicate that OP pesticides can be detected using hCE1 biosilica nanoparticles within a column chromatography format.

Discussion

Silica nanoparticles have the potential to generate a range of platforms for biodetection. We have shown that hCE1 can be effectively encapsulated into lysozyme-catalyzed silica nanoparticles, which maintain overall enzyme activity comparable to hCE1 in solution. However, they also exhibit a slightly reduced initial rate of product formation, although activity reached that of free hCE1 over time. We hypothesize that this effect is caused by impeded substrate access to the active site of the enzyme in the silica matrix. We also found that hCE1 is more efficiently incorporated into silica nanoparticles using lysozyme as a catalyst in comparison to PEI catalyzed silica particles. Similar results have been observed with other enzymes during encapsulation (126).

In this work, however, we focused on three catalysts – lysozyme, the R5 peptide, and PEI – which have been demonstrated to be successful in previous studies with other target enzymes (129, 139, 140). Based on our results (**see Fig. B.1A-C, Table B.1**), we hypothesize that the lack of entrapped hCE1 during PEI-mediated particle creation was caused by the rapid particle formation and the small size of

PEI. For example, when lysozyme was used as a catalyst, the reaction proceeded slowly, taking approximately 2 minutes until particles can be visualized in solution; in contrast, when PEI was employed, the particles formed immediately. This observation, combined with the smaller sized PEI-catalyzed particles relative to those created with lysozyme (**see Fig. B.1A-C**) suggested that PEI-generated silica matrixes excluded hCE1 under the reaction conditions employed. The lysozyme-catalyzed particles underwent more complete condensation, entrapping all the hCE1 present, similar to that seen for pure sol-gel silica reactions with other enzymes (141).

Finally, we demonstrated that silica nanoparticles containing hCE1 are able to detect OP pesticides in a column chromatography format (**see Fig. B.4**). The drop in hCE1 activity correlated with the strength of the inhibitor employed; for example, paraoxon, a more potent hCE1 inhibitor, did not allow enzyme activity to recover during the time course of the study. Such an apparatus could be employed in the detection of OP pesticides or chemical weapons agents using silica nanoparticles containing hCE1. Both liquid- and gas-based detection have already been reported involving other enzymes, including the cholinesterases (123). Our data indicate that another member of the serine hydrolase family of enzymes may also be employed for this or related technologies.

REFERENCES

1. Consortium THMP (2012) Structure, function and diversity of the healthy human microbiome. *Nature* 486:207–214.

2. Cho I, Blaser MJ (2012) The human microbiome: at the interface of health and disease. *Nat Rev Genet* 13:260–270.

3. Pflughoeft KJ, Versalovic J (2012) Human microbiome in health and disease. *Annu Rev Pathol* 7:99–122.

4. Young VB (2012) The intestinal microbiota in health and disease. *Curr Opin Gastroenterol* 28:63–69.

5. Macpherson AJ, Harris NL (2004) Interactions between commensal intestinal bacteria and the immune system. *Nat Rev Immunol* 4:478–485.

6. Lee YK, Mazmanian SK (2010) Has the microbiota played a critical role in the evolution of the adaptive immune system? *Science* 330:1768–1773.

7. Bischoff SC (2011) "Gut health": a new objective in medicine? *BMC Med* 9:24.

8. Hsiao EY et al. (2013) Microbiota Modulate Behavioral and Physiological Abnormalities Associated with Neurodevelopmental Disorders. *Cell* 155:1451–1463.

9. Tilg H, Kaser A (2011) Gut microbiome, obesity, and metabolic dysfunction. *J Clin Invest* 121:2126–2132.

10. Cani PD, Delzenne NM (2009) Interplay between obesity and associated metabolic disorders: new insights into the gut microbiota. *Curr Opin Pharmacol* 9:737–743.

11. Tremaroli V, Bäckhed F (2012) Functional interactions between the gut microbiota and host metabolism. *Nature* 489:242–249.

12. Soyucen E et al. (2013) Differences in the gut microbiota of healthy children and those with type 1 diabetes. *Pediatr Int Off J Jpn Pediatr Soc*.

13. Tuohy KM, Fava F, Viola R (2014) "The way to a man"s heart is through his gut microbiota' - dietary pro- and prebiotics for the management of cardiovascular risk. *Proc Nutr Soc*:1–14.

14. Littman DR, Pamer EG (2011) Role of the commensal microbiota in normal and pathogenic host immune responses. *Cell Host Microbe* 10:311–323.

15. Guengerich FP (2008) Cytochrome P450 and Chemical Toxicology. *Chem Res Toxicol* 21:70–83.

16. King CD, Rios GR, Green MD, Tephly TR (2000) UDP-glucuronosyltransferases. *Curr Drug Metab* 1:143–161.

17. Sampietro M, Iolascon A (1999) Molecular pathology of Crigler-Najjar type I and II and Gilbert's syndromes. *Haematologica* 84:150–157.

18. Swinney R, Hsu S, Tomlinson G (2006) Phase I and Phase II enzyme polymorphisms and childhood cancer. *J Investig Med Off Publ Am Fed Clin Res* 54:303–320.

19. Shimoi K, Nakayama T (2005) in *Methods in Enzymology*, Phase II Conjugation Enzymes and Transport Systems., ed Helmut Sies and LP (Academic Press), pp 263–272. Available at: http://www.sciencedirect.com/science/article/pii/S0076687905000157 [Accessed February 7, 2014].

20. Jones ML, Martoni CJ, Ganopolsky JG, Labbé A, Prakash S (2014) The human microbiome and bile acid metabolism: dysbiosis, dysmetabolism, disease and intervention. *Expert Opin Biol Ther*.

21. Henrissat B, Davies G (1997) Structural and sequence-based classification of glycoside hydrolases. *Curr Opin Struct Biol* 7:637–644.

22. Naz H et al. (2013) Human β -Glucuronidase: Structure, Function, and Application in Enzyme Replacement Therapy. *Rejuvenation Res* 16:352–363.

23. De Graaf M, Boven E, Scheeren HW, Haisma HJ, Pinedo HM (2002) Beta-glucuronidase-mediated drug release. *Curr Pharm Des* 8:1391–1403.

24. Basu C, Kausch AP, Chandlee JM (2004) Use of β-glucuronidase reporter gene for gene expression analysis in turfgrasses. *Biochem Biophys Res Commun* 320:7–10.

25. Fiksdal L, Tryland I (2008) Application of rapid enzyme assay techniques for monitoring of microbial water quality. *Curr Opin Biotechnol* 19:289–294.

26. Russell WM, Klaenhammer TR (2001) Identification and cloning of gusA, encoding a new beta-glucuronidase from Lactobacillus gasseri ADH. *Appl Environ Microbiol* 67:1253–1261.

27. McIntosh FM et al. (2012) Phylogenetic distribution of genes encoding β-glucuronidase activity in human colonic bacteria and the impact of diet on faecal glycosidase activities. *Environ Microbiol* 14:1876–1887.

28. Gloux K et al. (2011) A metagenomic β-glucuronidase uncovers a core adaptive function of the human intestinal microbiome. *Proc Natl Acad Sci U S A* 108 Suppl 1:4539–4546.

29. Michikawa M et al. (2012) Structural and Biochemical Characterization of Glycoside Hydrolase Family 79 β-Glucuronidase from Acidobacterium capsulatum. *J Biol Chem* 287:14069–14077.

30. Sperker B et al. (1997) Interindividual Variability in Expression and Activity of Human β-Glucuronidase in Liver and Kidney: Consequences for Drug Metabolism. *J Pharmacol Exp Ther* 281:914–920.

31. Dabek M, McCrae SI, Stevens VJ, Duncan SH, Louis P (2008) Distribution of beta-glucosidase and beta-glucuronidase activity and of beta-glucuronidase gene gus in human colonic bacteria. *FEMS Microbiol Ecol* 66:487–495.

32. Pusztaszeri MP, Genta RM, Cryer BL (2007) Drug-induced injury in the gastrointestinal tract: clinical and pathologic considerations. *Nat Clin Pract Gastroenterol Hepatol* 4:442–453.

33. Sousa T et al. (2008) The gastrointestinal microbiota as a site for the biotransformation of drugs. *Int J Pharm* 363:1–25.

34. Okuda H, Ogura K, Kato A, Takubo H, Watabe T (1998) A possible mechanism of eighteen patient deaths caused by interactions of sorivudine, a new antiviral drug, with oral 5-fluorouracil prodrugs. *J Pharmacol Exp Ther* 287:791–799.

35. Pizzolato JF, Saltz LB (2003) The camptothecins. *Lancet* 361:2235–2242.

36. Hsiang YH, Hertzberg R, Hecht S, Liu LF (1985) Camptothecin induces protein-linked DNA breaks via mammalian DNA topoisomerase I. *J Biol Chem* 260:14873–14878.

37. Cunningham D et al. (1998) Randomised trial of irinotecan plus supportive care versus supportive care alone after fluorouracil failure for patients with metastatic colorectal cancer. *Lancet* 352:1413–1418.

38. Fuchs CS et al. (2003) Phase III Comparison of Two Irinotecan Dosing Regimens in Second-Line Therapy of Metastatic Colorectal Cancer. *J Clin Oncol* 21:807 –814.

39. Hu Z-P et al. (2006) St. John's wort attenuates irinotecan-induced diarrhea via down-regulation of intestinal pro-inflammatory cytokines and inhibition of intestinal epithelial apoptosis. *Toxicol Appl Pharmacol* 216:225–237.

40. Kurita A et al. (2011) Streptomycin alleviates irinotecan-induced delayed-onset diarrhea in rats by a mechanism other than inhibition of β-glucuronidase activity in intestinal lumen. *Cancer Chemother Pharmacol* 67:201–213.

41. Saltz LB et al. (2000) Irinotecan plus fluorouracil and leucovorin for metastatic colorectal cancer. Irinotecan Study Group. *N Engl J Med* 343:905–914.

42. Rougier P et al. (1998) Randomised trial of irinotecan versus fluorouracil by continuous infusion after fluorouracil failure in patients with metastatic colorectal cancer. *Lancet* 352:1407–1412.

43. Rougier P et al. (1997) Phase II study of irinotecan in the treatment of advanced colorectal cancer in chemotherapy-naive patients and patients pretreated with fluorouracil-based chemotherapy. *J Clin Oncol Off J Am Soc Clin Oncol* 15:251–260.

44. Rothenberg ML et al. (1996) Phase II trial of irinotecan in patients with progressive or rapidly recurrent colorectal cancer. *J Clin Oncol Off J Am Soc Clin Oncol* 14:1128–1135.

45. Smith NF, Figg WD, Sparreboom A (2006) Pharmacogenetics of irinotecan metabolism and transport: an update. *Toxicol Vitro Int J Publ Assoc BIBRA* 20:163–175.

46. Kambe M et al. (2012) Phase I study of irinotecan by 24-h intravenous infusion in combination with 5-fluorouracil in metastatic colorectal cancer. *Int J Clin Oncol* 17:150–154.

47. Engstrom PF et al. (2009) Colon Cancer. *J Natl Compr Canc Netw* 7:778–831.

48. Han J-Y et al. (2012) A genome-wide association study for irinotecan-related severe toxicities in patients with advanced non-small-cell lung cancer. *Pharmacogenomics J*. Available at: http://www.ncbi.nlm.nih.gov/pubmed/22664479 [Accessed July 6, 2012].

49. Zaniboni A et al. (2012) FOLFIRI as second-line chemotherapy for advanced pancreatic cancer: a GISCAD multicenter phase II study. *Cancer Chemother Pharmacol* 69:1641–1645.

50. Matsumura M et al. (2010) Neoadjuvant chemotherapy followed by radical hysterectomy plus postoperative chemotherapy but no radiotherapy for Stage IB2-IIB cervical cancer--irinotecan and platinum chemotherapy. *Gynecol Oncol* 119:212–216.

51. Jo J-C et al. (2012) Phase II and UGT1A1 genotype study of irinotecan dose escalation as salvage therapy for advanced gastric cancer. *Br J Cancer* 106:1591–1597.

52. Lee KS, Park IH, Nam B-H, Ro J (2012) Phase II study of irinotecan plus capecitabine in anthracycline- and taxane- pretreated patients with metastatic breast cancer. *Invest New Drugs*. Available at: http://www.ncbi.nlm.nih.gov/pubmed/22562702 [Accessed July 6, 2012].

53. Spigel DR et al. (2012) Phase II study of maintenance sunitinib following irinotecan and carboplatin as first-line treatment for patients with extensive-stage small-cell lung cancer. *Lung Cancer Amst Neth*. Available at: http://www.ncbi.nlm.nih.gov/pubmed/22560921 [Accessed July 6, 2012].

54. Kim A, Ueda Y, Naka T, Enomoto T (2012) Therapeutic strategies in epithelial ovarian cancer. *J Exp Clin Cancer Res CR* 31:14.

55. Iyer L et al. (1998) Genetic predisposition to the metabolism of irinotecan (CPT-11). Role of uridine diphosphate glucuronosyltransferase isoform 1A1 in the glucuronidation of its active metabolite (SN-38) in human liver microsomes. *J Clin Invest* 101:847–854.

56. Saliba F et al. (1998) Pathophysiology and therapy of irinotecan-induced delayed-onset diarrhea in patients with advanced colorectal cancer: a prospective assessment. *J Clin Oncol Off J Am Soc Clin Oncol* 16:2745–2751.

57. Kawato Y, Aonuma M, Hirota Y, Kuga H, Sato K (1991) Intracellular roles of SN-38, a metabolite of the camptothecin derivative CPT-11, in the antitumor effect of CPT-11. *Cancer Res* 51:4187–4191.

58. Mathijssen RH et al. (2001) Clinical pharmacokinetics and metabolism of irinotecan (CPT-11). *Clin Cancer Res Off J Am Assoc Cancer Res* 7:2182–2194.

59. Ma MK, McLeod HL (2003) Lessons learned from the irinotecan metabolic pathway. *Curr Med Chem* 10:41–49.

60. Nagar S, Blanchard RL (2006) Pharmacogenetics of uridine diphosphoglucuronosyltransferase (UGT) 1A family members and its role in patient response to irinotecan. *Drug Metab Rev* 38:393–409.

61. Takasuna K et al. (1996) Involvement of beta-glucuronidase in intestinal microflora in the intestinal toxicity of the antitumor camptothecin derivative irinotecan hydrochloride (CPT-11) in rats. *Cancer Res* 56:3752–3757.

62. Tobin PJ, Dodds HM, Clarke S, Schnitzler M, Rivory LP (2003) The relative contributions of carboxylesterase and beta-glucuronidase in the formation of SN-38 in human colorectal tumours. *Oncol Rep* 10:1977–1979.

63. Brandi G et al. (2006) Intestinal microflora and digestive toxicity of irinotecan in mice. *Clin Cancer Res Off J Am Assoc Cancer Res* 12:1299–1307.

64. Takasuna K et al. (1998) Inhibition of intestinal microflora beta-glucuronidase modifies the distribution of the active metabolite of the antitumor agent, irinotecan hydrochloride (CPT-11) in rats. *Cancer Chemother Pharmacol* 42:280–286.

65. Abigerges D et al. (1994) Irinotecan (CPT-11) high-dose escalation using intensive high-dose loperamide to control diarrhea. *J Natl Cancer Inst* 86:446–449.

66. Ducreux M, Köhne C-H, Schwartz GK, Vanhoefer U (2003) Irinotecan in metastatic colorectal cancer: dose intensification and combination with new agents, including biological response modifiers. *Ann Oncol Off J Eur Soc Med Oncol ESMO* 14 Suppl 2:ii17–23.

67. Zhao J, Huang L, Belmar N, Buelow R, Fong T (2004) Oral RDP58 allows CPT-11 dose intensification for enhanced tumor response by decreasing gastrointestinal toxicity. *Clin Cancer Res Off J Am Assoc Cancer Res* 10:2851–2859.

68. Beretta GL, Zuco V, De Cesare M, Perego P, Zaffaroni N (2012) Namitecan: a hydrophilic camptothecin with a promising preclinical profile. *Curr Med Chem* 19:3488–3501.

69. Takeda Y et al. (2001) Prevention of irinotecan (CPT-11)-induced diarrhea by oral alkalization combined with control of defecation in cancer patients. *Int J Cancer J Int Cancer* 92:269–275.

70. Ikegami T et al. (2002) Intestinal alkalization as a possible preventive mechanism in irinotecan (CPT-11)-induced diarrhea. *Cancer Res* 62:179–187.

71. Hamada A et al. (2005) Pharmacokinetic changes of irinotecan by intestinal alkalinization in an advanced colorectal cancer patient. *Ther Drug Monit* 27:536–538.

72. Marsh S, Hoskins JM (2010) Irinotecan pharmacogenomics. *Pharmacogenomics* 11:1003–1010.

73. Fittkau M, Voigt W, Holzhausen H-J, Schmoll H-J (2004) Saccharic acid 1.4-lactone protects against CPT-11-induced mucosa damage in rats. *J Cancer Res Clin Oncol* 130:388–394.

74. Wallace BD et al. (2010) Alleviating cancer drug toxicity by inhibiting a bacterial enzyme. *Science* 330:831–835.

75. Scarpignato C, Hunt RH (2010) Nonsteroidal antiinflammatory drug-related injury to the gastrointestinal tract: clinical picture, pathogenesis, and prevention. *Gastroenterol Clin North Am* 39:433–464.

76. Boelsterli UA, Ramirez-Alcantara V (2011) NSAID acyl glucuronides and enteropathy. *Curr Drug Metab* 12:245–252.

77. Wallace JL (2012) NSAID gastropathy and enteropathy: distinct pathogenesis likely necessitates distinct prevention strategies. *Br J Pharmacol* 165:67–74.

78. Lai LH, Chan FKL (2009) Nonsteroid anti-inflammatory drug-induced gastroduodenal injury. *Curr Opin Gastroenterol* 25:544–548.

79. Wolfe MM, Lichtenstein DR, Singh G (1999) Gastrointestinal toxicity of nonsteroidal antiinflammatory drugs. *N Engl J Med* 340:1888–1899.

80. Fiorucci S (2009) Prevention of nonsteroidal anti-inflammatory drug-induced ulcer: looking to the future. *Gastroenterol Clin North Am* 38:315–332.

81. Graham DY, Opekun AR, Willingham FF, Qureshi WA (2005) Visible small-intestinal mucosal injury in chronic NSAID users. *Clin Gastroenterol Hepatol Off Clin Pract J Am Gastroenterol Assoc* 3:55–59.

82. Boelsterli UA, Redinbo MR, Saitta KS (2013) Multiple NSAID-induced hits injure the small intestine: underlying mechanisms and novel strategies. *Toxicol Sci Off J Soc Toxicol* 131:654–667.

83. Regan SL et al. (2010) Acyl glucuronides: the good, the bad and the ugly. *Biopharm Drug Dispos* 31:367–395.

84. Bailey MJ, Dickinson RG (2003) Acyl glucuronide reactivity in perspective: biological consequences. *Chem Biol Interact* 145:117–137.

85. LoGuidice A, Wallace BD, Bendel L, Redinbo MR, Boelsterli UA (2012) Pharmacologic targeting of bacterial β-glucuronidase alleviates nonsteroidal anti-inflammatory drug-induced enteropathy in mice. *J Pharmacol Exp Ther* 341:447–454.

86. Saitta KS et al. (2013) Bacterial β-glucuronidase inhibition protects mice against enteropathy induced by indomethacin, ketoprofen or diclofenac: mode of action and pharmacokinetics. *Xenobiotica Fate Foreign Compd Biol Syst*.

87. Mani S, Boelsterli UA, Redinbo MR (2013) Understanding and Modulating Mammalian-Microbial Communication for Improved Human Health. *Annu Rev Pharmacol Toxicol*.

88. Tobin P et al. (2006) The in vitro metabolism of irinotecan (CPT-11) by carboxylesterase and beta-glucuronidase in human colorectal tumours. *Br J Clin Pharmacol* 62:122–129.

89. Stachulski AV (2010) Acyl Glucuronides: Mechanistic Role in Drug Toxicity? Chemistry and Reactivity of Acyl Glucuronides. *Curr Drug Metab*. Available at: http://www.ncbi.nlm.nih.gov/pubmed/20946098 [Accessed April 6, 2011].

90. Wallace BD, Redinbo MR (2013) The human microbiome is a source of therapeutic drug targets. *Curr Opin Chem Biol* 17:379–384.

91. Ahmad S et al. (2011) A High Throughput Assay for Discovery of Bacterial β-Glucuronidase Inhibitors. *Curr Chem Genomics* 5:13–20.

92. Graef V, Furuya E, Nishikaze O (1977) Hydrolysis of steroid glucuronides with beta-glucuronidase preparations from bovine liver, Helix pomatia, and E. coli. *Clin Chem* 23:532–535.

93. Z. Otwinowski, W. Minor, Charles W. Carter, Jr. (1997) *Methods Enzymol.* (Academic Press).

94. McCoy AJ et al. (2007) Phaser crystallographic software. *J Appl Crystallogr* 40:658–674.

95. Brünger AT (1997) Free R value: cross-validation in crystallography. *Methods Enzymol* 277:366–396.

96. Adams PD et al. (2002) PHENIX: building new software for automated crystallographic structure determination. *Acta Crystallogr D Biol Crystallogr* 58:1948–1954.

97. Emsley P, Cowtan K (2004) Coot: model-building tools for molecular graphics. *Acta Crystallogr D Biol Crystallogr* 60:2126–2132.

98. Schüttelkopf AW, van Aalten DMF (2004) PRODRG: a tool for high-throughput crystallography of protein-ligand complexes. *Acta Crystallogr D Biol Crystallogr* 60:1355–1363.

99. Cooper HS, Murthy SN, Shah RS, Sedergran DJ (1993) Clinicopathologic study of dextran sulfate sodium experimental murine colitis. *Lab Investig J Tech Methods Pathol* 69:238–249.

100. Reagan-Shaw S, Nihal M, Ahmad N (2008) Dose translation from animal to human studies revisited. *FASEB J Off Publ Fed Am Soc Exp Biol* 22:659–661.

101. Jain S et al. (1996) Structure of human beta-glucuronidase reveals candidate lysosomal targeting and active-site motifs. *Nat Struct Biol* 3:375–381.

102. Maurice CF, Haiser HJ, Turnbaugh PJ (2013) Xenobiotics shape the physiology and gene expression of the active human gut microbiome. *Cell* 152:39–50.

103. Vítek L, Zelenka J, Zadinová M, Malina J (2005) The impact of intestinal microflora on serum bilirubin levels. *J Hepatol* 42:238–243.

104. Huang P-T et al. (2011) Enhancement of CPT-11 antitumor activity by adenovirus-mediated expression of β–glucuronidase in tumors. *Cancer Gene Ther* 18:381–389.

105. Araki E et al. (1993) Relationship between development of diarrhea and the concentration of SN-38, an active metabolite of CPT-11, in the intestine and the blood plasma of athymic mice following intraperitoneal administration of CPT-11. *Jpn J Cancer Res Gann* 84:697–702.

106. Roberts AB, Wallace BD, Venkatesh MK, Mani S, Redinbo MR (2013) Molecular Insights into Microbial β-Glucuronidase Inhibition to Abrogate CPT-11 Toxicity. *Mol Pharmacol*.

107. Blaut M, Klaus S (2012) Intestinal microbiota and obesity. *Handb Exp Pharmacol*:251–273.

108. Grice EA, Segre JA (2012) The human microbiome: our second genome. *Annu Rev Genomics Hum Genet* 13:151–170.

109. Reigstad CS, Kashyap PC (2013) Beyond phylotyping: understanding the impact of gut microbiota on host biology. *Neurogastroenterol Motil Off J Eur Gastrointest Motil Soc* 25:358–372.

110. Flores R et al. (2012) Fecal microbial determinants of fecal and systemic estrogens and estrogen metabolites: a cross-sectional study. *J Transl Med* 10:253.

111. Hu M (2007) Commentary: Bioavailability of Flavonoids and Polyphenols: Call to Arms. *Mol Pharm* 4:803–806.

112. Xing J, Chen X, Zhong D (2005) Absorption and enterohepatic circulation of baicalin in rats. *Life Sci* 78:140–146.

113. Vítek L et al. (2000) Intestinal colonization leading to fecal urobilinoid excretion may play a role in the pathogenesis of neonatal jaundice. *J Pediatr Gastroenterol Nutr* 30:294–298.

114. Bemis GW, Murcko MA (1996) The properties of known drugs. 1. Molecular frameworks. *J Med Chem* 39:2887–2893.

115. Walters WP, Murcko MA (2002) Prediction of "drug-likeness." *Adv Drug Deliv Rev* 54:255–271.

116. Lipinski CA, Lombardo F, Dominy BW, Feeney PJ (1997) Experimental and computational approaches to estimate solubility and permeability in drug discovery and development settings. *Adv Drug Deliv Rev* 23:3–25.

117. Henderson TR, Henderson RF, York JL (1975) Effects of Dimethyl Sulfoxide on Subunit Proteins*. *Ann N Y Acad Sci* 243:38–53.

118. Gupta E et al. (1994) Metabolic fate of irinotecan in humans: correlation of glucuronidation with diarrhea. *Cancer Res* 54:3723–3725.

119. Wierdl M et al. (2008) An improved human carboxylesterase for enzyme/prodrug therapy with CPT-11. *Cancer Gene Ther* 15:183–192.

120. Bencharit S et al. (2003) Crystal structure of human carboxylesterase 1 complexed with the Alzheimer's drug tacrine: from binding promiscuity to selective inhibition. *Chem Biol* 10:341–349.

121. Bencharit S et al. (2002) Structural insights into CPT-11 activation by mammalian carboxylesterases. *Nat Struct Biol* 9:337–342.

122. Frenkel-Mullerad H, Avnir D (2005) Sol-gel materials as efficient enzyme protectors: preserving the activity of phosphatases under extreme ph conditions. *J Am Chem Soc* 127:8077–8081.

123. Luckarift HR, Greenwald R, Bergin MH, Spain JC, Johnson GR (2007) Biosensor system for continuous monitoring of organophosphate aerosols. *Biosens Bioelectron* 23:400–406.

124. Luckarift HR, Ku BS, Dordick JS, Spain JC (2007) Silica-immobilized enzymes for multi-step synthesis in microfluidic devices. *Biotechnol Bioeng* 98:701–705.

125. Luckarift HR, Spain JC, Naik RR, Stone MO (2004) Enzyme immobilization in a biomimetic silica support. *Nat Biotechnol* 22:211–213.

126. Betancor L, Luckarift HR (2008) Bioinspired enzyme encapsulation for biocatalysis. *Trends Biotechnol* 26:566–572.

127. Aardema H et al. (2008) Organophosphorus pesticide poisoning: cases and developments. *Neth J Med* 66:149–153.

128. Newmark J (2007) Nerve agents. *The neurologist* 13:20–32.

129. Luckarift HR, Dickerson MB, Sandhage KH, Spain JC (2006) Rapid, room-temperature synthesis of antibacterial bionanocomposites of lysozyme with amorphous silica or titania. *Small Weinh Bergstr Ger* 2:640–643.

130. Ramanathan M et al. (2009) Lysozyme-mediated formation of protein-silica nano-composites for biosensing applications. *Colloids Surf B Biointerfaces* 73:58–64.

131. Bencharit S et al. (2006) Multisite promiscuity in the processing of endogenous substrates by human carboxylesterase 1. *J Mol Biol* 363:201–214.

132. Bencharit S, Morton CL, Xue Y, Potter PM, Redinbo MR (2003) Structural basis of heroin and cocaine metabolism by a promiscuous human drug-processing enzyme. *Nat Struct Biol* 10:349–356.

133. Fleming CD et al. (2005) Structural insights into drug processing by human carboxylesterase 1: tamoxifen, mevastatin, and inhibition by benzil. *J Mol Biol* 352:165–177.

134. Redinbo MR, Bencharit S, Potter PM (2003) Human carboxylesterase 1: from drug metabolism to drug discovery. *Biochem Soc Trans* 31:620–624.

135. Redinbo MR, Potter PM (2005) Mammalian carboxylesterases: from drug targets to protein therapeutics. *Drug Discov Today* 10:313–325.

136. Hemmert AC et al. (2010) Human carboxylesterase 1 stereoselectively binds the nerve agent cyclosarin and spontaneously hydrolyzes the nerve agent sarin. *Mol Pharmacol* 77:508–516.

137. Wadkins RM et al. (2001) Structural constraints affect the metabolism of 7-ethyl-10-[4-(1-piperidino)-1-piperidino]carbonyloxycamptothecin (CPT-11) by carboxylesterases. *Mol Pharmacol* 60:355–362.

138. Nam DH, Won K, Kim YH, Sang BI (2009) A novel route for immobilization of proteins to silica particles incorporating silaffin domains. *Biotechnol Prog* 25:1643–1649.

139. Betancor L, Berne C, Luckarift HR, Spain JC (2006) Coimmobilization of a redox enzyme and a cofactor regeneration system. *Chem Commun Camb Engl*:3640–3642.

140. Naik RR, Tomczak MM, Luckarift HR, Spain JC, Stone MO (2004) Entrapment of enzymes and nanoparticles using biomimetically synthesized silica. *Chem Commun Camb Engl*:1684–1685.

141. Gao Y, Heinemann A, Knott R, Bartlett J (2010) Encapsulation of protein in silica matrices: structural evolution on the molecular and nanoscales. *Langmuir ACS J Surf Colloids* 26:1239–1246.